

NASA Technical Memorandum 86240

Geopotential Research Mission, Science, Engineering, and Program Summary

Edited by

Thomas Keating, Patrick Taylor,
Werner Kahn, and Francis Lerch

*Goddard Space Flight Center
Greenbelt, Maryland*



National Aeronautics
and Space Administration

Scientific and Technical
Information Branch

1986

FOREWORD

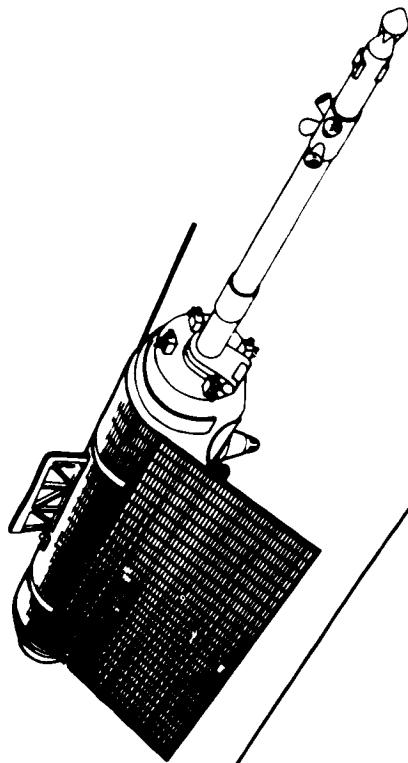
This report is based on the accumulated scientific and engineering studies pertaining to the Geopotential Research Mission (GRM). The scientific need and justification for the measurement of the Earth's gravity and magnetic fields are discussed. Emphasis is placed on the studies and conclusions of scientific organizations and NASA advisory groups. The engineering design and investigations performed over the last 4 years are described, and a spacecraft design capable of fulfilling all scientific objectives is presented.

While subsequent studies and design changes are expected to supercede the information presented herein, this report provides the baseline for the mission and indicates future modifications. In addition, critical features of the scientific requirements and state-of-the-art limitations of spacecraft design, mission flight performance, and data processing are discussed.

For additional information contact:

Dr. E. A. Flinn, NASA Headquarters Geodynamics Program Office
Dr. D. E. Smith, GSFC Project Scientist for Gravity
Mr. W. D. Kahn, GSFC Scientist for Gravity
Dr. P. T. Taylor, GSFC Project Scientist for Magnetism
Mr. T. Keating, GSFC Advance Missions Analysis Office

GEOPOTENTIAL RESEARCH MISSION



GRM

iv

CONTENTS

Section	Page
1. INTRODUCTION	1
1.1 Purpose	1
1.2 Limitations of Present Knowledge	4
1.2.1 Gravity Field	4
1.2.2 Magnetic Field	5
2. SCIENTIFIC RATIONALE	7
2.1 Executive Summary	7
2.2 Introduction	8
2.3 Dynamics and Structure of the Continents	10
2.4 Dynamics and Structure of the Subocean Crust and Lithosphere	20
2.5 The Deep Interior	21
2.5.1 The Mantle: Convection and the Gravity Field	21
2.5.2 The Core: Generation of the Magnetic Field	24
2.6 Ocean Circulation	26
2.7 Other Applications	28
2.7.1 Aeronomy	28
2.7.2 External Magnetic Field	29
2.7.3 Orbit Computation and Geodesy	30
2.8 Coordination of GRM with Other Missions and Studies	30
2.9 Concluding Remarks	33
3. SPACEFLIGHT MISSION DESCRIPTION	35
3.1 Scientific Requirements	35

CONTENTS (Continued)

<u>Section</u>		<u>Page</u>
3.1.1	Gravity	35
3.1.2	Magnetic	35
3.2	Mission Description	37
3.3	Orbit Selection	38
3.3.1	Gravity Mission	38
3.3.2	Magnetic Mission	41
3.4	Tracking Coverage and Accuracy	43
3.4.1	Doppler Tracking Network	43
3.4.2	Tracking Data Relay Satellite System	44
3.5	Doppler Network Data Collection	45
3.6	Launch and Descent Phase	46
4.	MISSION DATA REDUCTION PROCESS	49
4.1	Data Flow System	49
4.2	Flight Data	50
4.2.1	Range Rate (\dot{s}) Determination	50
4.2.2	Magnetic Field Determination	51
4.3	Gravity Model Determination	52
4.3.1	Model Representation	52
4.3.2	Method of Determination (Estimation)	55
4.3.3	Resolution of Spherical Harmonics and Error Estimation	57
4.3.4	GEOID Error and Gravity Anomaly Error	59
4.4	Magnetic Field Model Determination	61

CONTENTS (Continued)

<u>Section</u>	<u>Page</u>
4.4.1.1 Magnetic Anomaly Field Determination	62
5. SPACECRAFT DESIGN	65
5.1 A-1 and A-2 Spacecraft Characteristics	65
5.2 Satellite-to-Satellite Tracking System	69
5.2.1 Transmit Frequency and Ionospheric Effects	71
5.2.2 Antenna Configuration	73
5.3 Disturbance Compensation System Performance	80
5.4 Disturbance Compensation System Instrument Design	83
5.5 Propulsion	86
5.5.1 Propulsion Subsystem	86
5.5.2 Aerodynamic Drag Analysis and Fuel Consumption	89
5.6 Power Subsystem	91
5.7 Thermal Subsystem	94
5.8 Structure Subsystem	95
5.8.1 Spacecraft	95
5.8.2 Launch Cradle	98
5.8.3 Materials	100
5.9 C&DH and TDRSS Tracking Subsystem	101
5.10 DMA Tracking System	103
5.11 Onboard Data Processing	105
5.11.1 Housekeeping and Command Data	105
5.11.2 Scientific Data	106
5.11.3 Flight Controller	107
5.12 Total Spacecraft s Error	108

CONTENTS (Continued)

<u>Section</u>	<u>Page</u>
6. CRITICAL SUBSYSTEM DEVELOPMENT	111
6.1 Satellite-to-Satellite Tracking System	111
6.1.1 Component Testing	111
6.2 Guidance and Control Simulation	116
6.2.1 Equations of Motion	118
6.2.2 Control Laws	120
6.3 Guidance and Control Subsystem	126
6.3.1 Attitude Control Configuration	126
6.3.2 Onboard Computer	126
6.4 Proof-Mass Roundness and Center of Mass	126
6.4.1 Ball Roundness	126
6.4.2 Ball Mass Center Offset	128
6.5 Mass Attraction	129
6.6 Critical Design	130
6.6.1 DISCOS Performance	130
6.6.2 Satellite-to-Satellite Tracking System	132
6.6.3 Atmospheric Drag and Fuel Consumption	132
6.6.4 Propulsion Tank Availability	143
6.6.5 Scalar Magnetometer Life and Stability	143
6.6.6 Vector Magnetometer Axis Alignment	143
6.6.7 Onboard Flight Controller System	144
6.7 Data Reduction	144

CONTENTS (Continued)

<u>Section</u>	<u>Page</u>
6.7.1 Pre-Processing of SST Data	144
6.7.2 Gravity Field Computation Efficiency	145
6.7.3 Magnetic Field Model Computation	148
6.7.4 Computational Summary	151
8 Alternate Designs	151
6.9 International Cooperative Ventures	153
6.9.1 POPSAT Program	153
6.9.2 GRADIO Gradiometer	153
7. MISSION DATA	155
7.1 Data Flow and Data Handling	155
7.2 Data Storage/Availability	155
8. SCIENTIFIC ANALYSIS OPPORTUNITIES	159
9. PROGRAM SCHEDULE	161
10. SUMMARY OF GRM REPORT	163
11. REFERENCES	165
APPENDIX A--ACRONYM LIST	A-1
APPENDIX B--DEFINITION OF TERMS	B-1
APPENDIX C--MAJOR CONTRIBUTORS TO GRM REPORT	C-1
APPENDIX D--BIBLIOGRAPHY	D-1

ILLUSTRATIONS

Figure

	Page
GRM	iv
1-1 GRM Flight Profile	1
1-2 Gravity and Magnetic Simulations	3
1-3 Core Field Schematic	5
2-1 Magnetic Anomaly Field at 160 km Altitude	13
2-2 Rio Grande Rift, Gravity	15
2-3 Rio Grande Rift, Magnetics	15
2-4 Yellowstone, Gravity	16
2-5 Yellowstone, Magnetic	16
2-6 Alps, Gravity (Free-air)	17
2-7 Williston Basin, Gravity	18
2-8 Williston Basin, Magnetics	18
2-9 GEOIDS from Spherical Harmonic Degrees 2 Through 6	23
3-1 Definition of \dot{s}	38
3-2 Gravity Anomaly Sensing at Two Altitudes	39
3-3 Truncation Effect of GRM \dot{s} Value Beyond Degree L	40
3-4 Relative Magnetic Anomaly Amplitude as Observed at Spacecraft	42

ILLUSTRATIONS (Continued)

<u>Figure</u>		<u>Page</u>
3-5	Resolution of Magnetic Anomaly as a Function of Altitude	42
3-6	DMA Network of Doppler Tracking Stations, Solid Discs Denote TRANET . . .	43
3-7	TDRSS Zone of Exclusion	44
3-8	GRM Doppler Network Coverage	45
3-9	GRM Deployment	47
4-1	GRM Data Flow System	49
4-2	Geometry for Stokes' Equation	55
4-3	Gravity Signal Power to Noise Spectrum	57
4-4	Local GEOID for Simulation	60
5-1	GRM Orbit Configuration (A-1)	67
5-2	GRM Spacecraft Body	68
5-3	Simplified GRM SST System	69
5-4	GRM Satellite-to-Satellite Tracking System	70
5-5	GRM Ionospheric Range and Range/Rate Error	72
5-6	GRM Horn Antenna	74
5-7	Spacecraft Separation versus Angle Off Axis	75
5-8	Allowable Mass-center to Antenna Phase-center Error	76

ILLUSTRATIONS (Continued)

Figure

	Page
5-9 Simplified GRM SST System	78
5-10 SST Phase Jitter Cancellation	79
5-11 GRM DISCOS Ball-to-Ball Range Relationship	80
5-12 GRM DISCOS Design	84
5-13 GRM DISCOS Schematic Diagram	84
5-14 GRM Propulsion Schematic Diagram	87
5-15 Predicted Solar Flux at 10.7 cm Wavelength	90
5-16 GRM Daily Fuel Consumption	91
5-17 Solar Array Emphasis; GRM Orbit Configuration	92
5-18 Operating Points for Peak-Power Tracker	93
5-19 Power versus Load	93
5-20 GRM Internal Configuration	96
5-21 GRM-stowed Configuration	97
5-22 GRM A-1 Boom Deployment	98
5-23 GRM/Orbiter Deployment Concept	100
5-24 GRM A-2/Orbiter Deployment Concept	100
5-25 GRM Spacecraft: Telemetry/Command/Range and Range Rate Block Diagram . .	102

ILLUSTRATIONS (Continued)

<u>Figure</u>		<u>Page</u>
5-26	DMA Tracking Subsystem Block Diagram	105
6-1	Frequency Stability at 91.1 GHz	111
6-2	GRM Satellite-to-Satellite Tracking System (SST) Motion Experiment . . .	112
6-3	SSTV Demonstration System	114
6-4	SST Measurement Noise versus Averaging Time	115
6-5	Rate Noise During a Constant Velocity Ramp	116
6-6	GRM Guidance and Control System Functional Block Diagram	117
6-7	Notation for General Dynamic Equations	118
6-8	DISCOS Sensor Model	120
6-9	Desired In-track Limit Cycle	122
6-10	In-track Thruster Control Law	123
6-11	Cross-track Thruster Control Law	123
6-12	Proof-mass 1-Axis Phase Plane	124
6-13	Proof-mass Coordinate History (Without BCA)	124
6-14	Proof-mass Coordinate History (With BCA)	125
6-15	Harmonic Analysis of Roundness Errors--Typical Proof-mass	127
6-16	DISCOS Error Due to Proof-mass Roundness Errors	127

ILLUSTRATIONS (Continued)

Figure

6-17	Acceleration Due to a 10 kg Mass of Fuel Imbalance	130
6-18	Two-Stage DISCOS	131
6-19	Reflected N_2^+ Ion Stream Pattern from Molybdenum with Impact Energy of (a) 1 eV, (b) 4 eV, (c) 8 eV, and (d) 16 eV	134
6-20	Reflected Ion Stream Pattern from Molybdenum with (a) $\theta_i = 30^\circ$, (b) $\theta_i = 85^\circ$, and Two Energy Levels	135
6-21	Fractional Momentum Transfer with (a) $\theta_i = 80^\circ$ and (b) $\theta_i = 85^\circ$	136
6-22	Gas to Surface Momentum Transfer	137
6-23	SST Correction Data Flow	145
7-1	Ground Control and Data-processing Block Diagram	156
9-1	GRM Program Milestone Schedule	161

TABLES

<u>Table</u>		<u>Page</u>
1-1	Measurement Requirements vs. Geological Features	2
2-1	GEOID Accuracies	27
2-2	Ocean Currents Scale Sizes	27
3-1	Magnetic Accuracy Requirements (RMS)	36
4-1	GRM Error Analysis	59
4-2	GRM Simulation Errors for a 5° x 5° Region in the Tonga Trench	61
5-1	GRM Spacecraft Characteristics	65
5-2	Doppler Antenna Performance	74
5-3	TRIAD/GRM Parameters Value Comparison	85
5-4	GRM Fuel Budget Summary	91
5-5	Power Load Budget	93
5-6	Boom Design Data	99
5-7	GRM Estimated Weights	99
5-8	GRM Data Rates	101
5-9	GRM Link Margin Data	103
5-10	GRM/DMA Subsystem Characteristics	104

TABLES (Continued)

Table

5-11	GRM Housekeeping Data	<u>Page</u>
5-12	Spacecraft-to-Spacecraft Velocity Errors	106
6-1	Drag-Force Related Dimensions	109
6-2	adj CDj Drag-Force Components	139
6-3	Mathematical Computations for the Least Squares Gravity Matrix	141
6-4	Number of Mathematical Computations	147
		152

SECTION 1. INTRODUCTION

1.1 PURPOSE

The purpose of the Geopotential Research Mission (GRM) is to map the global gravity and magnetic fields to a half wavelength of 100 km. Two spacecraft will be placed by the Space Transportation System (STS) in coplanar polar circular orbits at an altitude of 160 km (in tandem) with a separation of 150 to 550 km (Figure 1-1).

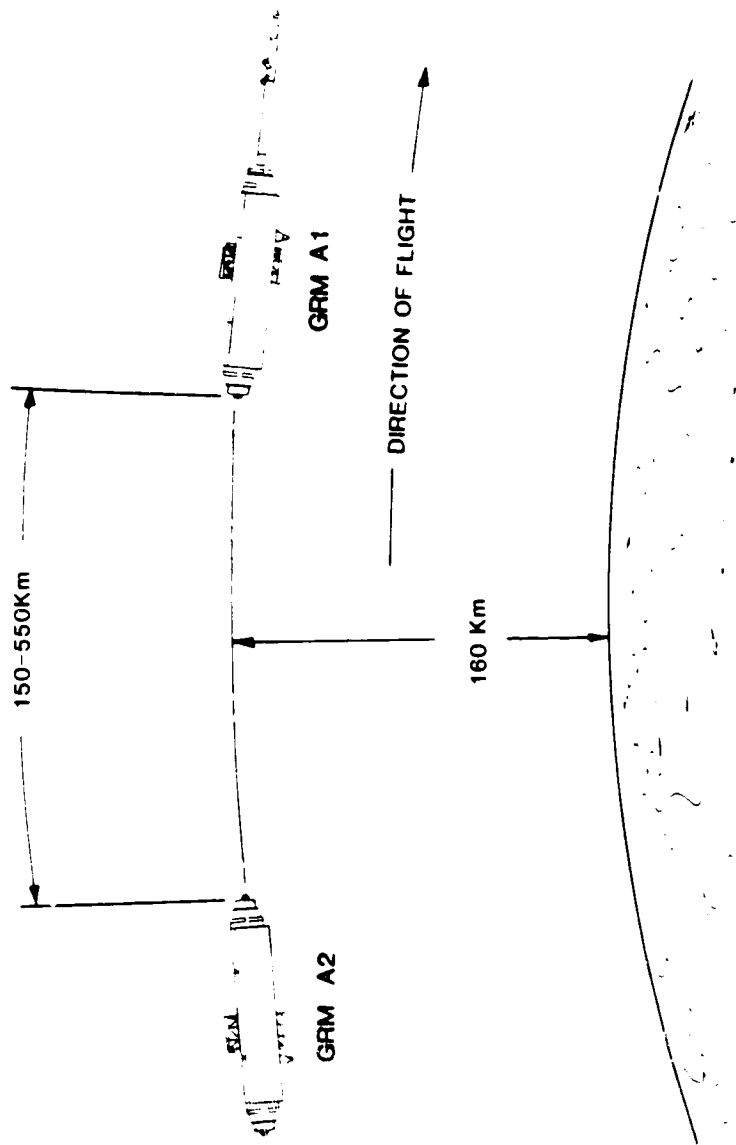


Figure 1-1. GRM Flight Profile

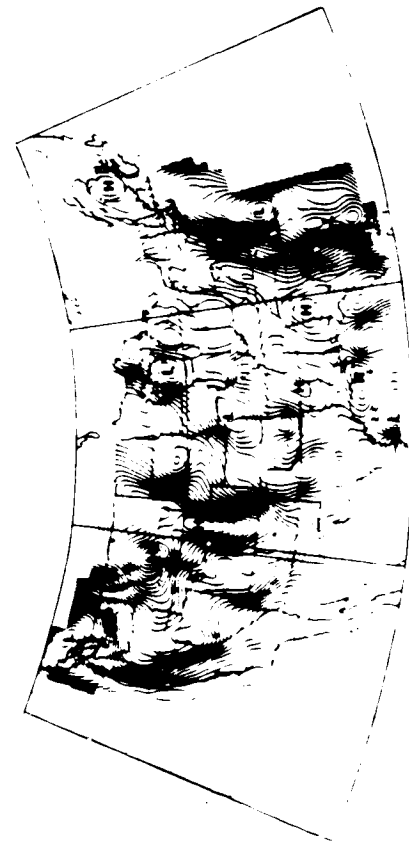
To obtain the gravity field, the relative velocity between these two satellites is measured and the gravity potential computed. By subtracting a reference potential, the short wavelength or crustal anomaly field is determined and can be mapped. The relative velocity variations must be measured with an accuracy of 1-micrometer per second over a 4-second averaging time. This process will produce a field of 2.5 milligal accuracy ($1 \text{ milligal} = 10^{-5} \text{m/s}^2$) and a 0.1 meter geoid at a 100 km resolution.

The gravity field obtained using the satellite produced data will meet requirements for studies of geologic structures recommended by national scientific communities as shown in Table 1-1 and discussed in "Scientific Rationale for the Geopotential Research Mission" (Section 2).

Table 1-1
Measurement Requirements vs. Geological Features

Feature Type	Wavelength (km)	Accuracy (mgal)
Sedimentary Basins	10-300	3-6
Batholiths	20-300	3-6
Mountain Ranges	20-1000	8-10
Subduction Zones	50-1000	10-12
Shields	50-800	2-3

Two magnetometers, one a scalar and the other, a vector tri-axial fluxgate, will be used to measure both the total field and the component field. In order to avoid spacecraft magnetic field contamination, these instruments will be deployed on the end of a five-meter-long boom extending forward of the lead satellite (Figure 1-1). Four solid-state star cameras are mounted on the boom near these magnetometers to provide attitude information. This instrumentation provides a mission absolute accuracy of 2 nanoteslas (scalar) and 5 nanoteslas (vector) with an attitude accuracy of orientation to 20 arc-seconds. These field values will have the same resolution as the gravity field; 100 km horizontal, half wavelength. A simulation of the short wavelength gravity and magnetic crustal anomaly fields was produced (Figure 1-2) by projecting the known Earth surface anomaly fields over the U.S. to the mission altitude of 160 km. Detailed interpretation of the crustal anomalies, mapped on a global scale, will allow significant analysis of major tectonic features (Figure 1-2).



a. Free-air gravity data over the United States (data from U.S. Geological Survey) computed at 160 km altitude. Contour interval is 1 mgal.



b. Magnetic anomaly field data (USGS/SEG) over the United States computed at 160 km altitude with major geologic/tectonic features superimposed (based on King 1977).

Figure 1-2. Gravity and Magnetic Simulations

Removing a magnetic core or main field model yields the crustal anomaly field. An accurate and updated main field model will be provided by mapping the low-order field harmonics ($n < 12$ or 13). Like the Magsat field model (Langel, 1982), this GRM derived core field will play a major part in revising the International Geomagnetic Reference Field (IGRF, Peddie 1983).

1.2 LIMITATIONS OF PRESENT KNOWLEDGE

1.2.1 GRAVITY FIELD

Knowledge of the gravity field is fundamental to understanding the dynamics of the Earth. Accurate gravity data is an essential requirement that must be made available on a worldwide basis. Gravity data recorded at the Earth's surface are of high accuracy, but these measurements do not cover more than 20 to 30 percent of the globe. Comparison of available gravity data with surface geological features has produced a general agreement between oceanic ridges and island arcs, but the accuracy and detail needed to allow precise correlations are lacking.

Currently, the National Aeronautics and Space Administration's (NASA's) gravity modeling program is based on the analysis of satellite tracking data, in conjunction with satellite altimetry and surface gravity measurement data. With these data, significant improvements to the model of the Earth's gravity field have been obtained. These models of the geopotential still lack the accuracy and resolution to resolve fundamental problems on the origin and structure of geological features on the Earth's surface, the mechanical properties of the Earth's lithospheric plates, and large-scale circulation of the oceans and major current systems. A particular limitation is the inadequately mapped regions that include the tectonic areas such as the collision zones of the Andes and the Himalayas.

Contemporary gravity field models determined through satellite orbit dynamics, surface gravity, and satellite altimetry data have provided gravity field information of sufficient accuracy and detail on a worldwide basis so that tentative correlations with surface features can be made. It is essential that the global geopotential extend to the much shorter wavelengths (approximately 100 km) so that the structure, composition, and physical state of the lithospheric crust and surface topography can be studied.

The GRM will sense the gravity field fine structure, and therefore, provide knowledge and understanding of: (1) the origin and structure of geological features on the Earth's surface; (2) the mechanical properties of the Earth's lithospheric plates

and the forces that may drive their motion; and (3) the large-scale circulation of the oceans and major current systems by the determination of an improved ocean geoid.

The GRM will provide the baseline for the NASA gravity program for the 1990's. The observational data obtained from this mission will give greater accuracy and resolution for developing the gravity field and geoid models. The geoid produced from GRM data will be used as the reference surface for ocean circulation and current studies.

1.2.2 MAGNETIC FIELD

The energy of the Earth's magnetic field falls into three ranges; long wavelength (core field), shorter wavelength (anomaly), and shortest wavelength (external variations). The main or core field is continuously changing, and until an adequate predictive model for this secular variation can be derived, any extension of main field models beyond the epoch of the last satellite mission are subject to considerable error (Figure 1-3).

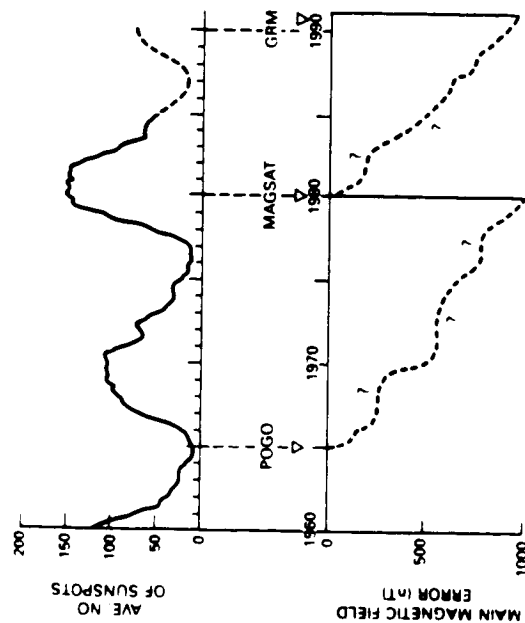


Figure 1-3. Core Field Schematic

Schematic representation of the decay in the knowledge of the changing magnetic-core field with time. Only past and future missions give meaningful reference points.

Errors in the core field result in an inaccurate reference field being removed from the observed magnetic measurements to produce a magnetic anomaly map. These main field inaccuracies cause anomaly resolution and interpretation errors.

The Geopotential Research Mission (GRM) Science Steering Group studied requirements for measuring the core field by comparing the results from the MAGSAT data with the secular variations. The perishability and the variations of the core field data as reported by the Magnetic Field Survey Working Group, "A Satellite Mission to Measure the Geomagnetic Field and its Secular Change," (Figure 1-3), January 1984, emphasizes the required measurement. As stated in the same report, "knowledge of the Earth's magnetic field and its secular change elucidates processes deep within the Earth at the core-mantle boundary (Backus, 1983)." To determine the crustal anomalies, it is necessary to remove the secular terms (up to degree 13) from the spherical expansion. Since the secular terms dominate the expansion, the ability to determine the crustal terms (degree 13 to 23) is directly related to the accuracy of the measurement of the core field.

Core field knowledge limitations have the following impact on the state of knowledge of the Earth:

- Studies of geomagnetic variation yield information about the deep electrical conductivity structure that cannot be obtained in any other way. Relatively rapid variations can yield information about lateral variations in conductivity for depths shallower than the 650 to 670 km seismic discontinuity in the mantle. These variations might give clues about the temperature and mantle convection patterns that may drive continental drift. Some authors suggest that phase changes occur at this depth; others suggest that there is a compositional change. A simple phase change would imply whole mantle convection, whereas a compositional change indicates two-layer convection (Lees, 1983).
- In the lower mantle, electrical conductivity values might indicate how much the magnetic signal from the outer core has been filtered before reaching the surface. This phenomenon may explain the correlation that has long been observed between variations of the length of the day and the field variation (Vestine, 1953). This correlation has been the subject of recent analysis (Courillot and others, 1982). Other scientists have correlated length of day variations to the average temperature over the surface of the Earth (Lamb, 1977).

SECTION 2. SCIENTIFIC RATIONALE

A Science Steering Group (SSG) defined for NASA both the scientific basis and the measurement requirements for the GRM. The SSG, cochaired by W. M. Kaula and C.G.A. Harrison, authored a report titled, "The Geopotential Research Mission Scientific Rationale." The original SSG February 1983 report has been revised by the cochairmen of the SSG in August 1985 and this edition is contained in this section. To ensure consistency throughout the document this material has been reformatted but not edited. However, some technical and programmatic changes have been made. Note that some of the material contained in this section may be repeated in other sections.

2.1 EXECUTIVE SUMMARY

The Geopotential Research Mission (GRM) is designed to measure variations in the gravity and magnetic field over the entire globe to a resolution of 100 km with unprecedented completeness and accuracy. The mission consists of two drag-free satellites at 160 km altitude in polar orbits, linked by precise Doppler.

Satellite altimetry has brought revolutionary advances in understanding the suboceanic solid Earth. GRM will extend this revolution to the study of the structure and evolution of the continents through gravity and magnetic measurements. The mission will give the first comprehensive coverage of the areas of greatest tectonic interest: the collision belts of the Himalayas and the Andes, and rift zones such as that in East Africa. Most of these areas cannot be surveyed by any other means. Understanding these major formational processes is essential to comprehending the state and evolution of the continents. GRM will also contribute to understanding of the suboceanic solid Earth through greatly improved coverage of both gravity and magnetic fields at the continental edges, which are important to ocean crust and lithosphere evolution, and of the magnetic field in the southern hemisphere and polar regions.

GRM will give profound insight into the deep interior of the Earth. The gravity field will elucidate the pattern and energetics of the thermal convection in the mantle which drives the plate motions. The magnetic field and its temporal variation will constrain models of the geodynamo in the fluid outer core.

GRM is essential to the full utilization of the next generation of altimetric satellites, the Topography Experiment (TOPEX), by providing the geoid to which sea surface heights are referred for studies of oceanic circulation.

Further applications of GRM are: (1) study of the lower thermosphere (taking advantage of its 160 km altitude); (2) study of externally generated variations of the magnetic field; (3) study of upper mantle conductivity; (4) improvement of orbit computation accuracy; and (5) improvement of reference frames for geodesy.

The GRM will, like the Venus Radar Mapper (VRM), contribute importantly to the ongoing comparative study of the terrestrial planets.

2.2 INTRODUCTION

The GRM will measure the gravity and magnetic fields of the Earth at an altitude of 160 km. The minimum lifetime of the mission will be six months, which will give an average spacing between orbits at the equator of about 7 km. The DISCOS System will make the orbit drag-free. The perturbations of the gravity field will be inferred from range-rates between the satellites, while the scalar and vector magnetic field will be measured by standard magnetometers. The spacecraft orientation will be measured by star cameras. The anticipated accuracies and resolutions are: 2 milligauss (2 x 10⁻⁵ m/sec²) and 100 km for the gravity field; 2 nanotesla and 100 km for the magnetic field (Goddard Space Flight Center, 1982).

In the Fall of 1983, the NAS briefed the Science Advisor to the President, Office of Science and Technology Policy, on research in the solid earth sciences. The briefing panel identified five research areas "...in which significant dividends can be expected as a result of incremental federal investment...". One of these areas was satellite geodesy which was further subdivided into the GPS and gravimetric systems. Concerning the gravimetric systems, the briefing panel stated:

"Satellite altimetry (measuring the elevation of the sea surface) recently has been used to construct maps of gravity anomalies in the oceans. These anomalies demonstrate, for example, that fracture zones are much more profound features than had previously been recognized, and they provide direct evidence for shallow convection in the mantle. These measurements will be continued by TOPEX, which is designed principally for oceanographic purposes. The resolution of these measurements can be improved by the systematic measurement of the gravity field from space, as proposed in the Geopotential Research Mission (GRM) of NASA. In addition, a mission such as this can extend high-resolution gravity (and magnetic) measurements in the continents. The value of this mission in providing global gravity coverage and better orbital data for TOPEX and other earlier missions make it an attractive opportunity for an early start."

In the Spring of 1985, there was a second research briefing by NAS on remote sensing from space. The briefing panel stated as its first recommendation that "high priority be given to the Earth Science Missions TOPEX and GRM for new starts in FY 1987 and FY 1988". The report later emphasizes the oceanographic, tectonophysical, and geomagnetic requirements for GRM.

An earlier NAS study, the SSB report "A Strategy for Earth Science from Space in the 1980's; Part I: Solid Earth and Oceans" (Committee on Earth Sciences, 1982) summarized the scientific goals for earth science into eleven categories. Measurements by GRM would contribute significantly to four of these goals: III, Ocean Dynamics; VII, Plate Dynamics; X, Internal Structure and Composition of the Earth; and XI, Generation of the Earth's magnetic field. The rationale presented here is cast into a framework of objectives of which the first four are essentially a reorganization of those in the SSB report. In addition, the GRM will contribute to the aeronomy of the lower thermosphere, the study of the external magnetic field, orbit computation, and geodesy. Finally, it was discussed how GRM should be coordinated with other space missions and related scientific efforts in the coming decade.

The headings are:

- 2.3 DYNAMICS AND STRUCTURE OF THE CONTINENTS
- 2.4 DYNAMICS AND STRUCTURE OF THE SUBOCEAN CRUST AND LITHOSPHERE
- 2.5 THE DEEP INTERIOR
 - 2.5.1 THE MANTLE: CONVECTION AND THE GRAVITY FIELD
 - 2.5.2 THE CORE: GENERATION OF THE MAGNETIC FIELD
- 2.6 OCEAN CIRCULATION
- 2.7 OTHER APPLICATIONS
 - 2.7.1 AERONOMY
 - 2.7.2 EXTERNAL MAGNETIC FIELD
 - 2.7.3 ORBIT COMPUTATION AND GEODESY
- 2.8 COORDINATION OF GRM WITH OTHER MISSIONS AND STUDIES
- 2.9 CONCLUDING REMARKS

Like all subdivisions of a continuum, the organization into 2.3, 2.4, and 2.5 is somewhat arbitrary. This organization reflects scientific communities and data availability as well as natural properties; some say the interaction of mantle convection with the continents will dominate the new findings, and hence should be given primary emphasis.

2.3 DYNAMICS AND STRUCTURE OF THE CONTINENTS

The plate tectonic revolution had its birth in the ocean, and considerable progress continues to be made in understanding the structure and dynamics of the suboceanic crust and lithosphere, but it is certainly the informed consensus that the most important area for study now is the continents. By "continents" we mean not only the continental crust, but also the upper mantle to at least 200 km depth, since there appear to be perceptible variations to such depths, including systematic differences between subcontinental and suboceanic regions.

The structure and tectonics of the continents are currently topics of great debate. In the past, the support of continental features--mountains, basins, etc. -- has generally been explained as arising from passive mechanisms: the elastic strength of the lithosphere, or isostasy: the balancing of surface loads by loads at depth (usually shallow) of opposite sign. However, there is a growing realization that in many places loads are sustained dynamically: particularly loads of extent to which GRM will be sensitive: 100 km or more. This dynamic support is a manifestation of mantle convection, which also is the process underlying plate tectonics. However, convection is a broad term, meaning any motion of matter arising from density heterogeneities, and it can take several forms.

Gravity and magnetic data giving at least as much detail as GRM are available for the coterminous USA and most of Canada, Europe, and Australia, but not for the remaining 80% of the Earth's land area. Some of this four-fifths has been measured, but the data are not available for scientific research. Unfortunately, the inadequately mapped regions include most of the highly interesting tectonic areas such as the collision zones of the Andes and the Himalayas.

The 1982 SSB Report "A Strategy for Earth Sciences from Space in the 1980's" gave as a primary scientific objective "To measure the Earth's gravitational field from global scales to wavelengths of 200 km or less," and stated that "determination of an improved gravitational field through space measurement should be an objective of highest priority...." The reason for the emphasis on determination over a great range of wavelengths is partly the great variety of features to whose interpretation gravity can contribute; on the continents, features such as mountain ranges, sedimentary basins, rifts and shield areas. But the reason is also that the support mechanisms associated with a particular structure can be inferred only if there is information from a broad spectral range. In general, continental features of limited extent are supported more by the flexural rigidity of the lithosphere than are broad features, while geologically older

features tend to be supported more by flexure than younger features. Over less rigid areas, the gravity field reflects sublithospheric properties; whereas over more rigid areas, it reflects more the thermo-mechanical properties of the lithosphere.

The response properties of the lithosphere to surface loads is only part of the picture. To create collisional mountain ranges, uplifted plateaus, sinking basins and offset faults, driving forces are required. Normally, these forces are generated by mantle convection, as mentioned. Sometimes, a relatively simple assumption can be made about the underlying forces, based on plate tectonics or other broad constraints, and the problem becomes estimation of the details of response of the continental crust and lithosphere. Often these details depend on past history; tectonic phenomena tend to occur where previous events have created an obstacle. The most evident example is a subduction zone, where oceanic lithosphere sinks because the continent is more buoyant.

Emphasis has been given to the wavelengths of features in the gravitational field. But there must also be signals above a measurable threshold in order for geophysical interpretation to be made. This question was addressed by the GRAVSAT Users Working Group, which in its August 1980 report produced a table including the following continental features:

Feature Type	Wavelength (km)	Accuracy (mgal)
Sedimentary Basins	10-300	3-6
Batholiths	20-300	3-6
Mountain Ranges	20-1000	8-10
Subduction Zones	50-1000	10-12
Shields	50-800	2-3

$$(1 \text{ mgal} = 10^{-5} \text{ m/sec}^2)$$

These accuracies are within the capability of GRM for wavelengths of about 200 km or more. To extract information about these features in the presence of stronger signals from the mantle will require considerable spectral filtering, but the 2 to 3 mgal GRM system should obtain significant scientific information concerning these structures.

The magnetic field at wavelengths less than about 3000 km is generally believed to be caused by sources within the crust and upper mantle. However, there are difficulties in accounting for all of the fields shorter than this wavelength using crustal sources

because of the required strength of these sources, which exceeds the magnetic strength of materials studied in the laboratory. Possible resolutions of this difficulty are to call for significant upper mantle sources or to suppose that some of the signal of wavelength shorter than 3000 km is produced in the core of the Earth. This is discussed in paragraph 2.5.2.

Physically, there might be a connection between the magnetic anomaly field and the gravity field if, for instance, the magnetic susceptibility of the crustal rock is directly related to the density. In actuality, this correlation is masked by many complications. The value of the shorter wavelengths of the magnetic field thus tends to be the empirical one of highlighting geologic structures which otherwise would be obscured by the effects of erosion and sedimentation, such as the large positive anomaly in Kentucky and Tennessee (Figure 2-1), which marks the site of a Precambrian rift. In tectonically stable areas, such as shields, gravity anomalies have the same property. If the lithosphere is cold and thick enough, it can support features of a few tens of kilometers in dimension almost indefinitely.

In younger continental crust, magnetic anomalies are often controlled by the thickness of the crustal material which is below the Curie temperature of the magnetic minerals, and therefore reflect the pattern of heat flow.

Failed rifts (aulacogens) and their associated hot spot swells are of particular interest, since they are the sites of intense volcanism, and of mineral accumulations and petroleum deposits. The Rio Grande Rift shows as a prominent negative in Figure 2-2 from northwest New Mexico up along the Colorado/Utah border. This rift does not show up as well on the short wavelength magnetic anomaly map (Figure 2-3) as on the unfiltered map (Figure 2-1). Other rifts in the United States have been discovered using surface gravimetry and aerial magnetometry and have been inferred on other continents from MAGSAT data. A combination of the gravity field and magnetic field measurements by GRM would allow many more continental rifts to be discovered, modelled, and their geologic evolution inferred. The Yellowstone Region, Figures 2-4 and 2-5, is another example of a hot spot swell.

(5 nT CONTOUR INTERVAL)

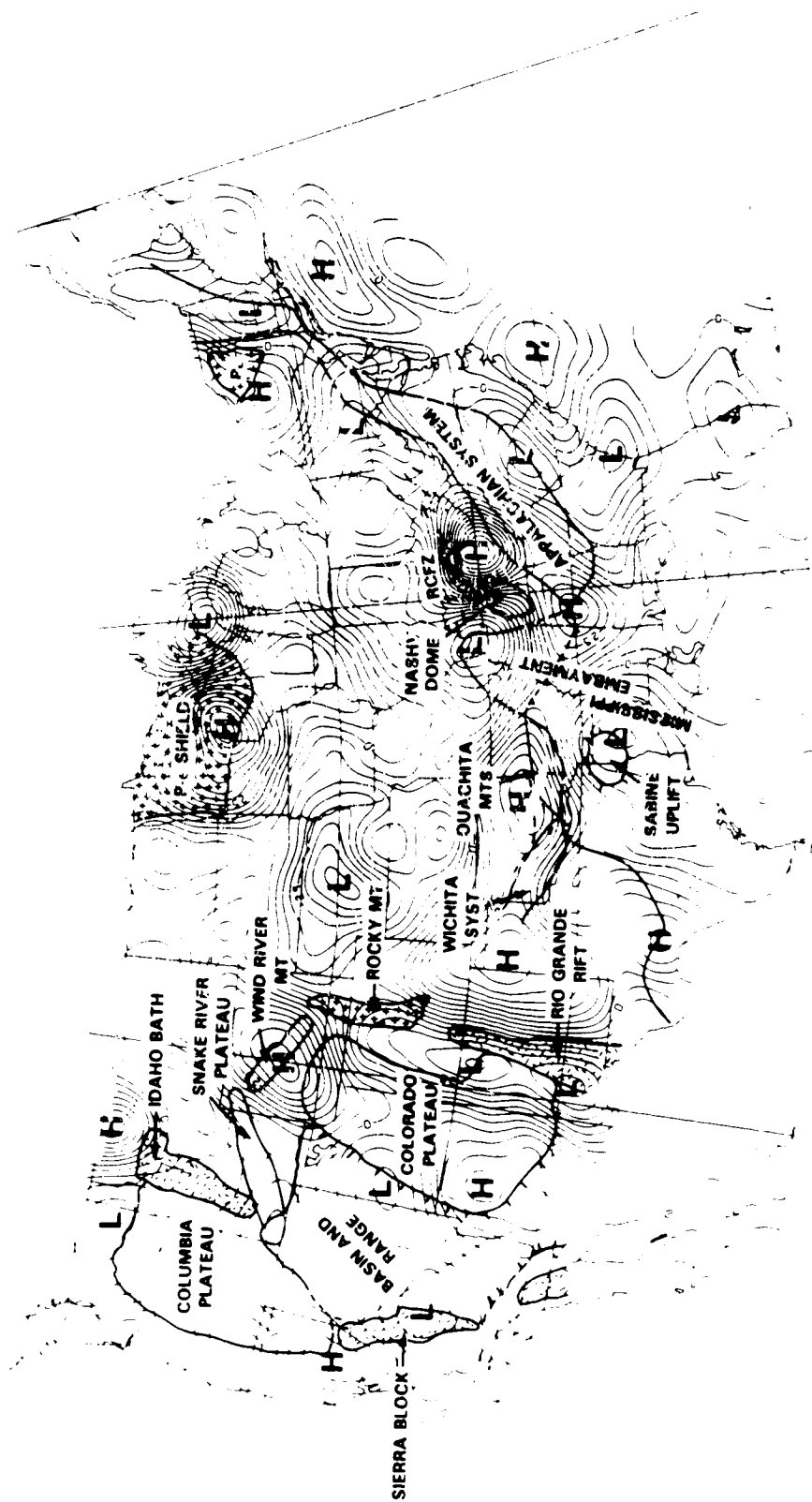
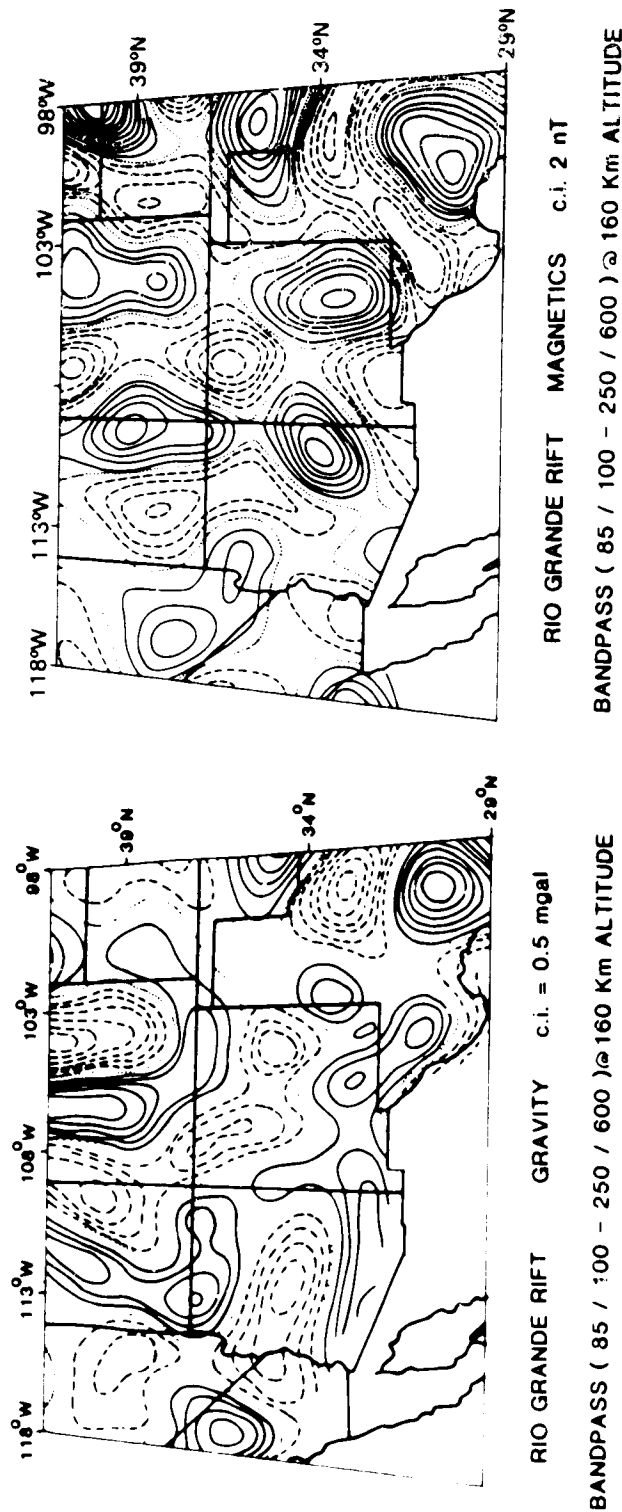


Figure 2-1. Magnetic Anomaly Field at 160 km Altitude

Mountain ranges show impressive variations in their gravitational signature. For example, the Alps and the Appalachians correlate with belts of positive and negative gravity anomalies with widths of a few tens to a few hundreds of kilometers and amplitudes up to 100 milligals (see Figure 2-6). This negative-positive anomaly "couple" has recently been interpreted in terms of the mass loads that act on the lithosphere during mountain building and the flexural properties of the lithosphere. The positive anomalies appear to arise from buried loads, such as obducted "flakes" of crust, which developed on the leading edge of the underthrust plate during the mountain building. The negative anomalies seem explicable as resulting from flexing of the lithosphere in response to both surface and subsurface loads, such as fold-thrust sheets. By comparing the amplitude and wavelength of the observed gravity anomaly "couple" to calculated profiles based on various flexural models, it has been possible to estimate the flexural rigidity of continental lithosphere under mountain ranges. Thus, for example, the Appalachians appear to have an appreciably greater lithospheric strength than the younger Alps. These estimates of lithospheric strength and their relationship to the age of the "basement" and age of the orogeny provide important information on the rheology of the lithosphere. Because mountain ranges are of such large dimensions, GRM should enable us to estimate flexural properties of the continental lithosphere in their vicinity.

Sedimentary basins are significant as to the location of petroleum and mineral deposits. The thermotectonic history of a sedimentary basin such as those of the North Sea, Alberta, and the Williston Basin (see Figures 2-7 and 2-8) is a complex interaction of loading, cooling, and flexure. Gravity measurements have contributed greatly to understanding the role of flexure in the evolution of basins. It appears feasible for GRM to resolve significant features in relatively large high-rigidity continental basins, such as the Appalachian and Ganges Basins.



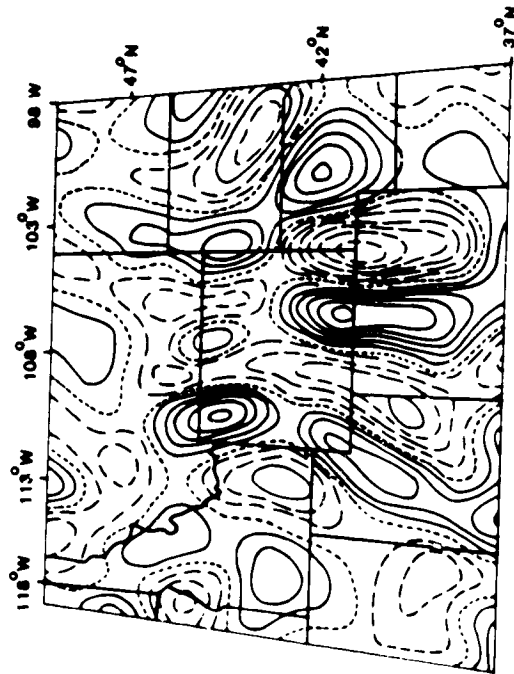
(P. T. Taylor, Written Communication, 1985)

(P. T. Taylor, Written Communication, 1985)

Figure 2-2. Rio Grande Rift, Gravity Figure 2-3. Rio Grande Rift, Magnetics

The Rio Grande Rift is an intraplate extensional feature reaching from West Texas northward into Colorado. It consists of a series of aligned grabens, associated with low level seismicity, Cenozoic volcanism, and thick accumulations of young alluvial sediments. The structure is reflected in the topography of New Mexico and Colorado; the grabens being flanked by prominent mountains such as the Sangre de Cristo Range. The Rio Grande Rift is generally interpreted as a zone of incipient but very slow continental fragmentation; extension rates are probably under 1 cm/yr.

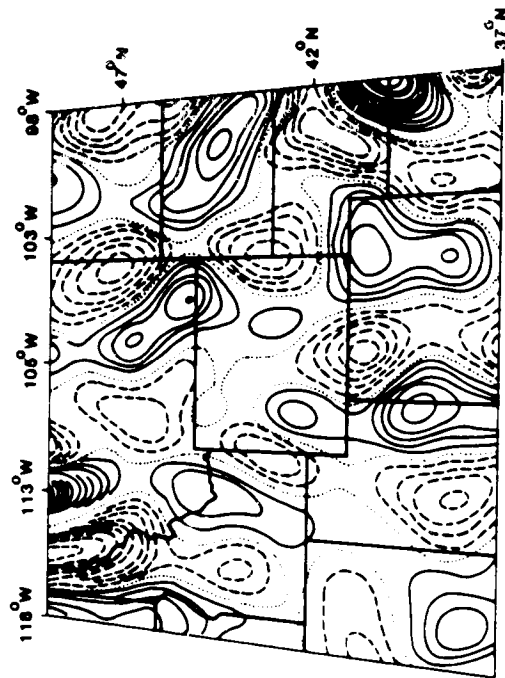
There is a well developed low magnetic anomaly of some -10 nT extending linearly, from the New Mexico-Mexican border into Colorado. The gravity anomaly is not as developed. (Note: All gravity discussions refer to free-air anomalies.)



YELLOWSTONE GRAVITY c.i. = 0.5 mgal
BANDPASS (85 / 100 - 250 / 260) @ 160 Km ALTITUDE

(P. T. Taylor, Written Communication, 1985)

Figure 2-4. Yellowstone, Gravity



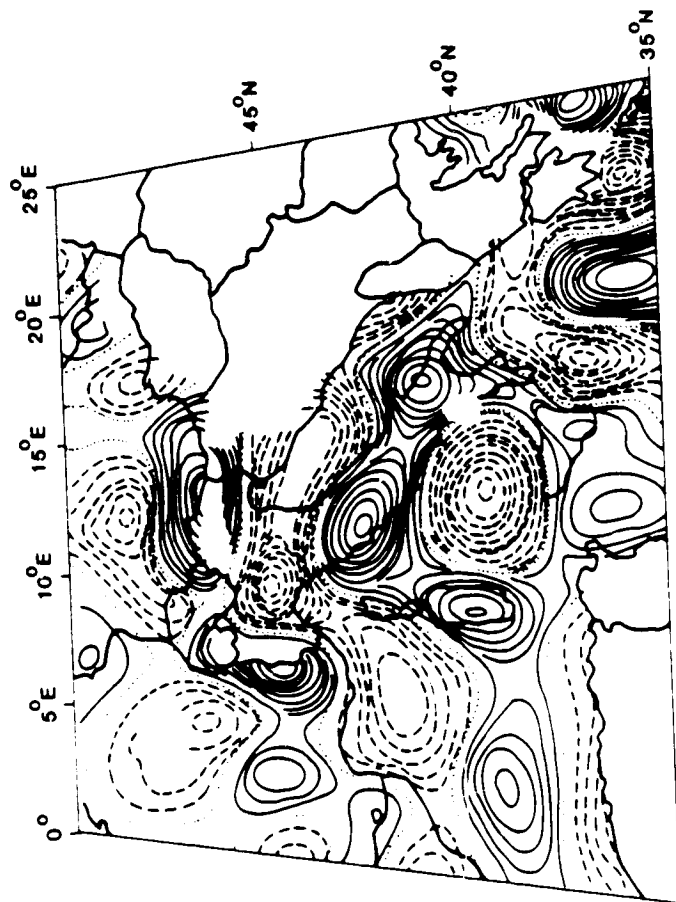
YELLOWSTONE MAGNETICS c.i. = 2 nT
BANDPASS (85 / 100 - 250 / 600) @ 160 Km ALTITUDE

(P. T. Taylor, Written Communication, 1985)

Figure 2-5. Yellowstone, Magnetic

The area occupied by Yellowstone National Park is an unusually active area of recent volcanism and tectonism located near the eastern margin of the North American Cordillera. The famous hot springs and geysers are the expression of a relatively shallow body of rhyolitic magma under a large caldera that may overlie a mantle plume. The caldera is rising at a rate of roughly one centimeter per year and may undergo a renewal of eruptive activity sometime in the future. The area has also experienced seismic activity in recent years, for example, the 1959 Hebgen Lake earthquake.

A prominent elongated free-air gravity positive (>2 m.gals) is situated over the source body for the Yellowstone plume. High temperatures, producing a near-surface Curie isotherm have erased the crustal magnetization thereby producing no magnetic anomaly.

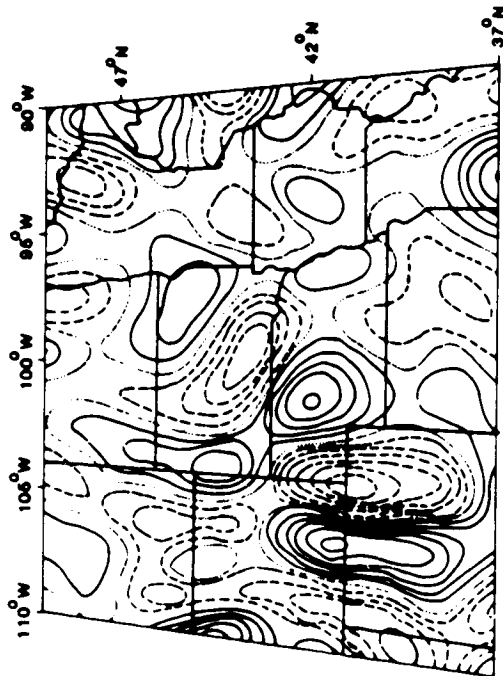


ALPS GRAVITY (FREE-AIR) $ci = 0.5 \text{ mgal}$
 AT ALTITUDE (160 Km) UPWARD CONTINUATION ALPS

(P. T. Taylor, Witten Communication, 1985)

Figure 2-6. Alps, Gravity (Free-air)

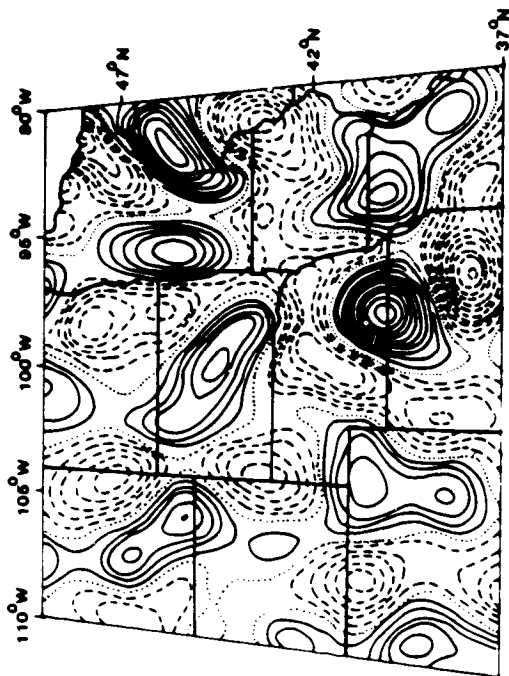
The Alps are the European segment of a much longer Cenozoic orogenic belt extending from Southern Asia (the Himalayas) to Spain (the Pyrenees). They are characterized by thick sequences of largely Mesozoic and Cenozoic sedimentary rock, floored by continental basement, and intense folding and thrusting, chiefly directed in this area to the north and northeast. The Alps are notably non-volcanic, although other parts of the Alpine chain have undergone Cenozoic volcanism. They reveal a positive free-air anomaly of some 5 mgal at GRM altitude.



WILLISTON BASIN GRAVITY c.o = 0.5 mgal
BANDPASS (85 / 100 - 250 / 600) @ 160 Km ALTITUDE

(P. T. Taylor, Written Communication, 1985)

Figure 2-7. Williston Basin, Gravity



WILLISTON BASIN MAGNETICS c.i. = 2 nT
BANDPASS (85 / 100 - 250 / 600) @ 160 Km ALTITUDE

(P. T. Taylor, Written Communication, 1985)

Figure 2-8. Williston Basin, Magnetics

The Williston Basin is a purely tectonic feature, having no topographic expression, occupying the junction of North Dakota, Montana, and Saskatchewan. It has been classified as an autogeosyncline, but the term intracratonic basin is perhaps more descriptive. Having a diameter of about 600 kilometers, it is an isolated sedimentary basin initially formed in the Mississippian, and it is now filled with about 3.5 km of sedimentary rock, some, oil producing.

The structure of the basin is outlined by a magnetic low with a value of less than -10 nT at GRM altitude. This negative magnetic field is characteristic of large sediment filled basins. There is a less well developed free-air gravity low.

In addition to defining the regional context for possible exploration targets, GRM would be of service to mineral exploration by furnishing a base for merging surface magnetic and gravity survey information over large areas. Its global coverage would provide the synoptic patterns to which detailed studies of limited areas could be matched and integrated. This would ease the problem of joining adjacent studies done by different workers on different scales with different datum corrections and assumptions. The GRM would also furnish an objective measure of the regional trends, which must be subtracted from surface surveys to identify target anomalies.

The two data sets of gravitational and magnetic potential, after suitable filtering, are useful for inferring tectonic histories from past epochs, often hundreds of millions of years old. This application is particularly true for magnetic anomalies, since they are not as susceptible to obliteration by isostatic adjustment. Thus, for example, matching of anomalies over different continental areas now separated by young ocean basins (e.g., South America and Africa) can be of use in reconstructing past continental configurations.

The examples presented above are only a few of the continental tectonic problems to which gravity and magnetic data apply. Despite the boon of satellite altimetry over the oceans, the majority of studies have continued to be of continental problems (e.g., as evidenced by papers in journals such as the "Journal of Geophysical Research"). This persistence of interest in the continents is partly because there exists other applicable data (geological, seismological, etc.), but mainly because most of the interesting important problems occur there. The controllers of oceanic tectonics are the subduction zones associated with great compressive belts, such as the Andes and the Himalayas. The variety of tectonic phenomena on the continents is much greater because of the variety of circumstances arising from their four billion year histories. Virtually all economically usable mineral deposits occur in intracontinental and continental margin environments. Because of this abundance of tectonic problems associated with continents, there is a large community of scientists who will welcome the gravimetry and magnetometry which GRM would bring to the poorly surveyed eighty percent of the continents.

GRM satellite-to-satellite range-rate is, at present, the only feasible means of obtaining accurate gravity measurements over a major part of the continents for which data are unavailable, and which include the most important features. The increase in resolution in measurement of the magnetic field over that determined by MAGSAT is significant. Both of these measurements will enable the modelling of crustal and lithospheric structure and their evolution.

2.4 DYNAMICS AND STRUCTURE OF THE SUBOCEANIC CRUST AND LITHOSPHERE

The ocean surface altimetry generated by the GEOS-3 and SEASAT missions has contributed greatly to our understanding of the evolution of the oceanic lithosphere as it moves away from the rises at which it is generated. Altimetry has: (1) clarified flexural and isostatic properties of the oceanic lithosphere as functions of age; (2) shown the existence of mantle flows other than those directly associated with plate motions; and (3) indicated, from geoid anomalies across fracture zones, the differing evolutions of transverse and collinear rheological properties of the lithosphere. It is also being applied successfully to subduction zones in regions of ocean-under-ocean lithosphere subduction, such as the Tonga Trench. As mentioned above, subduction zones are most important, since they probably control the oceanic plate motions. However, the data are incomplete for ocean-under-continent subduction (such as the Andes, or the western ocean-under-marginal-basins subduction, where an extensive island arc has evolved such as the Indonesian Archipelago). Another problem of the oceanic marginal zone which needs better understanding is the development of back-arc basins (such as the Philippine Sea), which in some cases may be developing into oceans themselves.

Magnetic anomalies over the oceanic crust were the key which unlocked the plate tectonic pattern. Sea floor spreading anomalies are of too short wavelengths to be sensed by GRM, but there are longer wavelength anomalies whose sources are still unknown. For example, MAGSAT data show a significant magnetic anomaly associated with the bend in the Hawaiian-Emperor seamount chain, as well as other large anomalies in the western Pacific. But much of the oceanic crust appears to give only small signals at MAGSAT altitudes. GRM would greatly improve the signal-to-noise ratio by measuring closer to the source. The minimum resolution length of 100 km will allow the anomalies produced by linear oceanic features such as aseismic ridges, seamount chains, and submarine plateaus to be seen much more clearly than at the higher altitude of MAGSAT.

GRM's main contribution to understanding oceanic evolution and tectonics will be through its measurement of the gravitational effects at subduction zones, but other problems, such as flexure across seamount chains and magnetic properties of the oceanic crust and upper mantle, can be studied as well

2.5 THE DEEP INTERIOR

2.5.1 THE MANTLE: CONVECTION AND THE GRAVITY FIELD

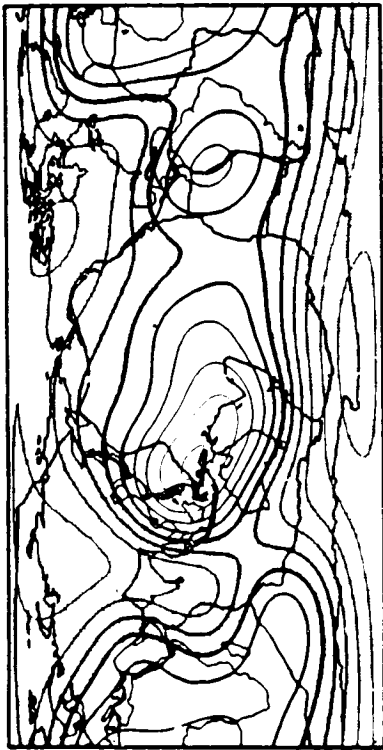
The problem of mantle convection is fundamental to understanding the evolution of the Earth. The outgassing of the oceans and atmosphere, the differentiation of the crust, volcanism, and all tectonics (continental complications as well as oceanic plates) are ultimately dependent on energy sources within (and possibly below) the mantle, and upon the transport of this energy in the mantle by thermal (plus some compositional) buoyancy. The oceanic crust and lithosphere are part of this convection: they are its uppermost boundary layer, coming to the surface at the rises and returning to the interior at subduction zones. Most oceanic crust, as well as its associated lithosphere, must be recycled to the interior. The continental crust and sizeable pieces of subcontinental mantle ride on top of the convective system. The velocities of the system are centimeters per year; the heat delivery is an average of 0.08 watts/meter². These values, together with the thermal and rheological properties of rocks, indicate that the system must be much more complicated than the smoothest flow necessary for observed plate motions. Phenomena such as changes in the plate tectonic pattern every 10-20 million years, long-term episodicity of volcanism in tectonically complex areas such as Western North America, exceptionally high heat flow on the continental side of subduction zones, and higher than predicted heat flow in ocean basins, all suggest that there are secondary scales of mantle flow not directly connected to the precisely measured plate tectonic pattern. What is needed are measurements which see through the lithosphere and into the mantle. The gravitational field is such a measurement. However, gravity in a sense sees too much; it is the integration of attractions throughout the solid earth. Hence it is essential, first, to measure it over as broad a spectrum as possible; and second, to strip off as much as can be properly explained by topography and density variations in the crust and lithosphere.

The gravity field is a direct constraint only on contemporary convection. The problems of greatest concern are mostly dependent on long-term evolution. However, the character of mantle convection has doubtless evolved slowly over the last few billion years. The energy sources are slowly declining by a factor of about fifty percent in the last three billion years. The most crucial question of these last three billion years is: to what extent is mantle convection separated into individual upper and lower mantle systems? This will probably be inferred largely from the effect of this separation on manifestations of contemporary convection, such as the gravitational field.

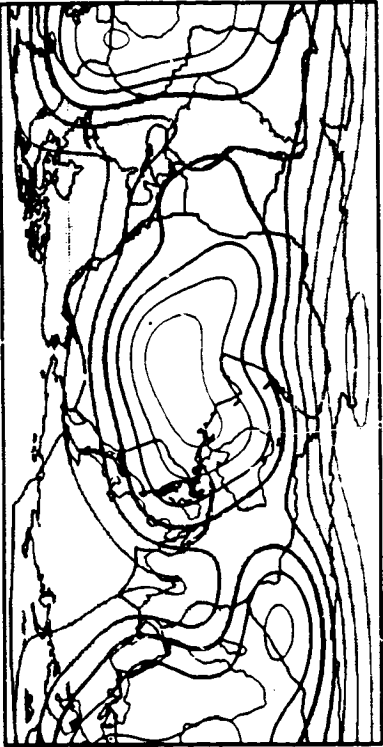
For essentially the foregoing reasons, the SSB 1982 report stated: "Determination of the Earth's gravity field over a wide range of spatial scales is of importance for solid earth dynamics because it is likely to provide direct information of the planform of mantle convection ... An improved gravitational field through space measurement should be an objective of highest priority for the 1980's."

The theoretically predicted complexity of mantle convection, as well as the strong temperature dependence of rock rheology, make it a difficult problem for computational modelling. Progress depends on a rapidly developing dialogue between the fluid dynamicists and those who generate constraints on the models, such as seismologists, isotope geochemists, petrologists, geologists, and others. Theoretical predictions of the gravity signal from forward models have been made since the mid-1960's, but only recently has there occurred a breakthrough in quantitative prediction. Seismological tomography can now infer velocity variations in the lower mantle. If density is assumed to vary with velocity, then a gravity field is calculable. The magnitude of the gravity signal depends on the mantle viscosity, since the magnitude of boundary deformations of the flow produced by the density anomalies depends on the viscosity. Solutions for mantle viscosity increase significantly with depth and account for more than eighty percent of the gravity variations in wavelengths longer than 4000 km (see Figure 2-9).

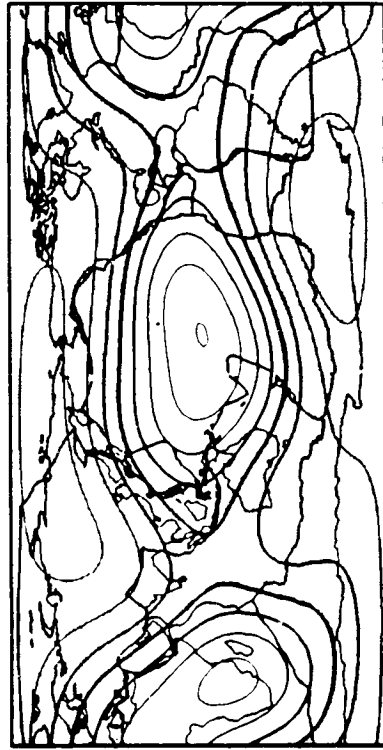
It can be expected that seismological tomography, now in its infancy, will attain much greater detail in mapping the velocity anomalies of the mantle, and that there will develop a stronger need for an improved gravity field in shorter wavelengths to match the predictions. Other rapidly evolving areas are the application of super computers to mantle convective problems and the development of rheological theory for mantle materials.



OBSERVED



OBSERVED MINUS SUBDUCTED SLAB EFFECTS



CALCULATED FROM SEISMIC VELOCITY VARIATIONS

Reprinted from Nature, Vol. 313, No. 6003, pp. 541-545, 14 February 1985
© Macmillan Journals Ltd. 1985

Figure 2-9. GEOIDS from Spherical Harmonic Degrees 2 Through 6

The broad variations of the Earth's gravity field come from a variety of sources. Figure 2-9 demonstrates that the bulk probably comes from two types of sources: (1) density irregularities in the deep mantle, recently inferred by seismology; and (2) subduction zones, where oceanic lithosphere is recycled to the interior.

2.5.2 THE CORE: GENERATION OF THE MAGNETIC FIELD

It is well-known that Earth's magnetic field is not a static entity. The most dramatic, least understood example is the highly irregular, sporadic but sudden reversals of polarity that it undergoes. These transitions are typically spaced a few hundred thousand years apart, but each one is completed in a range of only 2 to 10 thousand years. The rapidity of these changes, compared to geological processes, focuses attention on the Earth's liquid outer core as the seat of the phenomenon and prompts interest in learning how the core fluid moves in order to produce such magnetic spasms.

On a more immediate time scale, at any one place on the Earth's surface, magnetic changes are detectable even within a matter of months. An unpleasant consequence is that surface magnetic charts for navigation have to be updated at least every five to ten years, depending on the accuracy required. Yet, this practical nuisance can, in principle, be converted into a geophysical asset because these short time variations of the magnetic field are also produced by fluid motion in the core. Accurate monitoring of Earth's main magnetic field emanating from the core, together with its secular variation, provides the input for an inverse approach to the problem of determining how the core fluid is moving, a problem not presently approachable by any other means.

There is a variety of reasons for wanting to produce a synoptic map of horizontal fluid motions at the top of the core. The pattern would provide needed insight into the form (and therefore the energetics) of the geodynamo that operates more deeply in the core. Some statements could also be made about the magnitude and pattern of convective heat flux delivered from the core into the base of the mantle. Those same motions move footpoints of magnetic field lines on the core-mantle boundary, so they provide the basis for a short term forecast of the changes in magnetic field seen at the Earth's surface. Finally, it is those motions or probably some variant of them which produce polarity reversals.

The physical idea behind magnetic probing of core fluid dynamics rests on the electromagnetism of Ampere, Faraday, and Ohm: whenever an electrically conducting fluid moves across a pre-existing magnetic field, an electric field arises, which drives current, and whose curl induces the magnetic field to change in time. To determine the fluid motion, it is necessary to record both the magnetic field and its time variation.

How then can the time-dependent magnetic field at the top of Earth's core be monitored? Clearly, global magnetic observations at and above Earth's surface must first be taken and then extrapolated downward through the mantle to the core-mantle boundary. To

a fairly good first approximation, the mantle is electrically insulating, so downward continuation is by way of a magnetic scalar potential function. The real problem is to acquire adequate magnetic data.

Much has been done by looking at records obtained from magnetic observatories, but their small number (less than 200) and very uneven distribution over the surface of the Earth (most are in Europe - the South Pacific, Africa, and a large part of Asia and Antarctica are virtually unsampled) makes it impossible to derive a complete representation of the time-varying field from such data. Spherical harmonic models of the Earth's magnetic potential have often been produced starting with Gauss in 1839. Magnetic observatory data have been supplemented occasionally by repeat stations, surface ship measurements, aeromagnetic data, and satellite data (mainly from the POGO satellites). But the patchy nature of these data, and the fact that the POGO satellites measured only total field magnitude, meant that the measurements of scalar and vector field collected by MAGSAT produced a far better picture of the main magnetic field than had been available prior to 1980.

In order to determine the nature of the time-varying changes of the magnetic field, it is necessary to obtain a second accurate measurement of the field at a later epoch. This measurement is precisely what GRM will achieve. The time span between MAGSAT and GRM (about a decade) is adequate for very significant changes in the various vector components to occur, and yet hopefully, not so long that the core fluid dynamics have changed appreciably.

It was found that over the 7.5 month life span of MAGSAT, many of the spherical harmonic coefficients of the potential required time-varying terms in order to model the observed field accurately. However, that baseline was not long enough to allow these time terms to be measured accurately. Yet a ten year baseline provides time for the large changes needed for accurate measurement. Still longer times may be needed for accurate determination of changes in the higher degree spherical harmonics, but, in any case, those changes may not be coherent. However, an analysis of previous attempts to measure secular variation suggests that it should be possible to determine the secular variation of spherical harmonic components up to degree 12 (wavelength 3300 km) to an accuracy of about 0.1 nT/yr using a ten year baseline. This will be a significant improvement because previous attempts have usually been inaccurate beyond degree 8.

It should also be possible to look at a few of the higher-degree harmonics of the potential to see whether any significant changes have taken place since MAGSAT. It is generally believed (see paragraph 2.3) that harmonics higher than degree 14 represent sources from within the crust. However, if any of these harmonics change with time,

this will be excellent proof that they have sources within the core. Although most of the time varying changes in the higher-degree harmonics will not be capable of being measured, due to the limited time resolution of the method, some of the changes should be larger than average and thus capable of being detected, should they exist. Thus a second very accurate look at the field provided by GRM data will help solve this major problem concerning the source of the intermediate wavelength components of the field.

Longer wavelength variations in the gravity field from GRM measurements will constitute strong constraints on models of mantle convection. The longer wavelengths in the magnetic field observed by GRM, with those from MAGSAT, will produce a very accurate representation of the secular variation, which will constrain models of motion in the fluid core.

2.6 OCEAN CIRCULATION

The SSB study "A Strategy for Earth Science from Space in the 1980s," (1982), states: "The primary scientific objectives for the study of ocean dynamics from space for the next decade, in order of priority are:

1. (a) To measure the time-variable sea-surface elevation;
- (b) To measure the time-independent sea-surface elevation relative to the geoid..."

The sea surface differs from the geoid because of currents, wind stress, salinity, and temperature variations. These departures, called the sea surface topography, occur over a wide range of length scales from 30 km to basin-wide, and over time scales from days to essentially constant. Preliminary estimates of this topography to about 50 cm accuracy have already been made for basin-wide variations using SEASAT altimetry and an independent satellite geoid. The errors of about 50 cm reside mainly in the SEASAT orbit and the geoid, and negligibly in the radar altimetry itself, which probably achieved its design accuracy of 10 cm.

It is desirable to measure the sea-surface topography to 2 cm, the design goal of TOPEX, over as wide a range of length and time scales as possible. Table 2-1 lists the geoid height accuracies achievable for three spatial averaging sizes, while Table 2-2 gives oceanic current scale sizes and estimates of concomitant geoid height accuracies required to determine the currents (TOPEX Working Group, 1981).

Table 2-1
GEOID ACCURACIES

Averaging Size (degrees)	Scale at Equator (km)	Geoid Height Accuracies (cm)
2 x 2	220	2
1 x 1	110	4
0.5 x 0.5	55	16

Table 2-2
Ocean Currents Scale Sizes

Region	Transverse Size (km)	Surface Elevation (cm)	Geoid Requirements Length Scale (km) Height Scale (cm)
Western Boundary Currents	200	150	50 10
Return from Western Boundary Currents	2000	150	50 10
Antarctic Circumpolar Current	1000	100	100 10
Equatorial Currents	1000	35	100 3.5
Basin-Wide Circulation	2000	50	200 5
Pacific-Wide El Nino	5000	100	500 10

It may be seen that current scale sizes of order 100 km (half wavelength) require geoid height estimates of approximately 4 cm. Such a measurement yields a surface geostrophic current error of 4 cm/sec at mid latitudes. It should be noted that geoidal definition to a full wavelength of 200 km implies a horizontal resolution scale of 32 km, which is very close to the internal Rossby radius of deformation of approximately 30 km that characterizes most baroclinic ocean currents. Thus, GRM can provide a geoid whose

definitions on both horizontal and vertical dimensions can in principle allow TOPEX or other altimetric satellites to separate oceanic setup from geoidal undulations down to the smallest scales of interest.

The relationships between GRM and TOPEX are further discussed in Section 2.8. The impact of measurements of both the mean and fluctuating portions of oceanic surface elevations will be to allow greatly improved estimates of global heat transport by the ocean to be obtained; this transport is thought to carry toward the poles of the order of one half (or more) of the excess solar energy deposited in the tropics. This transport is an extremely important mechanism in establishing global climate and its variability. Both the mean current and its fluctuations enter into the transport process, the latter through nonlinear turbulent stresses; and while the energy of the current fluctuations in some parts of the ocean significantly exceeds the mean, the net eddy transport of either fluid or heat by fluctuating currents is estimated to be of the same order as the mean. Thus it is essential to determine both mean and variance if world ocean circulation is to be understood.

The GRM gravity and geoid information are essential for the achievement of the Space Science Board objectives for global sea surface elevations and attendant geostrophic current measurement.

2.7 OTHER APPLICATIONS

2.7.1 AERONOMY

Measurements by the Dynamics Explorer (DE) spacecraft, combined with ground-based observations, are defining the global circulation and structure in the F-region, about 300 km altitude. This circulation is energized by solar EUV at low and midlatitudes, but is strongly controlled by ion drag at high latitudes. Numerical models of magnetospheric convection which predict this behavior at 300 km altitude require arbitrary source parameters, but generally predict much different temperature and circulation patterns in the lower thermosphere, below 200 km altitude. Solar EUV and ion drag are less important at these lower elevations, while other effects, such as dissipation of tides and waves and heating and cooling by nitrogen oxide, are relatively more important. The few measurements which have been made in the lower thermospheric region indicate that enormous shears and extreme velocities at high latitudes can occur, and these have important implications for the global thermospheric circulation and energy budget.

The SSB report, "Solar System Space Physics in the 1980's: A Research Strategy" (Committee on Solar-Terrestrial Relationships, 1980), pointed out the need for a thermospheric dynamics satellite to operate with the incoherent scatter radar chain and the optical Fabry-Perot network to derive the global dynamic properties of the thermosphere. Current investigations should, in the coming decade, improve understanding of the thermosphere as a modulator and redistributor of solar wind energy, mass, and momentum into the Earth's upper atmosphere. However, in situ observations of thermospheric dynamics are badly needed. Measurements of winds and densities at the low-altitude polar orbit of GRM are an exciting opportunity to provide global synoptic maps of the dynamics and structure of a region which is very important, but relatively unprobed.

2.7.2 EXTERNAL MAGNETIC FIELD

The external magnetic field of the Earth arises from a complex system of electric currents flowing in the magnetosphere and ionosphere. Of particular interest are the currents which flow along magnetic field lines into and out of the polar regions. A vector magnetometer on a low-altitude spacecraft, such as GRM, would make it possible to study the directions and intensities of these currents, and their spatial and temporal variations. At a higher altitude, MAGSAT was the first satellite to measure these currents with a nearly absolute standard. This permitted study of the relationship between field-aligned currents and auroral electrojet currents.

Magnetic observations by GRM at 160 kilometers altitude would provide higher-resolution studies of the auroral electrojets, because they would be the closest observations to these currents ever made.

Studies of the external magnetic field are important to study of the Earth's interior in two ways. First, the study of the internally generated field depends on correct removal of the external field. At present, data taken during periods of external field disturbance are often useless for the study of the internal field generation. Second, temporal changes in the external field enable estimates to be made of the electrical conductivity of the solid Earth, because they induce currents. The magnetic field produced by these induced currents should be strong enough at GRM altitudes to enable determination of regional variations in the electrical conductivity of the Earth. These variations in conductivity in turn indicate variations in temperature or composition.

2.7.3 ORBIT COMPUTATIONS AND GEODESY

These problems were addressed in the NRC study "Applications of a Dedicated Gravitational Satellite Mission" (Panel on Gravity Field and Sea Level, Committee on Geodesy, 1979). At that time, the critical needs were of two distinct types: (1) altimetric satellites such as GEOS-3 and SEASAT-1, and (2) positioning satellites such as LAGEOS, STARLETTE, and GPS. Both of these needs persist. In regard to satellite type (1), the requirement is more severe than ever, if TOPEX is to be implemented, since the altimetric accuracy contemplated (4 cm) is about what is estimated for one-degree mean geoid heights from satellite-to-satellite range-rate by the GRAVSAT Users Working Group in its report of August 1980.

Geodesy requires precise orbits, as discussed in the preceding paragraph. An independent desideratum is the attainment of a global datum for height measurements. Vertical locations within geodetic systems should be referred not to a reference ellipsoid or the Earth's center, but rather to an equipotential surface. Normally this specific equipotential surface is estimated from tide measurements. However, the mean sea level differs from an equipotential level by tens of centimeters, while for remote areas where control for mapping is by photogrammetry, the averaging out of tidal oscillations may not be feasible. Satellite positions and geoid heights accurate to centimeters could unify vertical datums, and establish them in remote areas. The determination of an accurate geoid from GRM data will be important to fully utilizing the GPS to determine locations, since heights above the geoid are wanted.

GRM will provide significant information to aeronomers, complementary to that from the Dynamics Explorer, because of its low altitude. External magnetic fields will be better defined, and useful information about Earth conductivity will be obtained from the time-varying induced currents. The accurate gravity field generated by GRM will lead to more accurate satellite orbits and a more precise geoid, of value to geodesy as well as to oceanography.

2.8 COORDINATION OF GRM WITH OTHER MISSIONS AND STUDIES

MAGSAT, launched in 1979, produced the best picture of the Earth's magnetic field yet obtained. In order to make use of these data, it is essential that the time variations of the field are measured. GRM will provide another very accurate picture of the field which will help in this process of describing the time variations. If the GRM is launched prior to a proposed Magnetic Field Explorer Mission (MFE), which is a longer duration 550 km altitude core field monitoring mission, the GRM will provide the needed tie between the earlier MAGSAT results and the later long-duration MFE mission. This

will produce an unparalleled data set for studying the core of the Earth. If, on the other hand, MFE is launched prior to GRM and they are simultaneously operational, then there will be some advantage in having observations at different altitudes (160 km and 550 km) in order to remove the external field of the Earth. The magnetic observations of GRM and MFE are complementary. GRM will give a much better representation of the crustal component of the magnetic field, whereas MFE will allow the temporal variations of the core field to be accurately measured.

The indirect nature of inferences from the gravity and magnetic fields makes it essential that they be used in conjunction with other data. By far the most important data type is topography: (1) the elevations, to calculate the attracting effect of the topography; and (2) imagery, to provide the visible context of the gravimetry and magnetometry. The elevations required must be accurate to a few meters for area means comparable to the resolution of the gravimetry. In many areas of interest, such as the Soviet and Indian parts of the Alpine Belt, this accuracy can be satisfied by existing maps. In others the requirement can be met by systems of moderate accuracy, such as the GEOS-3 and GEOSAT altimeters, or the Large Format Camera (LFC). The imagery of relatively undeveloped areas, which is the foremost application of GRM, is best obtained by radar systems, since many of these are covered by vegetation (e.g., the Amazon Basin). Furthermore, in areas not so covered, it is desirable to infer subsurface features, such as the relics of valleys in the eastern Sahara found by SIR-A. The obvious tool is Shuttle Imaging Radar (SIR). SIR and GRM will make a natural couple, and the two data types in combination should constitute a significant advance in comprehensive examination of major tectonic areas such as the Hindu Kush, Pamir, Himalaya, and Tibetan Plateau Complex or the Andean chain, which are so important to the global tectonic picture but so inaccessible to ordinary means of survey.

While existing data plus LFC, SIR, etc., will complement the highest-priority objectives of GRM, the dynamics and structure of the continents and the study of the suboceanic crust and lithosphere will continue to be limited by the sparseness of bathymetry in many areas. This situation will improve with time. However, the strongest driver for this application of GRM is to complete the data for land-covered parts of subduction zones.

For the deep application of GRM described in paragraph 2.5 (Mantle Convection and Core Geodynamics), pacers are the development of theoretical insight, computational models, global surveys by seismic arrays, and laboratory measurement of rock properties (see Research Briefings, 1983). As discussed above, mantle convection modelling needs detailed gravitational fields while hydromagnetic theorists are already anxious for

better data on secular change in the magnetic field, for which a GRM nine years after MAGSAT would be ideal.

The application of GRM data to ocean circulation depends, of course, on an accurate altimetric satellite, for which role TOPEX is proposed. Objective 1(a) of paragraph 2.6, the time-varying field, can be partially achieved to an estimated accuracy of 14 cm using precisely repeating tracks of the TOPEX orbit in an inclination designed to avoid tidal effects. At present, a repetition interval of ten days and an inclination of 64 degrees are planned. The 14 cm error arises almost entirely from the radial component of the satellite position. This estimate assumes intensive tracking by the TRANET Doppler network and orbit computation using the best available gravity data (JPL Study Team, 1982). However, the balance of objective 1(a) and objective 1(b), the time-invariant field, cannot be attained to better than the existing 50 cm accuracy without a greatly improved gravity field, which GRM would provide. This gravity field would contribute in at least two ways: (1) by furnishing a more accurate geoid; and (2) by enabling computation of more precise orbits for TOPEX (TOPEX Science Working Group, 1981). Other ways in which GRM may contribute to the TOPEX mission are: (3) by enabling more effective deployment of surface ship measurements complementary to the TOPEX altimetry; and (4) by freeing TOPEX from restriction to the precisely repeating ground track. Improvement (3) would come through use of the GRM gravity field for the orbit and geoid with SEASAT altimetry, furnishing sea surface topography good to about 10 cm, which would enable more careful planning of the surface ship placement. Contributions (1), the geoid, and (2), the orbit, could eventually be realized by launching GRM subsequent to TOPEX. The improved orbit accuracy, (2), could be partially achieved through use of the GPS. However, contribution (3), ship deployment planning, could not be attained without GRM prior to TOPEX, while contribution (4) with TOPEX prior to GRM would require an assurance difficult to imagine.

As discussed in paragraph 2.7.2, the low altitude of GRM would make it of great benefit to aeronomy, providing measurements complementary to those of the Dynamic Explorer spacecraft at 300 km, and greatly assisting an ongoing theoretical and observational effort in upper atmosphere circulation.

A final virtue of GRM which should be mentioned is that, to the knowledge of this Working Group, it is unique: no other satellite-to-satellite range-rate system is under consideration, either in the Department of Defense or overseas. For the gravitational part of the mission, the principal system under development is the cryogenic gravity gradiometer. However, the gradiometer is still at an early stage of laboratory development. It is not known whether certain fundamental difficulties

will be overcome, and, at best, the gradiometer would not be ready for space flight until well into the 1990's.

2.9 CONCLUDING REMARKS

GRM will be capable of measuring the gravity and magnetic field of the Earth from the longest wavelengths down to a half wavelength of about 100 km. GRM's sensitivity to an extended spectrum should enable a large variety of lithospheric problems to be studied. The gravity and magnetic response of mountain ranges, sedimentary basins, rifts, and other structures will be measured. These measurements can then be used to model these features and constrain their tectonic history.

The longer wavelengths of the gravity field will be valuable for modelling the convection which occurs within the mantle. The long-wavelength spectrum of the magnetic field will allow an accurate model of the core field to be produced. Comparison of this model with that produced by MAGSAT nine years earlier will give the best information ever available on the secular variation of the magnetic field.

The gravity data over the oceans will provide a gravitational geoid, to which sea surface heights measured by TOPEX can be referred. These heights will give information on the time-independent oceanic circulation. The pattern of external magnetic fields and information on the circulation pattern in the lower thermosphere will also be measured by GRM. The more accurate measurement of the gravity field by GRM will enable significantly more accurate calculations of orbit parameters of other satellites, including TOPEX. A launch of GRM in the early 1990s would be long enough after MAGSAT to allow very accurate measurements of the secular variation of the Earth's magnetic field to be made. There also are a number of other developments in the various fields of geophysics relevant to the GRM which argue for an early launch as outlined in paragraph 2.8 of this report.

SECTION 3. SPACEFLIGHT MISSION DESCRIPTION

3.1 SCIENTIFIC REQUIREMENTS

3.1.1 GRAVITY

The Committee on Geodesy of the National Research Council (NRC) in the 1979 Report concluded that the existing knowledge of the Earth's gravity field is not adequate for various disciplinary needs. The required 1 sigma (1σ) accuracies and resolutions indicated for the GRM are as follows:

- Gravity anomaly accuracy 2.5 mgal
- Horizontal resolution 100 km
- Accuracy of oceanic geoid undulation difference 10 cm (over wavelengths of 100 to 300 km)

These accuracies will meet the disciplinary requirements listed in Table 1-1 and described in Section 2. The accuracy and resolution requirements determine the 160 km orbital altitude of the two GRM spacecraft. The global coverage requires that the orbital inclination be polar or near polar. Based on error analysis studies of the mission, approximately eight northbound and southbound passes of the satellites dispersed over each 1-degree equatorial increment are required. Such a coverage establishes a minimum mission lifetime of 6 months.

3.1.2 MAGNETIC

Magnetic mission requirements are based on the previously discussed mission objectives. The lowest possible altitude is necessary for increased anomaly signal and resolution, and a minimum satellite lifetime of 90 days is necessary for obtaining adequate data distribution. Based on these requirements, lowest possible altitude versus mission life, an operational altitude of 160 km was established. Using the data obtained from the Polar Orbiting Geophysical Observatory (POGO) and Magsat, the anomaly amplitudes up to 100 nT at 160 km determine the mission accuracy requirements. Absolute scalar accuracy of 2 nT is expected to be sufficient for detecting all major crustal features.

Noise from ionospheric and magnetospheric sources limits the achievable accuracy to about 2 nT. The accuracy along the orbital track is only limited by the instrument performance of 1 nT. It is estimated that a vector accuracy of better than 5 nT and 20 arc-seconds will be required in the anomaly studies.

The accuracy requirement for the field model is determined primarily by the need to remove the core source contributions from magnetic survey data. For an accuracy of 10 to 20 nT at the Earth's surface (assuming that the noncrustal fields can be represented by a 13th degree spherical harmonic expansion), an accuracy of about 5 nT at a 200 km altitude is required.

Table 3-1 summarizes the mission accuracy requirements in terms of the expected mission applications.

Table 3-1
Magnetic Accuracy Requirements (RMS)

Application	Scalar	Vector Component
Crustal Anomaly Studies	2 nT	5 nT, 20 arc-sec
Upper Mantle Conductivity	--	5 nT, 20 arc-sec
World Magnetic Charts	2 nT	15 nT, 60 arc-sec
Ionospheric/Magnetospheric Research	--	50 nT, 200 arc-sec

The major contributions to measurement error are the accuracy of determining spacecraft position and the precision to which the attitude of the vector sensor is known. To achieve the 5 nT accuracy, the attitude at the sensor must be determined to within 20 arc-seconds, and the spacecraft position to within 60 meters, 3 σ , radially and 100 meters, 3 σ , horizontally.

The Earth's magnetic field measurements are made in the presence of perturbing magnetic fields from ionospheric and magnetospheric sources. If the mission is flown during solar maximum, approximately 50 percent of the data obtained at latitudes below 50 degrees will be sufficiently free of these perturbations to yield the required accuracy. Above 50 degrees latitude, sparser data would be adequate. For global anomaly resolution of 100 km, coverage is needed along grid lines no more than 50 km apart. The time needed for achieving this resolution is estimated to be 30 days for perfectly quiet data or 90 days at solar maximum. This is a minimal coverage with no capability of averaging or statistical analysis. In order to provide a workable sample, data twice this density are required. This sets the desired lifetime of the mission at 180 days.

3.2 MISSION DESCRIPTION

The gravity measurement requirements can be met through the analysis of the relative orbital motion between two drag-free objects. The objects are spheres located in cavities within two spacecraft following the same circular polar orbit at an altitude of 160 km. The two spacecraft will vary in separation from 150 to 550 km in accordance with a mission flight plan. Millimeter wave antennas on each spacecraft will point to corresponding antennas on the other spacecraft. Each spacecraft will transmit and receive simultaneously in the 42 and 91 GHz Continuous Wave (CW) bands. Frequency shifts caused by small changes in the velocity between each spacecraft will be measured. As the spacecraft are affected by drag forces, the spacecraft are thrust periodically to prevent the spheres from touching the cavities. Since the spacecraft-cavity configuration shields the spheres from all surface forces, the motion of the spheres is affected only by body forces. The cavities are located at the exact centroid of each spacecraft so that the only differential body force acting on the spheres is gravity. Relative motion between the two spheres as they are accelerated and decelerated while passing over a gravity anomaly is a measure of the anomaly magnitude. The position of the sphere within each spacecraft and the relative motion between the two spacecraft are measured to the 1×10^{-6} m/s level every 4 seconds in the along-track direction providing data every 30 km along the meridian. Over the mission lifetime of 6 months, ground-track repeat cycles of 30, 60, 90, or 180 days may be selected to provide both the required spatial separation at the equator and to optimize the computational processing (discussed in paragraphs 4.3 and 6.7).

The magnetic measurement requirements can be met using the vector and scalar magnetometers similar to those of the Magsat mission. In addition to the magnetometers, the

magnetic measuring spacecraft will carry a set of four star cameras and two sun sensors that will provide the navigational references required for mapping the magnetic field.

During the mission, the science data will be continuously collected, stored, and transmitted to the ground operations control center. The data related to the gravity field will be extensively processed to determine the field to within 2.5 milligal and the geoid amplitude to within 10 cm; both the field and the amplitude will have a 100 km half-wavelength resolution. The interim-less-accurate results will be available within one year of the flight termination, and the processed raw SST and DMA Doppler data tapes will be available within 3 months after the start of the science mission. The final precision high-resolution gravity field data and the spherical harmonic model will be available within 2 years after flight termination. The magnetic field data will also be available on an interim, less accurate basis within 3 months after the start of the science mission. The final, 20 arc-second resolution vector aspect angle tapes will be available within 1 year after mission termination.

3.3 ORBIT SELECTION

3.3.1 GRAVITY MISSION

The goal of the gravity mission is to provide the \dot{s} (Figure 3-1) measurement on a global scale that correlates to a 1 mgal anomaly of a 100 by 100 km (more precisely, a 111 by 111 km) square. The magnitude of the \dot{s} in $\mu\text{m/s}$ for such a gravity anomaly is shown in Figure 3-2. The peak-to-peak signal of 20 $\mu\text{m/s}$ is for a zenith pass at an altitude of 160 km. While coplanar orbits have been selected as the prime configuration, other investigators suggest that identical ground track orbits are preferable.

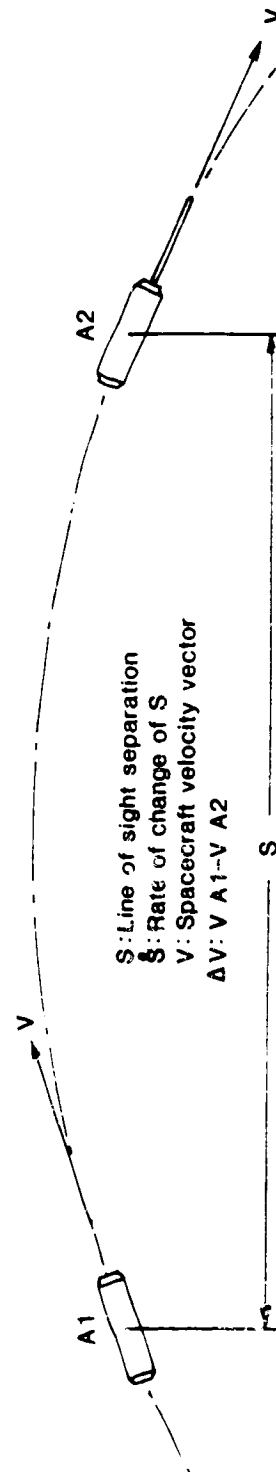


Figure 3-1. Definition of \dot{s}

1 deg. x 1 deg.; -1 mgal

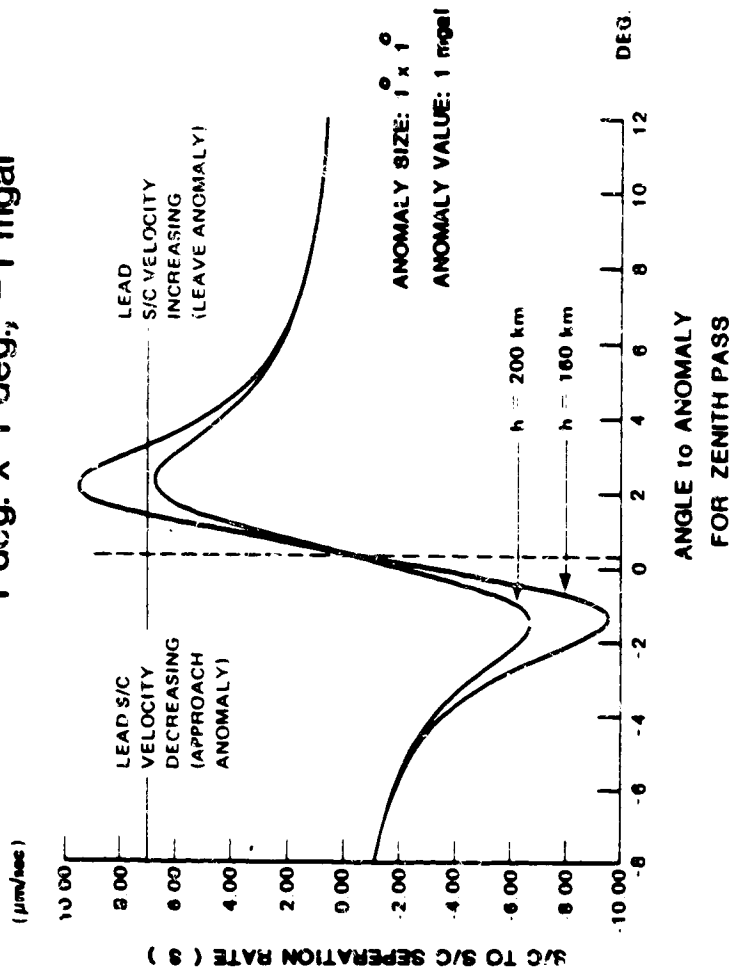


Figure 3-2. Gravity Anomaly Sensing at Two Altitudes

To obtain the required global coverage, the orbit must be polar (inclination = $90^\circ \pm 0.1^\circ$). The duration of the mission is based on the allowed spacing between ground tracks. Sampling theory dictates that to prevent aliasing, the rate should be twice the signal rate. Thus, the equatorial spacing should be no greater than 0.5 degree. The flight duration of 180 days allows the right ascension equatorial spacing to be 0.0625 degree or 8 times the minimum sampling rate. The equatorial separation may be based upon shorter ground-track repeat cycles resulting in spacing greater than 0.0625 degree, but not greater than 0.25 degree.

Figure 3-3 shows the residual signal of GRM for the spherical harmonic expansion beyond degree L. Therefore, it corresponds to the minimum degree of the harmonic expansion that is required to meet a specified accuracy of the \dot{s} signal.

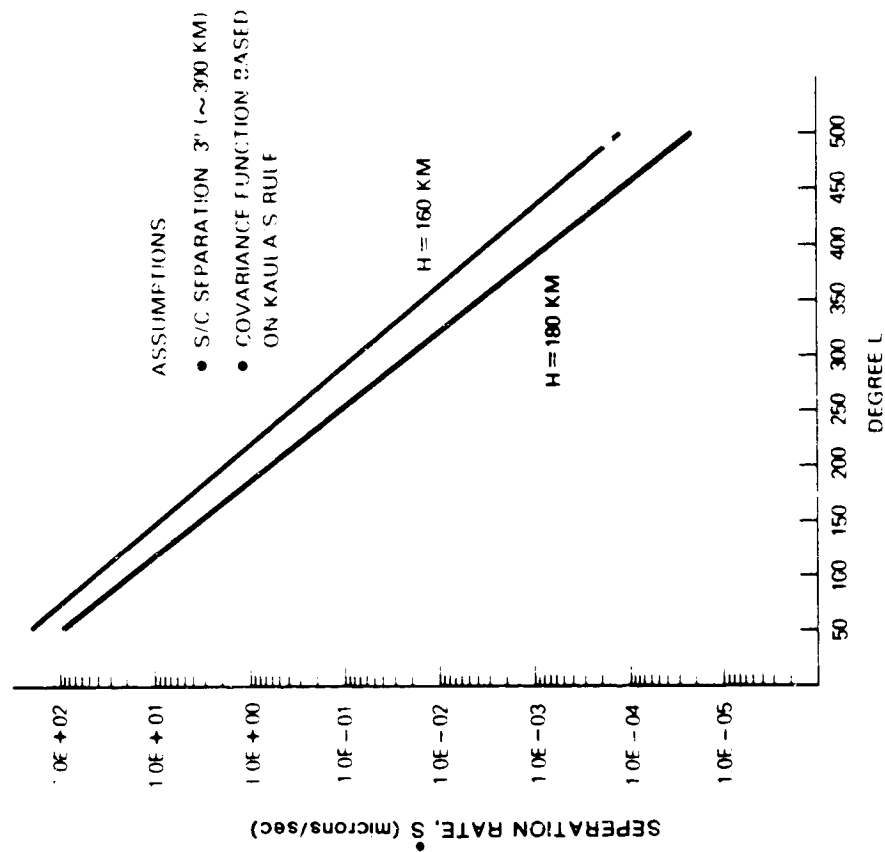


Figure 3-3. Truncation Effect of GRM \dot{s} Value Beyond Degree L

For an expansion carried out to degree 180 at 160 km (resolution of 1 deg x 1 deg square), Figure 3-3 shows that it would correspond to \dot{s} accuracy of 2 $\mu\text{m/s}$. Because of the aliasing effect due to truncation, further simulations and analysis have shown that the expansion should be modeled to about degree 300 for an \dot{s} accuracy of 1 $\mu\text{m/s}$.

The science requirements of 2.5 mgal, 1-degree square, and 10 cm geoid determine the mission performance requirements, which are:

- \dot{s} * Noise: 1.0 $\mu\text{m/s}$ (1σ)
- Orbital Altitude: 160 km (at Equator)
- Orbital Inclination: 90 \pm 0.1 deg
- Mission Lifetime: 180 days

3.3.2 MAGNETIC MISSION

The GRM design orbit meets the needs of low altitude and global coverage. In addition, the GRM drag-free, circular orbit provides an inherent advantage and is superior to the Magsat orbit. Figure 3-4 shows that the estimated sensitivity and resolution for the GRM exceeds all previous missions. Resolution of the crustal anomalies is directly dependent upon the satellite altitude as shown in Figure 3-5.

*The \dot{s} measurement noise is the 1 sigma total of the uncertainty contributions from all hardware, software, and natural phenomena such as ionosphere.

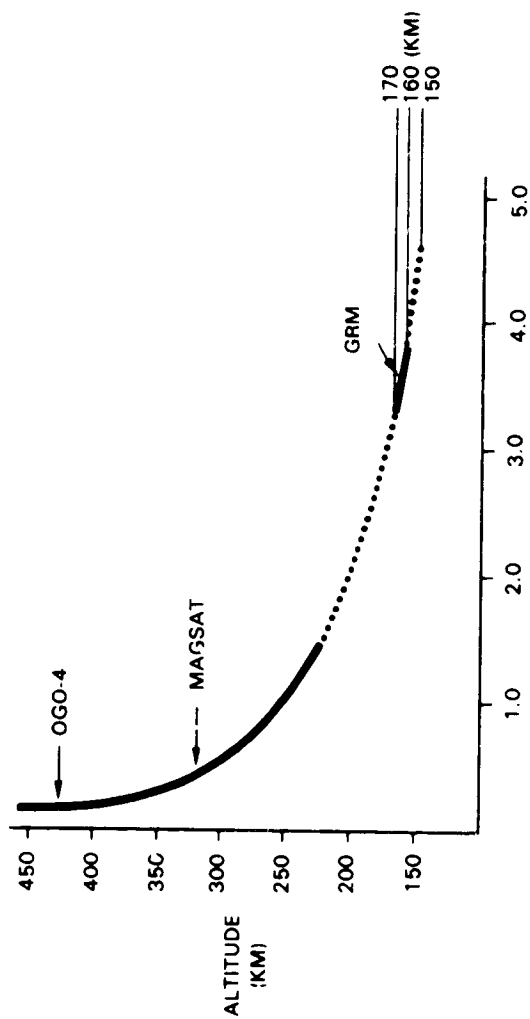


Figure 3-4. Relative Magnetic Anomaly Amplitude as Observed at Spacecraft

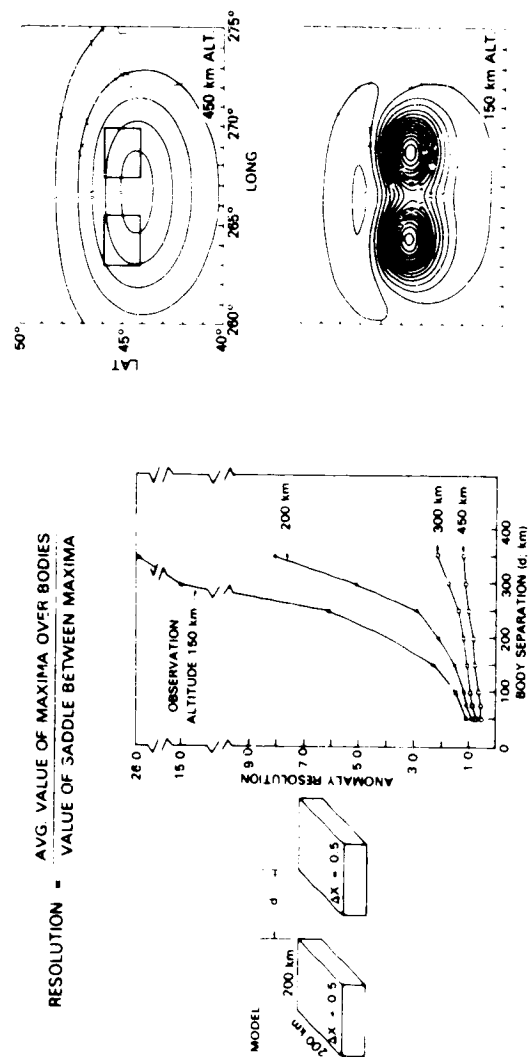


Figure 3-5. Resolution of Magnetic Anomaly as a Function of Altitude

3.4 TRACKING COVERAGE AND ACCURACY

3.4.1 DOPPLER TRACKING NETWORK

The required orbit determination, 3σ accuracy for the magnetic mission is:

- 60 meters radial
- 100 meters along- and cross-track

The required accuracy for the gravity mission is:

- 100 meters radial
- 300 meters along- and cross-track

These accuracies are readily obtainable from the Defense Mapping Agency (DMA) Doppler tracking network. The Doppler network can measure the spacecraft position to within 2 meters. The network (Figure 3-6) provides an orbital position at 39 locations. Ephemeris data will be generated by NASA from the Doppler data obtained from the DMA.

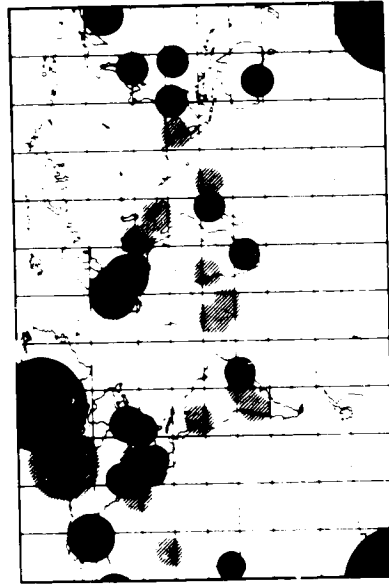


Figure 3-6. DMA Network of Doppler Tracking Stations
(Antarctic Polar Station not Shown, Solid Discs Denote TRANET)

Because of delays in approval of the mission, the full DMA network may not be available as shown. It is expected that the 20 TRANET stations will be available and sufficient to support the mission. However, there is a need to evaluate using the Global Positioning System (GPS) for the operational tracking network.

3.4.2 TRACKING DATA RELAY SATELLITE SYSTEM

The NASA Tracking Data Relay Satellite System (TDRSS) tracking of the GRM will be required for GRM mission support. Ephemeris data generated by the TDRSS tracking of the GRM are not sufficiently accurate for the scientific data reduction. TDRSS tracking will be used extensively during the early part of the mission for quick-look orbit determination while the spacecraft are descending from (STS) insertion altitude to the mission altitude. TDRSS has global coverage capability except for the Zone of Exclusion (ZOE) as shown in Figure 3-7. Onboard tape recorders will be utilized to store data during the ZOE period.

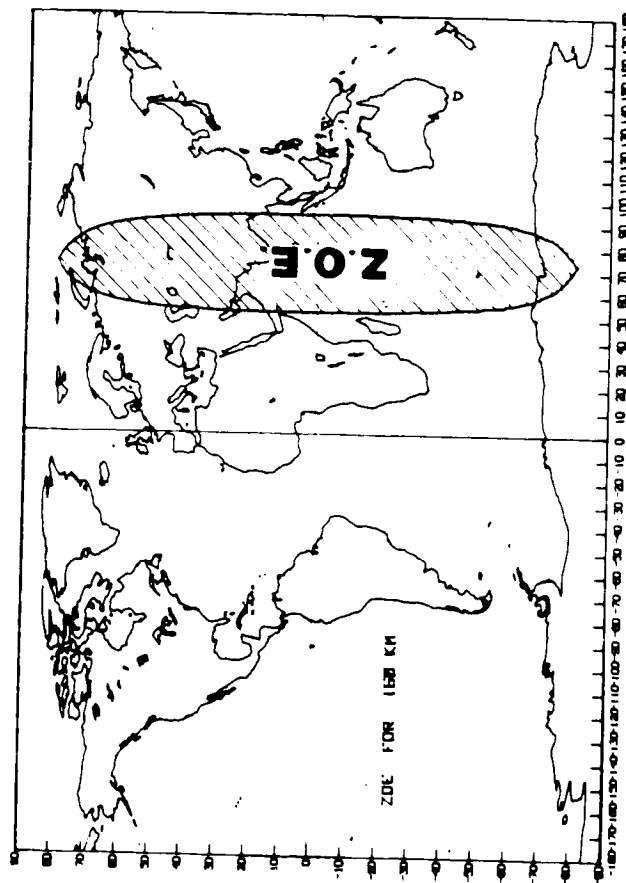


Figure 3-7. TDRSS Zone of Exclusion

3.5 DOPPLER NETWORK DATA COLLECTION

The planned utilization of the Doppler network operated by the DMA (Figures 3-6 and 3-8) is ideally suited for the GRM flight.

The combined features of the low orbital altitude (160 km) and drag-free orbit and the performance capability of the network will result in Doppler data well within the minimum needs required for the spacecraft orbital position determination. The DMA operated Doppler network will not provide ephemeris data. Instead, these Doppler data obtained from the stations will be cleaned, checked, and delivered to NASA.

The difference between the TRANET stations and the GEOCEIVER stations (Figure 3-6) is that the former have the capability to simultaneously track two spacecraft, whereas the latter have the capability to track only a single spacecraft. The two spacecraft tracking is obtained using +77.5 and +82.5 parts per million offsets from the 150 and 400 MHz carrier frequencies.

Figure 3-8 shows the TRANET coverage obtained for 25 GRM orbits. Individual station coverage is based on elevation angles above 5 degrees. Each dashed segment is a 30-second pass and five segments are required for valid data.

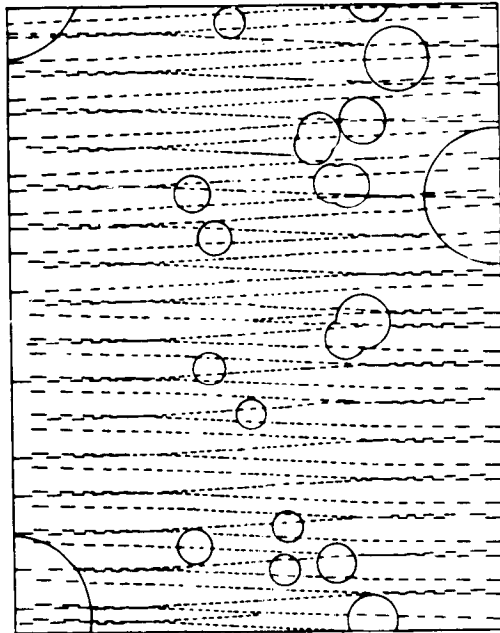


Figure 3.8. GRM TRANET Doppler Network Coverage (5 deg Elevation)

3.6 LAUNCH AND DESCENT PHASE

One Shuttle will be utilized to launch both GRM spacecraft from the Western Space and Missile Center (WSMC) into a polar orbit.

Deployment (Figure 3-9) will be at a nominal altitude of 275 km. The Orbiter will place the two spacecraft in the same orbital plane, positioning the A-2 spacecraft 50 km behind the A-1 spacecraft.

A deploy/descent sequence giving the procedure for descent to 160 km altitude and a range separation of 150 km is as follows:

<u>Step</u>	<u>Operation</u>
1	STS deploys A-1 at 275 km
2	STS deploys A-2 at 275 km with 50 km separation
3	24 hours of spacecraft/mission checkout
4	Both spacecraft descend to 225 km (Hohmann Transfer)
5	A-2 spacecraft separates to 100 km at 225 km
6	48 hours of spacecraft/mission checkout
7	Both spacecraft descend to 200 km (Hohmann Transfer)
8	A-2 spacecraft separates to 150 km at 200 km
9	72 hours of spacecraft/mission checkout
10	Both spacecraft descend to 180 km (Hohmann Transfer)
11	96 hours of spacecraft/mission checkout at 180 km
12	Both spacecraft descend to 160 km (Hohmann Transfer)
13	168 hours of final spacecraft/mission checkout
14	Begin mission operations

The accumulated time of flight for this sequence is 417 hours; the accumulated fuel consumption is 142 kg for the A-1 spacecraft and 150 kg for the A-2 spacecraft.

The foregoing sequence has been established to provide a framework for mission planning. The monitoring of both spacecraft will only be interrupted by the ZOE related to the TDRSS coverage. Extensive use of the one-way Multiple Access (MA) Mode 2 of Data Group 1 (DG 1) is planned to provide both a Doppler link to the TDRS for orbit determination and a telemetry link. DG 1 Mode 2 uses a noncoherent carrier (a forward link is not required) with two short Pseudo Random Noise (PRN) codes utilizing Binary Phase-Shift Key (BPSK) modulating the quadrature phases of the carrier. During the deploy/descent phase, the science data transmission from the A-1 spacecraft may be restricted when the MA Mode 2 DG 1 is used.

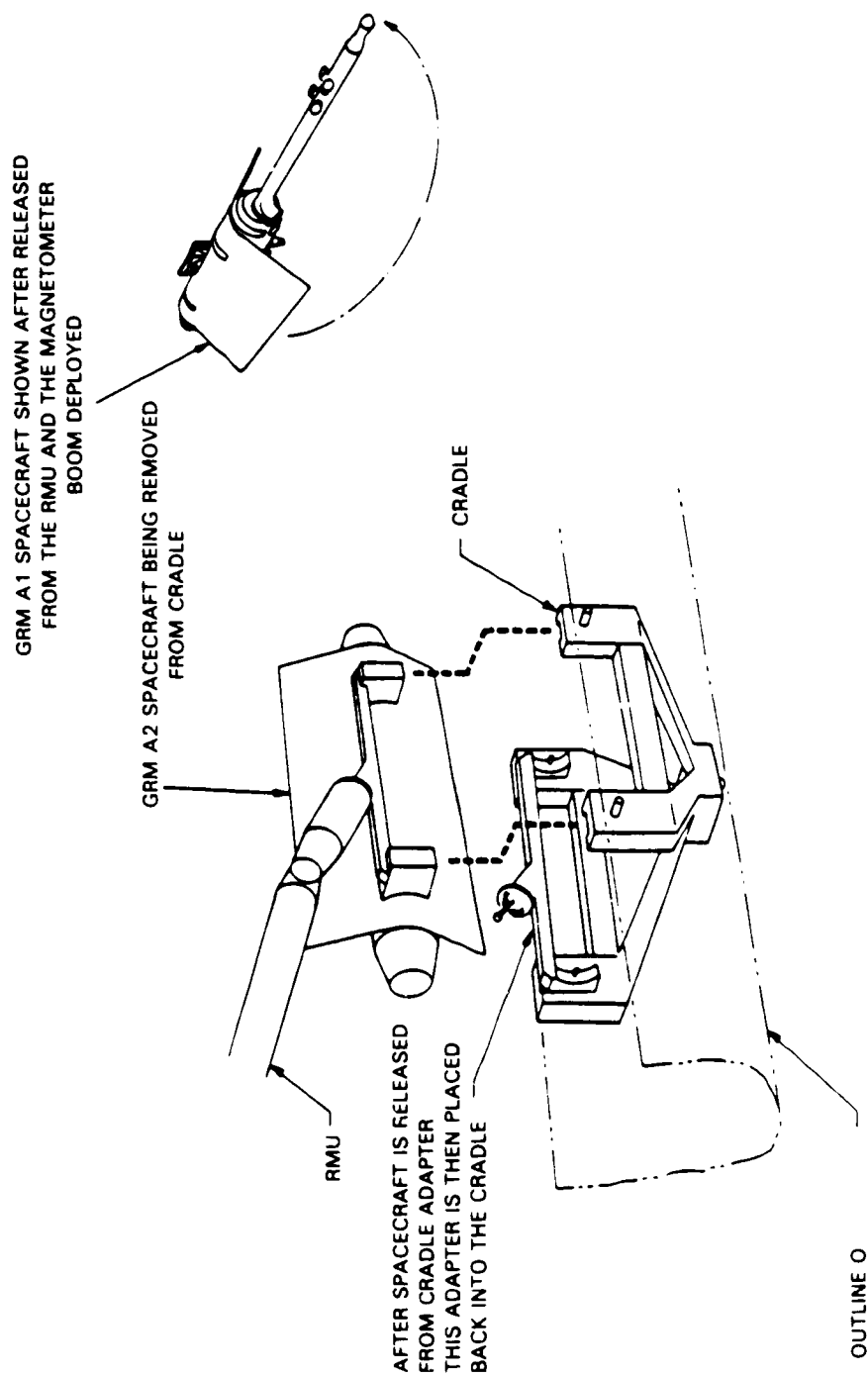


Figure 3-9. GRM Deployment

4.1 DATA FLOW SYSTEM

The GRM Data Flow System is shown in Figure 4-1. The two spacecraft (A-1 and A-2) are linked to each other via the SST, and each spacecraft is linked to the ground via the TDRSS. The TDRSS will provide a nearly global coverage of the A-1 and A-2 spacecraft. The command, spacecraft and experiment telemetry, and TDRSS ranging signals will be linked to GSFC by the White Sands Ground Terminal (WSGT) and a Domestic Satellite (DOMSAT) relay network. Control of the GRM spacecraft will be from a Multisatellite Operations Control Center (MSOCC) located at GSFC.

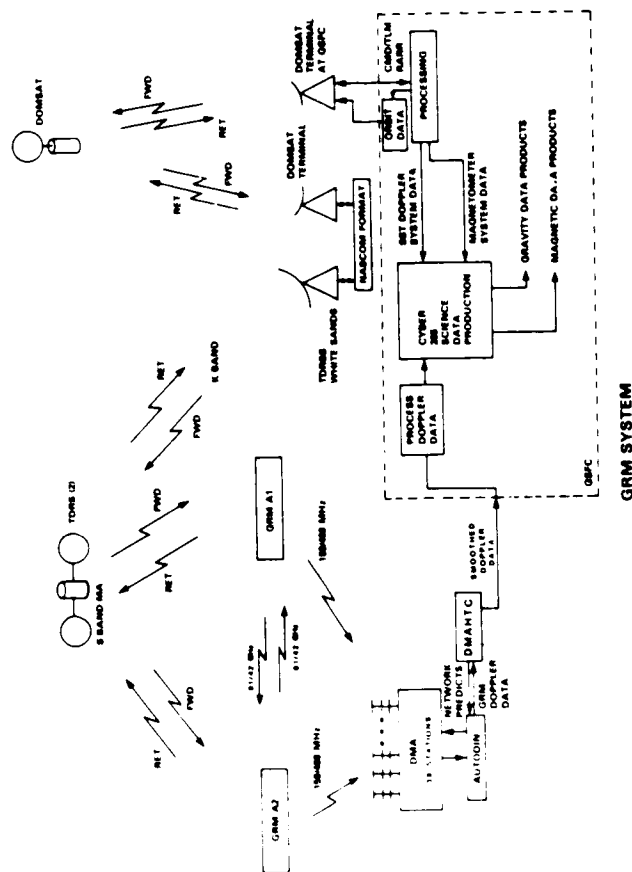


Figure 4-1. GRM Data Flow System

Determination of the operational orbits of the A-1 and A-2 spacecraft will be accomplished using the TDRSS ranging system and the onboard transponders that is required for TDRSS-to-GRM operational control and the command/telemetry link. The telemetry link will include the Satellite-to-Satellite Tracking (SST) Doppler system data.

The GRM orbital position determination will be obtained using the DMA network Doppler tracking stations. If the Geceiver stations are not in operation, only the 20 TRANET stations will provide the tracking data. In either case, the stations operating at the frequencies of 150 and 400 MHz are linked to the DMA Hydrographic/Topographic Center (DMAHTC) via the Department of Defense (DOD) Autodin Network. The spacecraft-to-ground Doppler data for orbit determination will be smoothed, quality-checked, and time-tagged before transmission to GSFC. GSFC will compute the orbits and use the computations as the basis for the magnetic science data and as the initial estimated orbit for the gravity science data. The final orbit will be determined in an interactive sequence, as the gravity field model is refined.

The three-axis vector data obtained from the vector magnetometer must be inertial-space oriented. This orientation is obtained by using the computed orbit and the pointing angles provided by the star camera. The maximum aspect angle error of any one axis is 20 arc-seconds.

4.2 FLIGHT DATA

4.2.1 RANGE RATE (\dot{s}) DETERMINATION

This parameter, which is the basis for computing the gravity anomalies, is measured using the SST system and the Disturbance Compensation System (DISCOS). To obtain the SST data, a pair of millimeter wave (42 and 91 GHz) signals are obtained from a highly stable 5 MHz oscillator. These two signals are transmitted between the two satellites. If the line-of-sight distance between the satellites varies, the two wave signals are frequency-shifted by the Doppler effect. The phase of the frequency shifted signal is compared with that of the stable 5 MHz reference signal. This frequency difference is measured by a time-interval counting method at a rate of nominally 10,000 samples per second. Both the 42 and 91 GHz Doppler-shifted signals are averaged over 0.1 second. Each satellite is simultaneously measuring the same \dot{s} . By combining the data in ground processing, coherent errors are canceled.

The ground data processing for the \dot{s} determination is summarized as follows:

- The three axis proof-mass position within each spacecraft is measured 10 times per second and it is used for correcting the SST data.
- \dot{s} time averaged over 4 seconds for two frequencies from each spacecraft is determined.
- The orbital position of each spacecraft determined from the Doppler tracking by the DMA network is used for position determination to within 100 meters radial and 300 meters along- and cross-track.

4.2.2 MAGNETIC FIELD DETERMINATION

Measurement of the magnetic fields is accomplished by using two magnetic field measurement instruments.

- Scalar magnetometer (cesium or helium)
- Vector magnetometer (3-axis fluxgate)

These magnetic measurements are combined with the vector magnetometer axis reference system and the spacecraft orbit position determination system to provide the mission's magnetic data.

Detection of the scalar magnetic field is accomplished by measuring the Larmor frequency (f_L), which for cesium gas is related to the magnetic field (H_O) by

$$H_O = (1/3.49847)f_L$$

where

f_L in Hertz (Hz)

H_O in nanotesla (nT)

$$1/3.49847 = \frac{\gamma}{2\pi}$$

γ = gyromagnetic ratio (1.79598)

The instrument's tracking filters multiply the f_L by a factor of 16, and the output is averaged over a period of time (T). This provides the number of counts related to the H_0 . The count reading is sampled 4 times per second with a resolution of 18 bits (one part in 218). A sample rate of 4 times per second equates to the along-track magnetic field being measured every 2 km. A minimum 30-day repeat cycle establishes the cross-track resolution that is a maximum of 0.375 degree (approximately 42 km) based on both the ascending and descending crossings at the Equator. These values, 2 km along-track and 42 km cross-track, are sufficient to provide the 100 km resolution required by the mission.

Three axis fluxgate vector magnetometer detection of the field is accomplished by driving the three orthogonal instrument cores and sampling the drive voltage required to null the field. The sensitivity of each axis is 100 $\mu V/nT$. The vector magnetometer is a stepwise scale instrument in which the steps are resolved to one part in 2000. The resolution is 12 bits which provides 4096 counts (2^{12}) per 2000 nT, yielding a resolution of 0.244 nT ($2000/4096 \times 0.5$). With 16 samples per second (each axis at a resolution of 12 bits), the along-track resolution is 500 meters but the cross-track resolution at the Equator remains a function of the ground-track repeat cycle.

The three axis resolution of the magnetic field requires an inertial reference for the vector magnetometer. Star cameras are used for this reference. Although Magsat used the NASA standard star tracker, the GRM is expected to use solid-state cameras of the Charge Transfer Device (CTD) type. To aid the star camera attitude determination system, precision sun sensors will be used. Both the star cameras and the sun sensors will be sampled 4 times per second, which is consistent with the scalar magnetometer sampling rate.

4.3 GRAVITY MODEL DETERMINATION

4.3.1 MODEL REPRESENTATION

The gravitational potential at satellite altitude can be represented by the following two ways:

- (a) A spherical harmonic series
- (b) A reference potential plus a global grid of anomalies (i.e., one-half degree equal area gravity or potential anomalies)

Both depictions of the field are useful because the localized parameters provide the benefit of a visual map and the global spherical harmonics provide the capability of analytical manipulation.

The gravitational potential of the satellite in spherical harmonics is given by

$$V = \frac{\mu}{r} \left[1 + \sum_{\ell=2}^{N_{\max}} \sum_{m=0}^{\ell} \left(\frac{a_e}{r} \right)^{\ell} \bar{P}_{\ell m}(\sin \phi) \left\{ (\bar{C}_{\ell m} \cos m\lambda) + (\bar{S}_{\ell m} \sin m\lambda) \right\} \right] \quad (4-1)$$

where

μ = gravitational parameter of the Earth (also called GM)

r = geocentric distance to satellite

a_e = Equatorial radius of the Earth

ϕ = geocentric latitude

λ = geocentric longitude

$\bar{P}_{\ell m}(\sin \phi)$ = normalized associated Legendre Polynomials of degree ℓ and order m

$\bar{C}_{\ell m}, \bar{S}_{\ell m}$ = normalized gravitational coefficients to be recovered

N_{\max} = maximum degree ($N_{\max} \approx 300$ is expected)

The potential at satellite altitude in terms of a global grid of anomaly, Δg , is defined by

$$U = U_{\text{Ref}} + T \quad (4-2)$$

where

U_{Ref} = reference potential in terms of spherical harmonics complete to intermediary degree and order N

T = disturbance potential given by the upward continuation integral (Heiskanen and Moritz, 1967) defined as follows

$$T = \frac{R}{4\pi} \iint_{\text{sphere}} S(r, \psi) \delta(\Delta g) d\sigma \quad (4-3)$$

where

$$d\sigma = \cos \phi d\lambda d\phi$$

R = radius of the reference sphere for the gravity anomalies

$\delta(\Delta g)$ = residual anomaly of Δg referred to the potential U_{Ref} at the sphere R

$S(r, \psi)$ = Stokes' upward continuation function

$$S(r, \psi) = \frac{2R}{d} + \frac{R}{r} - \frac{3Rd}{r^2} - \frac{R^2}{r^2} \left(\cos \psi (5 + 3 \ln \frac{r - R \cos \psi + d}{2r}) \right) \quad (4-4)$$

where

d , r , R , and ψ are defined as shown in Figure 4-2.

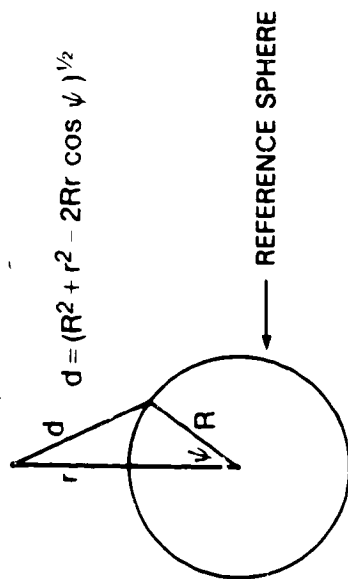


Figure 4-2. Geometry for Stokes' Equation

In the complete case where the harmonics are not truncated and the anomalies refer to point values, the two potentials are equal; namely, $U = V$.

In the discrete case, for $1/2$ deg \times $1/2$ deg gravity anomalies and the harmonics complete to $N_{\max} = 300$, the two potentials provide nearly equivalent accuracy for the GRM 1 deg \times 1 deg gravity anomaly on a global scale. From the half-wavelength rule relating the resolution of harmonics complete through degree N_{\max} to a grid size of α (degrees), namely

$$\frac{180}{N_{\max}} \approx \alpha$$

the $1/2$ deg square grid corresponds to a finer resolution of $N_{\max} = 360$ instead of 300. In local areas, such as an ocean trench and mountainous regions where the short wavelength signal has greater strength, a special solution using the global field of harmonics with $N_{\max} = 300$ as the reference potential and recovering a grid of residual anomalies ($1/2$ deg or less) over the local region could then provide refinement in the gravity field.

4.3.2 METHOD OF DETERMINATION (ESTIMATION)

Starting with the current knowledge of the gravity field, the determination method, in general, is based upon the process of expanding the GRM signal (Doppler SST) in a Taylor series of linear adjustments. This Taylor series expansion is an adjustment about the orbit parameters (both satellites) and the gravity parameters and is used to form the least squares normal equations. In addition, the DMA provided Doppler

tracking data will also be combined with the \dot{s} data in order to resolve the orbit parameters. Orbital arcs spanning a period of time, which could be up to several days, will be formed for processing the data and the least squares normal equations will be accumulated over the mission lifetime. Numerical integration techniques are the most accurate for computing the orbits and also the partial derivatives needed for the observation signal equation. Procedural techniques for the parameter estimation are being investigated in order to realize the necessary computation efficiency.

Iterative procedures for parameter estimation are dictated primarily by the large number of unknowns (N_{UNK}) in the least squares normal matrix. Using $N_{UNK} \approx 10^5$ unknowns for harmonics complete to degree and order 300, there are about 10^{10} terms (N^2_{UNK}) for a complete matrix. Since the normal matrix is accumulated over the observations, amounting to 4×10^6 points for a 6-month mission, it is important to conserve on computations by employing techniques that strongly favor sparse matrices. Because of the approximations approach, it will require a few iterations to converge on the gravity field. Computational time is discussed in paragraph 6.7.1 which shows the need for the sparse matrix techniques.

Two basic methods that conform to this process of a sparse matrix use: (1) spherical harmonic parameters; and (2) a set of grid parameters of $1/2$ deg equal area anomalies. In the spherical harmonics, analytical perturbations of Fourier series (Kaula, 1983; Wagner and Goad, 1982; Wagner, 1983; and Colombo, 1984) are employed where only cross terms between coefficient parameters of the same order (and degree parity) are considered. Since the influence of a remote anomaly on the signal is inappreciable for the $1/2$ deg equal area anomalies, a cap is used for the observation equation to remove all cross terms outside a given radius from the subsatellite point. In this latter case, the anomalies are perturbed from a spherical harmonic reference potential complete at least through a degree and order 36. A number of significant related papers which have been published by members of the GRAVSAT Data Analysis Working Group, chaired by Richard Rapp of Ohio State University, are listed in Appendix A.

A simulation of the GRM signal through numerical integration (Schutz, 1985) is in process to test the different techniques for convergence and accuracy. Application of the sparse matrix technique for the spherical harmonics may require certain orbit constraints, such as restraining the perigee from rotating and by use of long-period repeating ground tracks. These conditions are also being analyzed in the simulation analysis. The in-orbit maneuvers required for support of these techniques shall be a part of the mission flight plan.

4.3.3 RESOLUTION OF SPHERICAL HARMONICS AND ERROR ESTIMATION

From analysis of the error characteristic of the GRM signal (1σ accuracy of 1 μm/sec averaged over 4 seconds), an error power spectrum of the assumed gravity anomaly (Δg) can be estimated for the harmonics of degree l . From current knowledge of the gravity data, a power spectrum of the gravity anomaly has been obtained. The maximum degree, N_{\max} , corresponds to the point where the error power spectrum of the GRM signal becomes equal to the power spectrum of the gravity field, Figure 4-3. From this analysis, an estimate of N_{\max} of approximately degree 300 has been obtained.

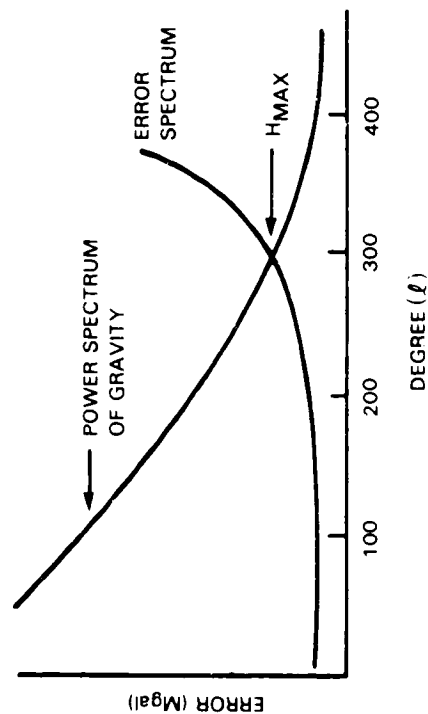


Figure 4-3. Gravity Signal Power to Noise Spectrum

Error analysis techniques have employed approximations for the gravitational perturbations for the GRM signal. The GRM Doppler signal, given by Kaula (1983) is:

$$\dot{s} = [\dot{r}_1(r_1 - r_2 \cos \delta u) + \dot{r}_2(r_2 - r_1 \cos \delta u) + (r_1 r_2 \delta \dot{u}) \sin \delta u] / s$$

where

r_1, r_2 = the respective distances to the satellites

δu = the angle between the satellite position vectors

s = the line-of-sight separation distance between the satellites as shown in Figure 3-1.

For the GRM coplanar case, the along-track component given by the last term $[(r_1 r_2 \delta u) \sin \delta u]$ in the above equation produces a dominant part of the gravitational perturbation. Although this component may be useful in an overall error analysis (as presented in the next section), the remaining terms in the above equation are necessary to adequately represent the near sectorial terms of the spectrum.

Methods for estimating the GRM goals (Δg errors) and the bound N_{\max} have employed the total energy equation and show (Keating and Smith, 1984) in a simplified way how the spherical harmonics, the GRM Doppler signal, and gravity anomaly are related, namely

$$\Delta g = \frac{\mu}{r^2} \left[\sum_{\ell=2}^N \sum_{m=0}^{\ell} (\ell-1) \left(\frac{a}{r} \right)^{\ell} \bar{P}_{\ell m}(\sin \phi) \left\{ (\bar{C}'_{\ell m} \cos m\lambda) + (\bar{S}_{\ell m} \sin m\lambda) \right\} \right] \quad (4-5)$$

$$\Delta v = \frac{1}{v} \frac{\mu}{r} \left[\sum_{\ell=2}^N \sum_{m=0}^{\ell} \left(\frac{a}{r} \right)^{\ell} \bar{P}_{\ell m}(\sin \phi) \left\{ (\bar{C}_{\ell m} \cos m\lambda) + (\bar{S}_{\ell m} \sin m\lambda) \right\} \right] \left[\begin{matrix} \text{SAT A1} \\ \text{SAT A2} \end{matrix} \right] \left[\begin{matrix} \text{SAT A1} \\ \text{SAT A2} \end{matrix} \right] \frac{\mu}{v r^2} \Delta r \quad (4-6)$$

$$\bar{C}'_{\ell m} = \bar{C}_{\ell m} - C_{\ell m}(R)$$

where

$\bar{C}_{\ell m}(R)$ = the even zonal coefficients for the reference potential of the Earth

Δg = gravity anomaly

$\Delta v = \Delta v_1 - \Delta v_2$ (gravitational perturbation)

Note: $\Delta \dot{s} = \Delta v$ (assumption), $\Delta r = r_{\text{SAT 1}} - r_{\text{SAT 2}}$

and where SAT1 and SAT2 are assumed to be in the same polar circular reference orbit.

From covariance analysis, the errors of the coefficients in the Δv equation (assuming Δr negligible for a circular orbit) can be analyzed from the GRM data and substituted in the Δg equation to estimate the commission errors of gravity anomaly. Because of the property of orthogonality of the spherical harmonics, only the diagonal terms of the covariance matrix may be considered for a simplified analysis. By use of a power law of gravity anomaly from gravimetry, omission errors can also be estimated for Δg beyond the point where the spectral term becomes equal to the commission error (\approx degree 300) as shown in Figure 4-3. Using special techniques, the gravity anomaly error can be averaged globally in a simplified way over one degree equal area blocks to estimate the accuracy goal of Δg for GRM (Jekeli and Rapp, 1980, OSU Report No. 307, and Kahn, 1982). The results from these analyses are given in Table 4-1. In addition, a result is also given (Colombo, 1981) in which correlations between the coefficients of the same order and parity were considered in the analysis whereas the previous cases were based upon diagonal terms only. The Colombo method (although approximate) is more general and the resulting slightly larger errors show the importance of the correlations. The N_{\max} values in Table 4-1 are in reasonably good agreement with the previously stated estimate of 300 for N_{\max} .

Table 4-1
GRM Error 1σ Analysis*

Investigators	$1^\circ \times 1^\circ$ Gravity Anomaly Error	$1^\circ \times 1^\circ$ Geoid Error	N_{\max}
Jekeli and Rapp	2.1 mgal	3.7 cm	313
Kahn	2.8	4.6	312
Colombo	3.2	5.7	331

*Altitude 160 km, separation 3 deg, SST Doppler $1 \mu\text{m/sec}$ (1σ) at 4-second data rate

4.3.4 GEOID ERROR AND GRAVITY ANOMALY ERROR

An estimation of $1^\circ \times 1^\circ$ geoid height and gravity anomaly errors is derived from a GRM simulation of a $1/2^\circ \times 1/2^\circ$ deg grid of gravity anomaly and geoid height over a $5^\circ \times 5^\circ$ deg region of the Tonga Trench (Figure 4-4). In this analysis, the reference potential (equation 4-2) was ellipsoidal, therefore, the residual anomalies

recovered from equation 4-3 were the full Δg values. For the recovery of the geoid height h , the upward continuation integral (equation 4-3) was modified as follows:

$$S(r, \psi) = -\frac{r^2 - R^2}{d^3} \times \frac{\mu}{R^2} \quad (4-7)$$

where

$$d = (r^2 + R^2 - 2rR \cos \psi)^{1/2}$$

and Δg was replaced by h . The results for this simulation were obtained by Lerch (1982) and are listed in Table 4-2.

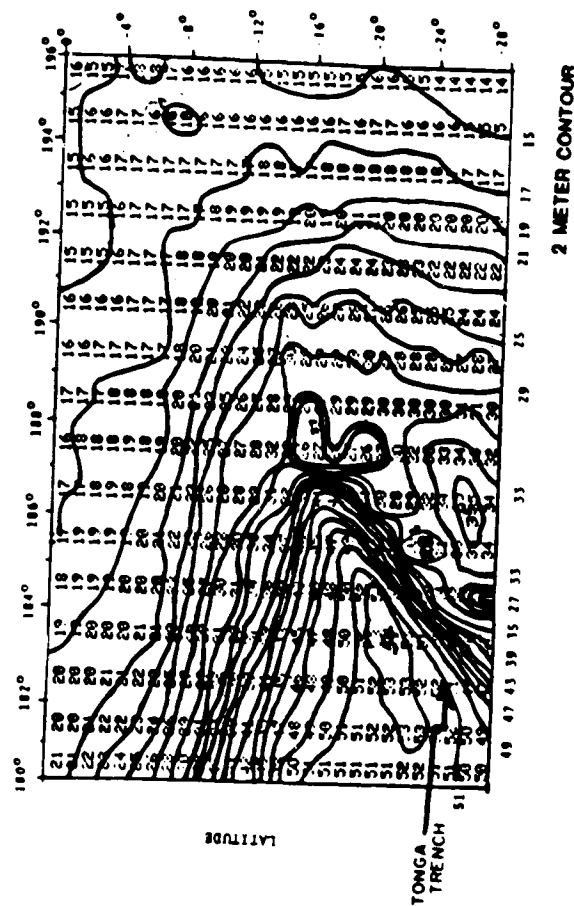


Figure 4-4. Local GEoid for Simulation

Table 4-2
 GRM* Simulation Errors for a 5 deg x 5 deg
 Region in the Tonga Trench

Parameters Recovered	1° x 1° Gravity Anomaly Error	1° x 1° Geoid Height Error
1/2° x 1/2° Geoid Heights and Gravity Anomalies	3.5 mgal	6.2 cm

*160 km altitude, 3 deg separation, 1 $\mu\text{m/sec}$ (10) SST Doppler at a 4-second data rate

These results are slightly larger than those derived from the error analysis in Table 4-1. The larger errors were not due to the steep variations in the trench area, as similar results were obtained in the 5 deg x 5 deg region away from the trench area.

More insight into the GRM gravity errors will be obtained from the global simulations that are currently in process using the spherical harmonic representation complete through degree and order 300.

4.4 MAGNETIC FIELD MODEL DETERMINATION

The magnetic field is representable in a similar manner as the gravity field; that is as a gridded spherical harmonic expansion. The field strength is directly convertible from the flight output units of frequency or counts for the scalar magnetometer instrument and volts for the vector magnetometer into nanoteslas. To provide the scalar and vector field models at satellite altitude requires the inputs of field strength and orbit position. For the vector fields (north-south, east-west, and vertical), the instrument orientation obtained from the star camera and sun sensor data is also required. The satellite's radial position to +60 meters and along- and cross-track to +100 meters must be computed from the DMA-supplied Doppler data. The orientation of the vector magnetometer axis to within 20 arc-seconds (5.6×10^{-3} degrees) must be determined.

For the spherical expansion, the useful degree is 13 ($N = 13$) for main field studies. Higher order models will be developed from the mission data.

$$V = \sum_{n=1}^N \sum_{m=0}^n \left(\frac{a_m}{r} \right)^{n+1} [g_n^m \cos m\lambda + h_n^m \sin m\lambda] P_n^m(\sin \theta) \quad (4-8)$$

$$\vec{B} = - \nabla V$$

where

- V = geomagnetic potential (tesla-meter)
- r = geocentric radial distance to the spacecraft (m)
- a_m = mean radius of the Earth's magnetic reference sphere (6371.2 km)
- λ = geocentric east longitude (degree)
- ∇ = vector operator (del) = $i \frac{\partial}{\partial x} + j \frac{\partial}{\partial y} + k \frac{\partial}{\partial z}$
- θ = geocentric colatitude (degree)
- $P_n^m(\cos \theta)$ = Schmidt quasi-normalized form of associated Legendre functions (in "modern" methodology)
- \vec{B} = magnetic field vector (tesla; actually magnetic induction)

4.4.1 MAGNETIC ANOMALY FIELD DETERMINATION

The Earth's magnetic field can be divided into three main parts: (1) the largest field which is produced by the Earth's core is the main or core field; (2) external fields that are formed in the ionosphere and magnetosphere (Parkinson, 1983); and (3) the smaller magnetic anomaly field which was induced in the varying magnetic properties of the rocks that make up the Earth's crust. Induced magnetization is generally believed to be the source of this crustal anomaly field; however, remanent magnetization may be a significant contributor. If the main and external fields of the Earth were

reduced to zero, the induced crustal anomaly field would be zero; however, the remanent component would remain.

In producing the magnetic anomaly field maps from GRM (total intensity, east-west, north-south, and vertical vector maps will be determined), it is necessary to remove these main and external fields from the observed total intensity and vector data. Numerically, this process involves subtracting a main field of the order of 25 to 60,000 nT and an external signal ranging into the thousands of nanoteslas from the observed data. The subtraction of the main field and external signal produces an anomaly value between the noise level of 2 nT up to 25 nT. The quality of the anomaly maps are determined by how well the main and external fields are removed.

A great deal of experience has been gained from the earlier POGO (Regan and others, 1975) and the more recent Magsat missions (Langel, 1982). To correct for external fields, these previous missions utilized data from only magnetically quiet periods ($K_p < 2$) and in addition, removed an analytical function representing magnetospheric currents (Langel and Sweeney, 1971). It was subsequently found (Mayhew, 1979), that geographically coincident passes had differing magnetic signatures. To rectify this inconsistency, trends were removed from these satellite data producing coincident results. The removal of a trend was done after the data were divided into three segments (-50 deg Latitude to 0 deg, -25 deg to +25 deg, and 0 deg to +50 deg). A straight line trend is used by Langel (1982), while Mayhew (1979), employs a quadratic function.

A previously determined (Langel, 1981), 13 degree and order spherical harmonic model of the main field is used to represent the large core component of the Earth's field. This model is used as a reference allowing the higher order crustal fields to be determined.

Actual production of the anomaly map was then made using the reduced measurements to create average values in blocks of 2 deg latitude by 2 deg longitude. Initially, one datum from each pass is used in a block and these results are averaged, Magsat data differing by more than a +2 standard deviation are removed from each block and a new block average is computed. Results from this procedure (for Magsat) are given in Section 2.

Since these Magsat maps were derived, subsequent work has suggested some modifications to this process. Goyal and others (1985) indicate that a least-squares collocation method has been found to produce more accurate anomaly estimates at altitudes less

than 400 Km, but essentially the same results at greater than 400 Km. Taylor and Frawley (1985) have adjusted the satellite orbital intersections (in a least-squares sense) to minimum error by applying bias and linear-trend corrections in a manner analogous to the reduction of Seasat data. Arkani--Hamed and Strangway (1985) have divided the Magsat data set into dawn-only and dusk-only orbits and have produced anomaly maps using this data selection technique. Additional work is being done on representing the anomaly data and at present, it cannot be stated definitely which methods or techniques will be applied to produce the anomaly charts from the GRM data.

SECTION 5. SPACECRAFT DESIGN

5.1 A-1 AND A-2 SPACECRAFT CHARACTERISTICS

The two spacecraft designated A-1 and A-2 differ only in the inclusion of the magnetometers, star cameras, and boom on the A-1 spacecraft. Table 5-1 provides the detailed characteristics of each spacecraft and Figures 5-1 and 5-2 show the design features of the A-1 spacecraft.

Table 5-1
GRM Spacecraft Characteristics

Features	A-1	A-2
Total Mass	2734 kg	2517 kg
Hydrazine Fuel Mass	1400 kg	1400 kg
Power		
Battery Size	Two 20 ampere-hour	Two 20 ampere-hour
Minimum Power Available	400 W	400 W
Command and Data Handling		
Data Rate	4.6 kb/s real time	2.6 kb/s real time
--Telemetry	(34 kb/s playback)	(34 kb/s playback)
--Command	125 bits per second	125 bits per second

Table 5-1 (Continued)

Features	A-1	A-2
<p>Thermal</p> <p>Overall Spacecraft</p> <p>Rigid Boom</p> <p>Structure</p> <p>Guidance and Control</p> <p>Sensing Resolution</p> <p>--Attitude</p> <p>--Attitude Rates</p> <p>--Star Cameras</p> <p>--Sun Sensors</p> <p>Control Precision Attitude</p> <p>Autonomous Onboard Guidance</p> <p>Computer</p> <p>Satellite-to-Satellite</p> <p>Doppler Tracking</p> <p>--Accuracy (1σ)</p>	<p>Heat pipes, insulation, and coatings</p> <p>Insulation</p> <p>Cruciform, natural frequency greater than 10 Hz</p> <p>Rigid boom, natural frequency greater than 8 Hz</p> <p>0.05° pitch, roll, and yaw</p> <p>0.003°/hr with DRIRU</p> <p>6.0 arc-sec (0.0017°)</p> <p>2.0 arc-min (0.033°)</p> <p>0.1°, with 20 N-m-s wheels</p> <p>64 K byte ROM</p> <p>32 K byte RAM</p> <p>1 x 10⁻⁶ m/s</p>	<p>Heat pipes, insulation, and coatings</p> <p>Cruciform, natural frequency greater than 10 Hz</p> <p>0.05° pitch, roll, and yaw with Earth</p> <p>0.003°/hr with DRIRU</p> <p>0.1° with 20 N-m-s wheels</p> <p>64 K byte ROM</p> <p>32 K byte RAM</p> <p>1 x 10⁻⁶ m/s</p>

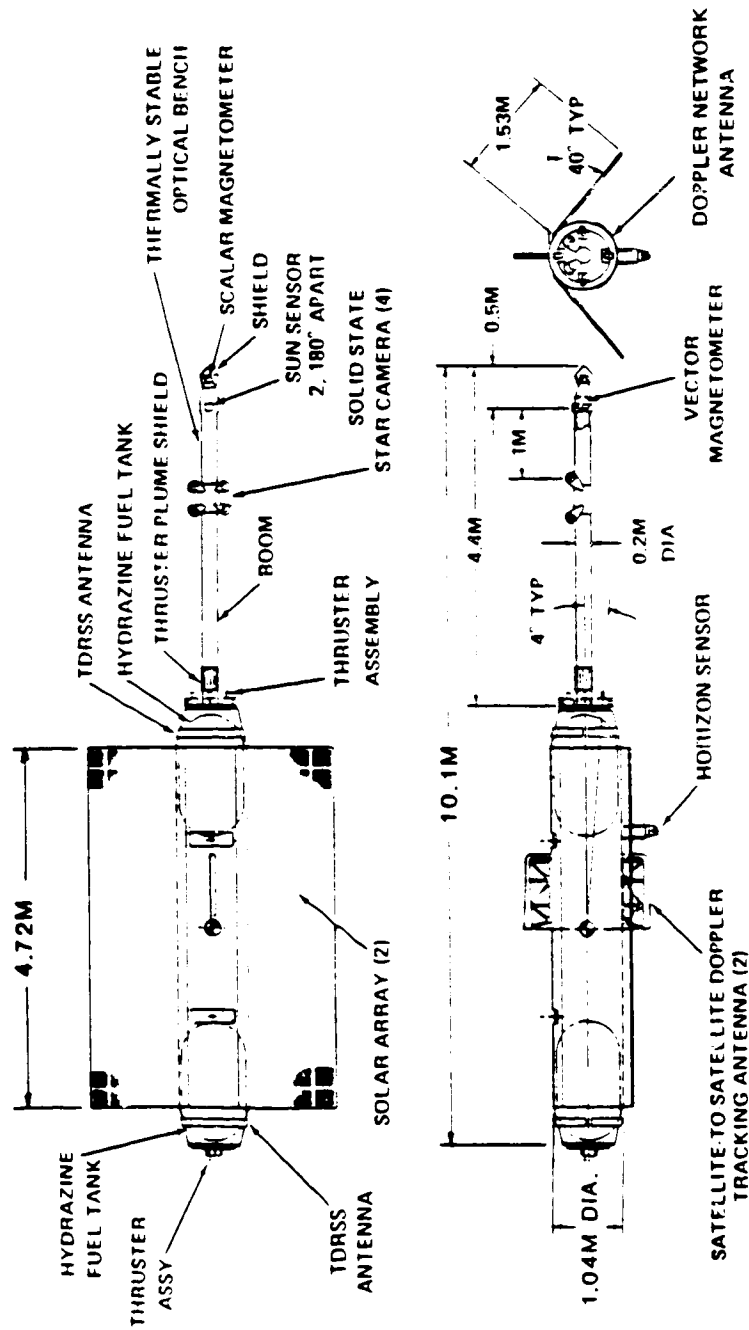
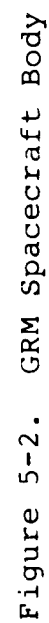


Figure 5-1. GRM Orbit Configuration (A-1)



5.2 SATELLITE-TO-SATELLITE TRACKING SYSTEM

A two way coherent Doppler measurement (MacArthur and Uthery, 1981) system will be used for making relative range rate measurements between the two satellites. Figures 5-3 and 5-4 are block diagrams of the system. Two narrow-beam antennas on each satellite will be directed at the other satellite to transmit and receive in the 42 and

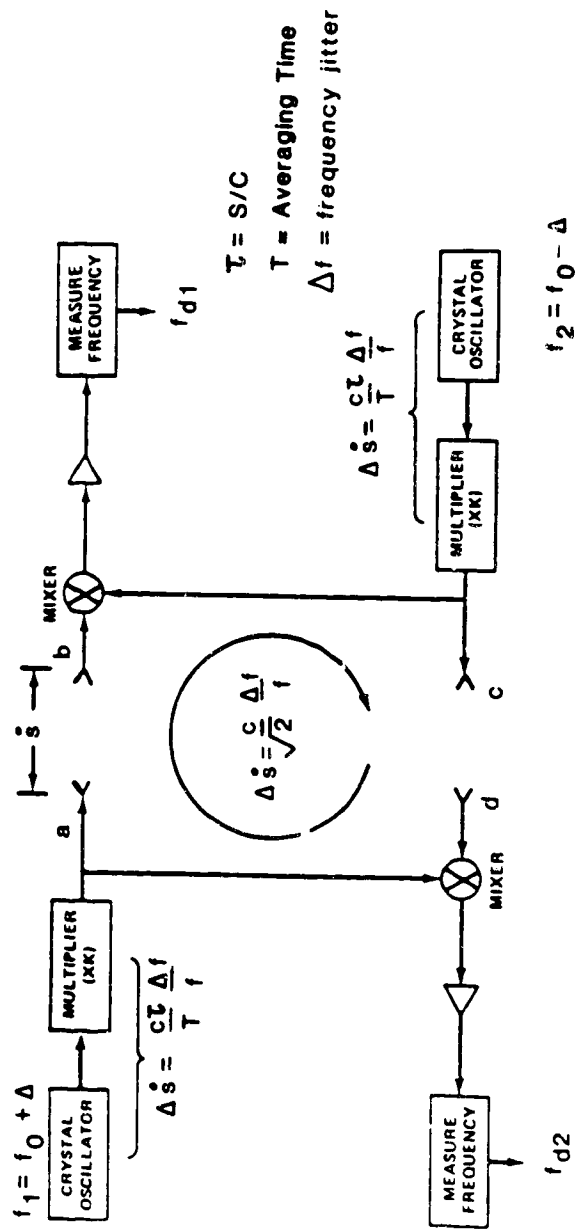


Figure 5-3. Simplified GRM SST System

91 GHz bands. A stable reference oscillator will be multiplied by the factor K to a high-frequency CW signal that will then serve simultaneously as both a transmit signal and a local oscillator. The two reference oscillators are offset slightly from nominal frequency, f_0 , and the beat frequency is formed by mixing the received signal with the local oscillator in either system and it will be a measure of the relative

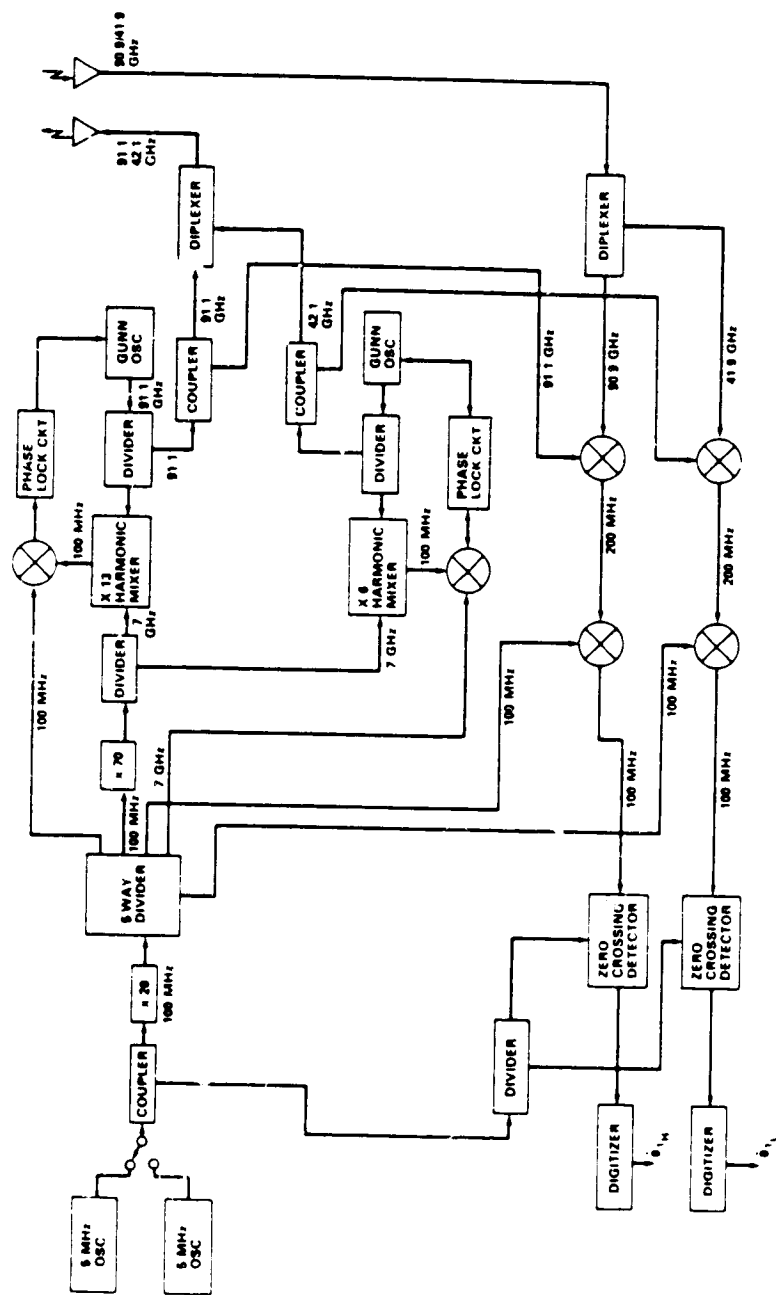


Figure 5-4. GRM Satellite-to-Satellite Tracking System

rate between the satellites via the one-way Doppler shift on the carrier signals. The Doppler frequency for a one-way transmission is given by

$$f_d = f_c \left(1 \pm \frac{\dot{s}}{c} \right)$$

where

f_d = received frequency
 f_c = transmitted frequency
 \dot{s} = separation rate of change (range rate)
 c = speed of light

For $f_c = 91 \text{ GHz}$ ($91 \times 10^9 \text{ Hz}$) and $\dot{s} = 10^{-6} \text{ m/s}$, the f_d is $91,000,000,000.0003035 \text{ Hz}$. Figure 5-4 shows an intermediate frequency (IF) of 100 MHz , which in turn is further converted to an IF of 10 kHz . Thus, the $f_{dIF} = 10,000.0003305 \text{ Hz}$. The $1 \mu\text{m/s}$ range rate is the minimum required sensitivity. For an \dot{s} of 1 m/s , the f_d is $91,000,000,303.5 \text{ Hz}$ providing an f_{dIF} of $10,303.5 \text{ Hz}$.

Frequency fluctuations in either the 91 or 42 GHz signal will have an equal and opposite effect on the signal observed in each satellite. Cancellation in the final processing would be perfect if it were not for the separation between the satellites. A phase lag between the frequency wiggles appearing at the output of each satellite, results in a less than complete cancellation. Frequency stability of the reference oscillators poses an ultimate limit on the attainable precision. Analyses have shown that today's stable crystal oscillators have fractional frequency fluctuations of a few parts in 10^{13} for which a rate precision approaching $3 \times 10^{-7} \text{ m/s}$ is predicted for a 300 km satellite separation and a 4-second averaging time. Other error sources will act to limit precision but are not expected to prevent the 10^{-6} m/s (1σ) overall requirement from being realized. These error sources are described in the following paragraphs.

5.2.1 TRANSMIT FREQUENCY AND IONOSPHERIC EFFECTS

The choice of transmit frequency does not greatly affect precision because the Doppler frequency for a given range rate and the carrier signal frequency fluctuations vary directly with the multiplying factor K .

Additive noise at each receiver input contributes to Doppler measurement noise; therefore, the transmit power must be chosen to provide a sufficient signal-to-noise ratio. By operating at the highest frequency at which the requisite transmit power can be realized with currently available solid-state devices, the effect of the ionospheric contribution to range noise is minimized. A frequency near 90 GHz has been chosen as a

baseline. At this frequency, initial calculations indicate an ionospheric error contribution of approximately 10^{-6} m/s under worst-case conditions at the Equator.

The magnitude of the ionospheric effect is illustrated in Figure 5-5. The path delay through the ionosphere is increased relative to a vacuum as a function of electron density, which in turn exhibits both geographical and temporal (day/night, seasonal) variability under the influence of solar activity. The example shown in Figure 5-5 is based on solar activity anticipated in 1985 (these conditions are a projection of anticipated data which is appropriate to the mission) and reflects a noon orbit, 0 degree longitude, 150 km altitude, 100 km separation, and 90 GHz center frequency.

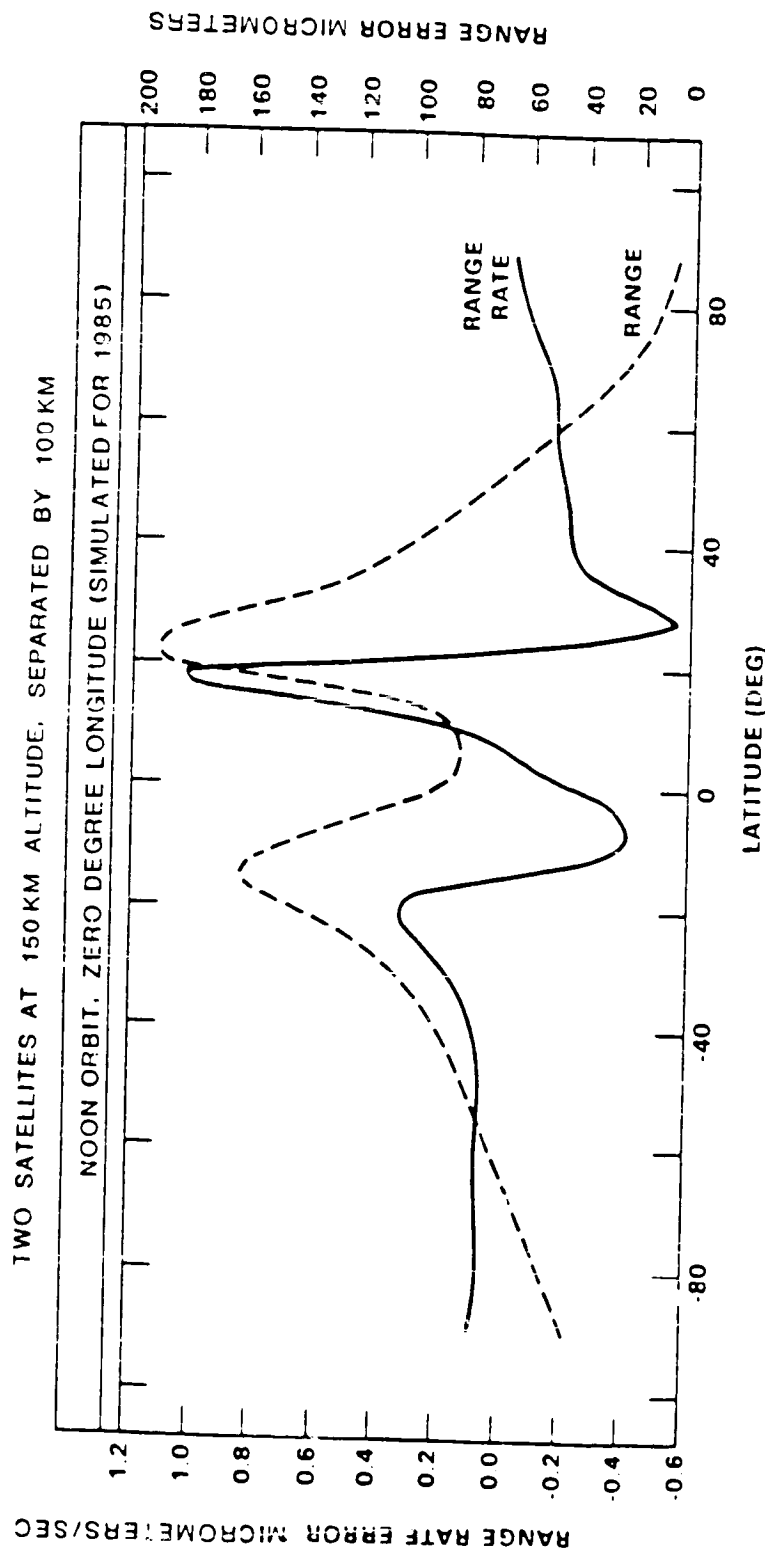


Figure 5-5. GRM Ionospheric Range and Range/Rate Error

The dual-frequency scheme will reduce the ionospheric error. The phase delay through the ionosphere is

$$\phi_o = k/f^2$$

where

ϕ_D = the phase delay

f = the transmitted frequency

k = a proportionality constant

The choice of which two frequencies involves several tradeoffs. The greater the frequency separation, the more accurate the range rate measurement cancellation process. If both frequencies are chosen to be as high as practical, then failure of either channel will still provide useful data in the absence of ionospheric correction capability. The choice of closely spaced frequencies will allow the use of common antennas and will provide better cancellation of higher order ionospheric errors. The current choice of frequencies (42 and 91 GHz) is based on maximum cancellation of the dominant first-order ionospheric error and maximum frequency separation while using a common antenna and integer multiples of the 5 MHz reference oscillator.

5.2.2 ANTENNA CONFIGURATION

The Doppler antenna configuration shown in Figure 5-6 provides the antenna performance tabulated in Table 5-2.

The antennas are pyramidal horns with adequate thermal and structural stiffness. There are phase-correcting lenses in the apertures. The separation from the spacecraft body is selected to direct the 91 GHz antenna pattern null (near the first pattern null at 42 GHz and the third pattern null at 91 GHz) at the primary multipath reflection point located at the edge of the cylindrical body. The two horns are linearly polarized with their polarization parallel with their narrow dimension. The antennas are symmetrically located about the center mass of the spacecraft to place their effective phase center coincident with the center of mass. The 1.53-deg tilt of the antenna is based on the 3.06 deg angle between the spacecraft-to-spacecraft centerline, which results from

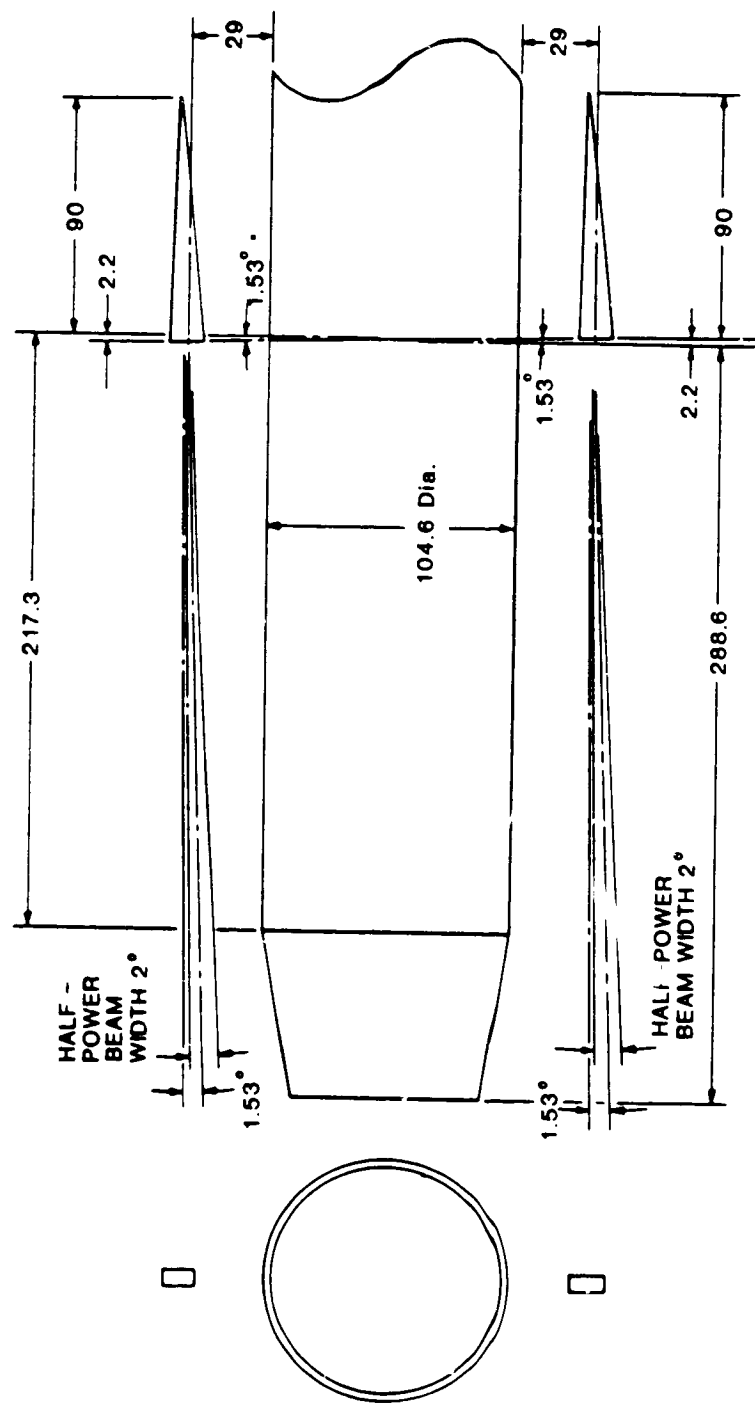
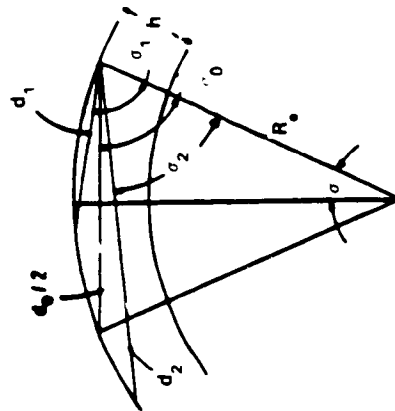


Figure 5-6. GRM Horn Antenna

Table 5-2
Doppler Antenna Performance

Parameter	Frequency
Gain (100%)	91 GHz
Beamwidth (3 dB)	36.2 dB
Skin Depth Loss	2° x 5.1°
	0.41 dB
	42 GHz
	28.7 dB
	4.7° x 11.9°
	0.27 dB

a 350 km satellite-to-satellite spacing and the orbital altitude of 160 km (Figure 5-7). The spacecraft nose includes a truncated cone that mates with the cylindrical body. This provides a reflective plane designed to minimize spurious reflections entering into the signal path through the sidelobes. To protect the inside of the horns from solar heating, it may be necessary to shield the apertures using a Teflon cover that is coated with 100 angstroms of silver. The estimated skin depth loss of such a design is shown in Table 5-2.



$d_0 = 350$ Δ Deg.	$d_1 < d_0$ d_1 Km	$d_2 > d_0$ d_2 Km
.5	235	464
1.0	121	578
1.1	99	600

$$R_0 = 6378.14 \text{ Km}$$

$$h = 160 \text{ Km}$$

$$d_0 = 350 \text{ Km}$$

$$\sigma_0 = \cos^{-1} \left(\frac{d_0/2}{h + R_0} \right)$$

$$\sigma_0 = 88.456^\circ$$

$$\alpha = 90 - \sigma_0$$

$$\alpha = 1.534$$

$$\sigma_1 = \sigma_0 + \Delta; \sigma_2 = \sigma_0 - \Delta$$

$$d_1 = 2 \times (R_0 + h) \cos(\sigma_0 + \Delta)$$

$$d_2 = 2 \times (R_0 + h) \cos(\sigma_0 - \Delta)$$

Figure 5-7. Spacecraft Separation versus Angle Off Axis

Signals reflected from the spacecraft body combine with the direct signal and cause a phase modulation as a function of pitch attitude motion. Calculations have shown that for an attitude change rate of 2.6×10^{-4} rad/s, the reflected signal must be approximately 50 dB below the direct signal to keep the effective error below 10^{-6} m/s. This degree of isolation will be achieved by the combination of low antenna sidelobes and surface treatment to break up specular (mirror-like) reflections from the spacecraft body. It will also be necessary to avoid any protuberances from the body that might intercept and diffract energy into the antennas.

The two antennas (one transmission and one reception) are mounted on opposite sides of the spacecraft body. To the degree that the effective electrical center of the antenna pair can be made to conform to the center of mass, cancellation of rate errors induced by attitude motion are illustrated in Figure 5-8.

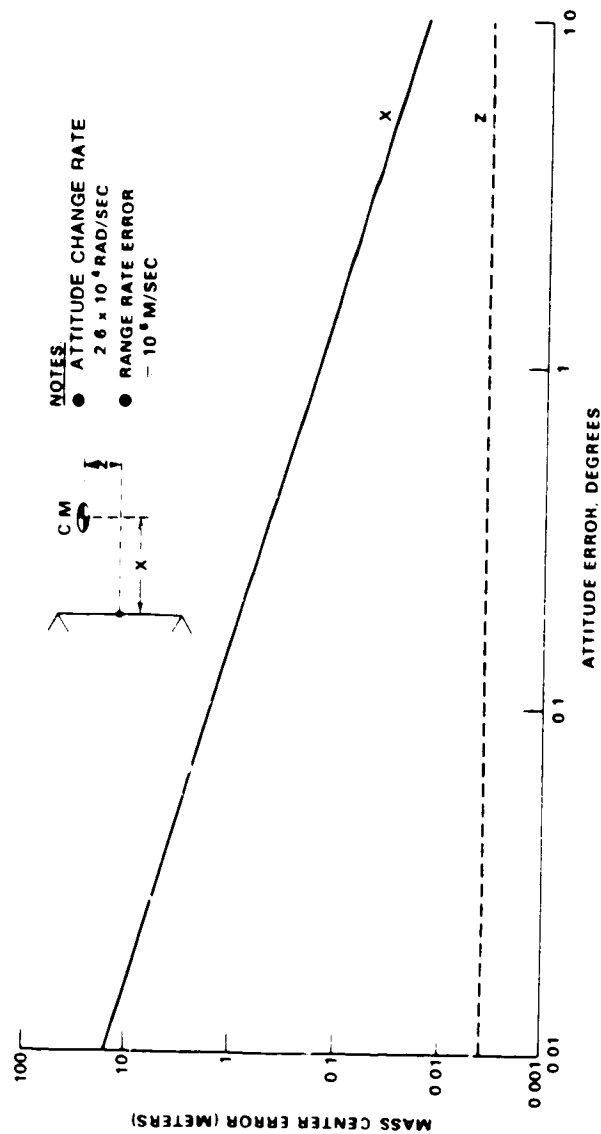


Figure 5-8. Allowable Mass-center to Antenna Phase-center Error

A maximum attitude change rate of 2.6×10^{-4} rad/s in each of three planes have been assumed. For example, this is equivalent to a sinusoidal variation of 1-degree attitude error peak and a 422-second oscillation period.

Misalignment along the line of sight (X) is better tolerated since the main component of antenna motion versus pitch or yaw is at right angles to the line of sight. If the antennas were located at the end of the spacecraft body (to eliminate all forward multipaths, the resultant required attitude control would need to be better than 0.1 degree relative to the other spacecraft. Such a scheme would require the necessity of mutual spacecraft tracking for attitude control.

Misalignment perpendicular to the line of sight (X) must be kept below 0.004 m to keep the peak error below 10^{-6} m/s, also assuming that no correction is applied based upon knowledge of attitude change rate. Differential expansion of the two antennas as a function of temperature gradients, which will vary the antenna length, is not a significant design problem.

Figure 5-8 shows a Z axis tolerance of about 4 mm. The use of exotic materials or techniques will not be required in the antenna design. Straightforward use of thermal control surfaces and/or blankets will suffice.

The choice of over and under mounting of the antennas is based upon the relative magnitude of the potential pitch and yaw motion deviations. It is desired to have the smallest antenna beamwidth in the plane intersecting the spacecraft body to minimize multipath effects. The location of the solar array fins must also be considered. The mechanical design of the antenna must allow for the effects of thruster firings on antenna phase center motions, the launch envelope restrictions, the thermal distortion of the mounting supports, and the phase-correcting lens material.

The velocity noise of the SST system (Figure 5-9) is

$$\Delta \dot{s} = \frac{c\tau}{T} \frac{\Delta f}{f} \quad (5-1)$$

where

$\Delta \dot{s}$ = velocity noise

c = speed of light

τ = the time delay between the satellites

T = s/c

Δf = the frequency jitter

T = averaging time

f = carrier frequency

\dot{s} = line of sight rate of change

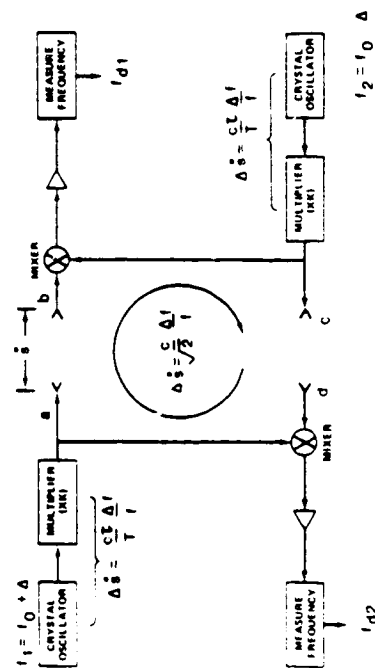


Figure 5-9. Simplified GRM SST System

The Δf , which also can be described as $\Delta\phi$, can be generated by oscillator frequency drift, mixer phase noise, and multiplier noise. Any other circuit phase noise is present in both the transmitting spacecraft radiating signal and the local oscillator circuits. As a result, the noise present in the signal received from the transmitting spacecraft is correlated with the signal generated by the local oscillator circuits of the transmitting spacecraft. The corrupted signals from both spacecraft are combined (ground processing), and the correlated noise is cancelled to the degree controlled by the time delay. If the range, \dot{s} , were zero, the phase noise would be cancelled and $\Delta\dot{s}$ would be zero. For a separation of 300 km, $\tau = R/c \approx 10^{-3}$ seconds. For a frequency jitter of 1 Hz (1 part in 9.1×10^{10}) and a 300 km separation, the cancellation would be -44 dB for a 1 second averaging time. The cancellation in dB is

$$C_{dB} = 10 \log_{10} [\sin(\pi/T) \times 360 \times \Delta f]^2 \quad (5-2)$$

Figure 5-10 shows the cancellation for two averaging times over the expected separation range.

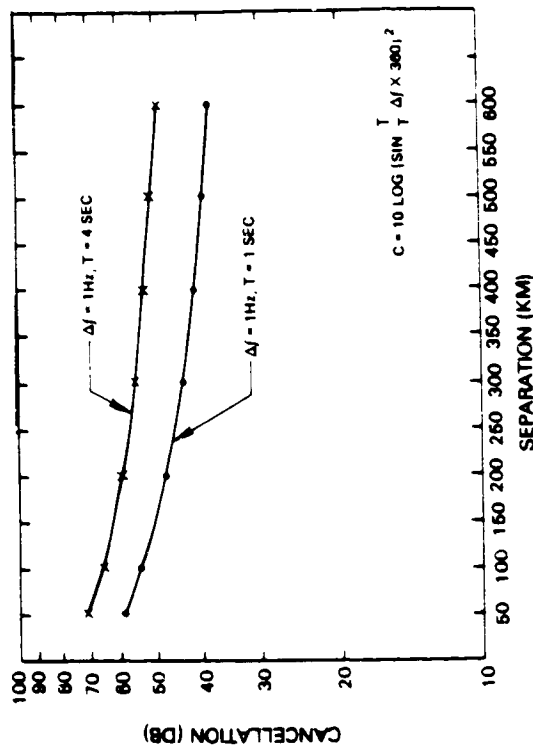


Figure 5-10. SST Phase Jitter Cancellation

Equation 5-1 does not include the external system errors such as ionosphere, multipath reflections, and movement of the phase center of the antennas due to thermal and mechanical forces. As previously described (paragraph 5.1.1), the dual frequencies of 91 and 42 GHz address the ionospheric phase delay error and the mechanical design addresses the error sources of multipath and antenna phase center movement.

5.3 DISTURBANCE COMPENSATION SYSTEM PERFORMANCE

The spherical cavity of the Disturbance Compensation System (DISCOS) is rigidly attached to the spacecraft body. The external forces acting on the spacecraft displace the electrical center of the capacitive cavity from the mass center of the proof mass or ball. This displacement must be determined and used to correct the SST data that are a direct measurement of the relative velocity between the phase centers of the antennas. This relationship is shown in Figure 5-11.

The true range (s_T) is

$$s_T = s + \delta_{x1} + \delta_{x2} \quad (5-3)$$

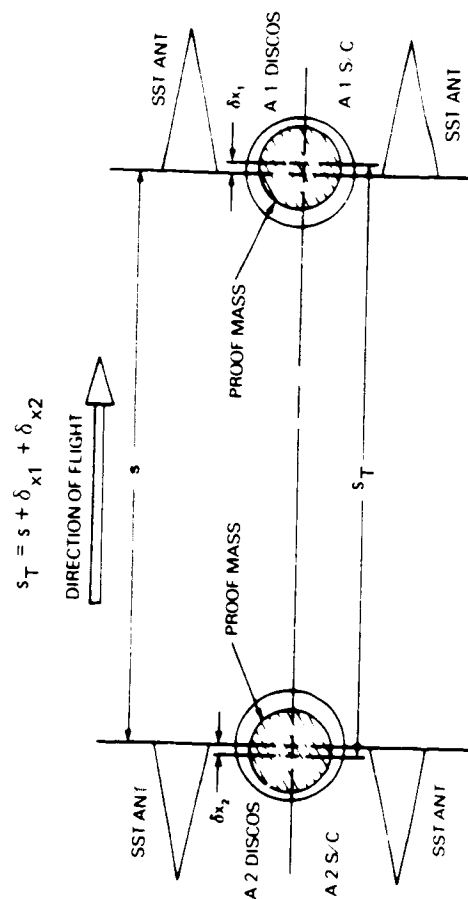


Figure 5-11. GRM DISCOS Ball-to-Ball Range Relationship

The desired flight parameter is not s_T but \dot{s}_T or v_T . Therefore,

$$\dot{s}_T = \dot{\delta}_{x1} + \dot{\delta}_{x2} \quad (5-4)$$

The SST system measures \dot{s} , and the DISCOS provides the $\dot{\delta}$ values. The signal obtained from the DISCOS is a voltage based on the position of the ball within the cavity. Periodic sampling (e.g., at a 0.1-second time interval rate) provides the delta voltage (ΔE) proportional to $\dot{\delta}x$. Therefore, the DISCOS performance is an additional and crucial parameter effecting the gravity field measurement task.

Three factors related to the DISCOS performance are:

- Calibrating the scale factors (i.e., $\Delta E/\Delta X$, $\Delta E/\Delta Y$, and $\Delta E/\Delta Z$ for all positions of the ball within the cavity)
- Periodically measuring the in-flight ball position at the necessary rate for SST data correction
- Determining the in-flight stability of the calibration

For one axis, the measured position of the ball is (Ray, Jenkins, and Junkins, 1981)

$$X_m = K_{11} X [1 + K_{12} X^2 + K_{13} (Y^2 + Z^2)] - K_{11} K_{10} [1 + K_{12} K_{10}^2 + K_{13} (K_{20}^2 + K_{30}^2)] \quad (5-5)$$

where

X_m = measured position

X , Y , and Z = true offsets from the cavity center

K_{11} = scale factor = a_{x1}/a_{x2}^2 = ball radius/ball-to-wall gap
 $K_{11} = (0.7)/(10^{-2})^2$ m

K_{12} = factor $1/a_{x2} = 10^4$

K₁₃

= factor a_{x3} = cavity radius = 0.8 m

K₁₀, K₂₀, and K₃₀ = fixed offsets of the SST phase centers to the electric center of the cavity

Similar expressions for Y_m and Z_m are inferred from the foregoing equation. Analysis of the related proof-mass position equations and error sources have been provided by Yansouni and De Bra (1974), Ray, Jenkins, and Junkins (1981), and Junkins (1984). In addition, a separate analysis of the DISCOS was provided by Vijayaraghavan and Sonnabend (1982).

The work performed by Junkins (1984) sized the problem of performance accuracy by normalizing K₁₁ and simulating errors based upon initial offsets (K₁₀, K₂₀, and K₃₀) and scale factor (K₁₁, K₁₂, and K₁₃) errors. Junkins also followed up the Ray, Jenkins and Junkins 1981 work by analyzing the coast-arc (i.e., the parabolic displacement of the proof mass along the direction of flight due to drag forces and drag makeup thruster action) as defined in the following equation

$$X(t) = X_0 + v_0 t - \frac{1}{2} a_d t^2 \quad (5-6)$$

where

X_0 = position after thruster firing

v_0 = Δv provided by the thrusters after thruster firing based on the control laws

a_d = external aerodynamic drag forces

If equation 5-5 is simplified by setting all cross-coupling terms equal to zero and no orthogonal positional offset in the ball position, the equation becomes

$$X_m = K_{11} [X + K_{12} X^3] \quad (5-7)$$

With $K_{12} \approx 10^4$, the calibration accuracy of K₁₂ becomes a critical parameter. Since it is not possible to accurately estimate either the thruster imparted \dot{s} , or the drag acceleration, a_d , the value of $X(t)$ cannot be determined to the accuracy necessary for providing the required $\dot{\delta}_x$ without determining the x_m from the DISCOS outputs. Equations 5-6 and 5-7 are a simplification of the problem, but these equations can be used to determine DISCOS performance and calibration needs.

Consideration has been given to alternate DISCOS designs that would provide either of the following functions:

- Create a two-stage DISCOS in which the SST system and the DISCOS would be independently (magnetically) suspended within the spacecraft. This would allow the ball to be maintained very close to the center of the cavity and greatly simplify the calibration of the DISCOS and the SST data processing. In effect, the SST would be tracking ball-to-ball instead of spacecraft-to-spacecraft.
- Provide an onboard DISCOS ball position measuring system that is independent of the DISCOS outputs. Such a system would provide the means of maintaining a calibration history of the instrument.

The DISCOS performance impact on the accuracy of the gravity field is considerable. The present design is based upon the successful TRIAD experience and it is sufficiently robust to provide the needed data outputs. Calibration and stability are a major concern. Alternate designs and augmentation of the existing design are being considered on the basis of either relieving the demands on the instrument by modification of the system design, or by in-flight calibration both of which also provide a simplification of the data processing. If the inclusion of a laser Doppler experiment on the GRM should prove desirable and feasible, the laser Doppler measurements would be improved considerably by the alternative DISCOS designs.

5.4 DISTURBANCE COMPENSATION SYSTEM INSTRUMENT DESIGN

The DISCOS shown in Figure 5-12 is an unsupported spherical ball in a spherical 3-axis capacitive cavity. When placed in a zero-g field, the ball floats within the cavity, thus changing the cavity's capacity as a function of its position. If the DISCOS is housed within a spacecraft and shielded from all external forces and is responding only to the gravitational potential, it provides the means to: (a) fly a drag-free orbit, and (b) to detect the gravity field potential existing at the orbital altitude. This section discusses the instrument and its role in the spacecraft guidance and control system.

Drag-free satellites have been studied since the early 1960's by Stanford University, Johns Hopkins University/ Applied Physics Laboratory (JHU/APL), and ONERA (France). The TRIAD, a U.S. Navy navigational satellite launched in 1972, was equipped with a DISCOS that was jointly developed by APL and Stanford. This satellite's 2 years of successful operation proved the drag-free concept. An APL/Stanford review of the TRIAD design indicated that the TRIAD technology is adaptable to the GRM mission. Although more detailed design work will be performed, studies have shown that 0.1 $\mu\text{m/s}$ minimum sensitivity can be achieved by modification of the TRIAD DISCOS sensor. The GRM design performance shown in Figure 5-13 is compared with the TRIAD performance and the results are listed in Table 5-3.

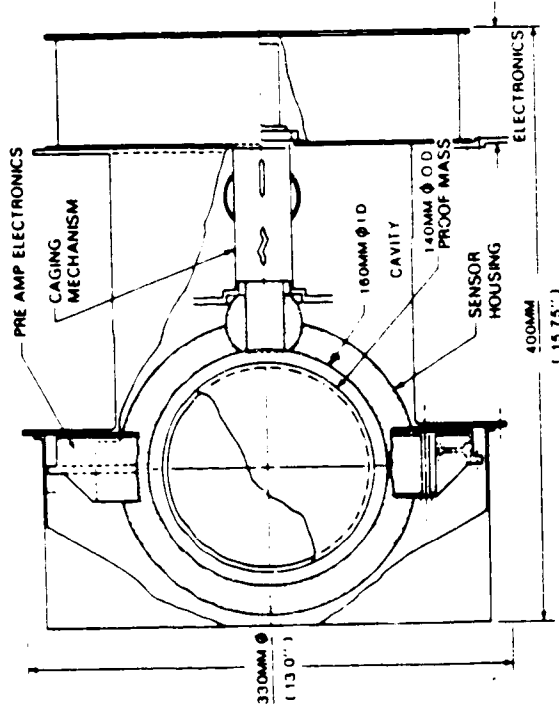
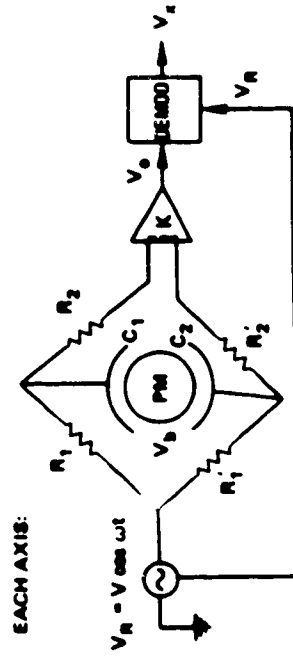


Figure 5-12. GRM Discos Design

CAPACITIVE SENSOR ANALYSIS



Transfer Function:
$$\frac{V_o}{V_R - V_b} = \frac{K \omega s (\delta C + \frac{C_o}{R_{10}} \delta R)}{s^2 + s^2 b + j(s + 2b)}$$

Capacitance: C_b = plate-to-shield ("stray capacitance")
 C_A = plate-to-ball ("active capacitance")
 (ball centered)
 $C_o = C_b + C_A$

Define: $R_{10} = (R_1 + R_1')/2$ $\delta C = (C_2 - C_1)/2$
 $R_{20} = (R_2 + R_2')/2$ $a = R_{10} \omega C_o$
 $\delta R = (R_1' - R_1)/2$ $b = R_{20} \omega C_o$
 $C_o = (C_1 - C_2)/2$

Figure 5-13. GRM DISCOS Schematic Diagram

Table 5-3
TRIAD/GRM Parameter Value Comparison

	TRIAD	GRM
Ball/Housing Radii, (mm)	11/20	70/80
CA, pF	0.31	7.10
CS, pF	39.5	~33
R10, k Ω	22.6	8.0
R20, k Ω	2.26	2.5
Scale Factor, V_x/x , V/mm	0.78	22.8
Amplifier Gain, V/ μ A	222.8	15.6
$\partial V_x/\partial C$, V/pf	26.9	38.6
$\partial C/\partial x$, pF/mm	0.029	0.59
$\partial I/\partial x$, μ A/mm	0.054	2.3
$\omega/2\pi$, MHz	1.03	1.03
Reference Voltage, V	4.5	1.6
a, b	5.82, 0.58	2.06, 0.64

The GRM DISCOS consists of the proof mass, capacitive position sensor, housing (cavity), and associated electronics. The DISCOS sensor outputs are used by the Guidance and Control System (GCS) for controlling the thrusters and for correcting ball-to-ball relative motion caused by external forces.

The preliminary DISCOS performance requirements are:

- Ball-to-spacecraft relative velocity knowledge within $0.1 \mu\text{m/s}$ (1σ) with a 4-second averaging time
- Three-axis disturbance compensation within 10^{-9} g, rms, over the frequency range of 0.001 to 0.5 rad/s

To meet the 10^{-9} g, compensation requirement, the satellite must follow the ball without touching it. Satellite/ball interactions exist because of mass attraction, electric and magnetic fields, residual gas pressure, and radiation pressure. The 1972 flight of the Navy navigational satellite TRIAD demonstrated that these disturbances can be kept below 10^{-11} g.

Thruster control will place a less stringent requirement on the DISCOS sensor than the need for precise velocity information accurate to within $0.1 \mu\text{m/s}$. In a capacitive sensor of the TRIAD type, contributors to this error include ball center of mass offset, ball shape, pickoff noise, thermal deflections, and structural flexure. Since the requirement is for velocity accuracy, absolute null stability is not required and contributors varying slower than about twice per orbit are unimportant. Also, high-frequency (200 times orbital period) disturbances can be filtered out. Studies at Stanford and APL have shown that careful mechanical design can reduce the velocity error to the limit of pickoff noise. This source can be made acceptably small by making the cavity diameter about 160 mm (four times the TRIAD diameter), which increases active capacitance and thus signal-to-noise ratio. The 160 mm sensor has an estimated velocity noise capability of $0.1 \mu\text{m/s}$, with a 4-second averaging time. This is based upon interpolation of laboratory noise measurements of two different sensors at Stanford.

The DISCOS instrument shown in Figure 5-12 is estimated to weigh about 15 kg. Like TRIAD, the housing will be fabricated of beryllium oxide because of its excellent thermal conductivity, near-zero electrical conductivity, acceptable dielectric constant, and uniform density. The 160 mm housing is about the largest size that could be made of beryllium oxide with available technology. The capacitive sensor plates are plated directly on the cavity inner surface to ensure dimensional stability. Plate geometry, electronics, and caging mechanisms are similar to those of TRIAD. The ball material has not been selected. Aluminum is acceptable, and a 140 mm diameter ball would have a mass of 4 kg.

5.5 PROPULSION

5.5.1 PROPULSION SUBSYSTEM

The propulsion subsystem (Figure 5-14) provides the thrust to counteract the atmospheric drag force in all directions and to keep the reference mass centered. It also provides rotational torque around all axes to unload the reaction wheels and it has the capability to back up the momentum wheels by direct jet control. The thrusters are arranged in parallel redundant groups that are fed through cross-connected latching valves for maximum safety and reliability.

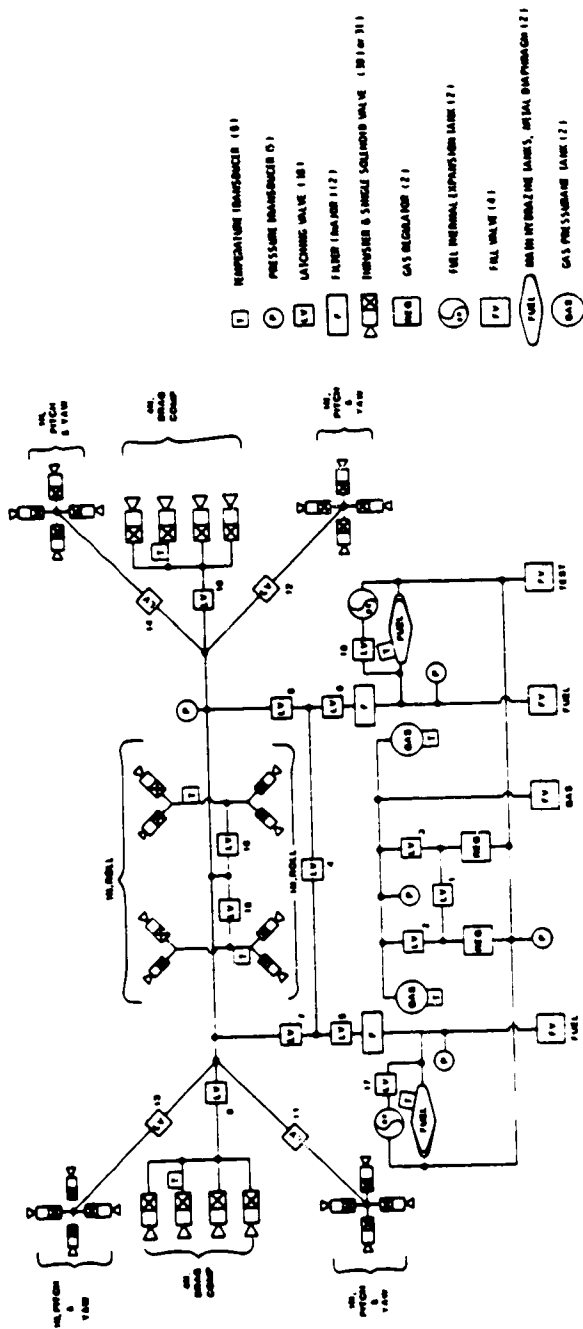


Figure 5-14. GRM Propulsion Schematic Diagram

The propulsion subsystem consists of two 0.97 m diameter metal diaphragm liquid hydrazine fuel tanks, two 0.35 m diameter pressurant gas tanks, and two 35 kg ullage tanks. To minimize mass attraction, all tanks are placed symmetrically equidistant from the proof mass.

The propulsion system schematic diagram shows the interconnecting fuel lines and commandable latching valves that allow equal fuel consumption from each tank by the thrusters. The gas tanks that pressurize the fuel are interconnected to a common, dual, pressure regulating system to ensure equal consumption from each gas tank and a constant fuel pressure of about 2,000 kilopascals (300 psi). A mass-sensor system will be incorporated with each fuel tank to allow measurement and control of its contents. Initially, the system contains approximately 1400 kg of liquid hydrazine fuel. This is distributed to redundant sets of catalytic rocket thrusters, producing 2.8 million newton-seconds of thrust for counteracting drag and controlling the spacecraft position.

The thrusters, arranged in redundant groups that are fed through redundant latching valves, are described as follows:

- The GRM spacecraft uses eight 4-newton (1 lb) thrusters for drag force counteraction. The aft end of the spacecraft will use four thrusters for drag force compensation with their thrust axes aligned through the center of the DISCOS cavity. The forward end will use four thrusters operating in pairs. Their axes will be aligned with the center of the proof mass, but the need to cant the thrusters to clear the rigid boom requires the thrusters to be fired in pairs. The 4-degree cant angle contributes to 0.25 percent loss of thrust, which is negligible. For a single thruster, the orthogonal thrust with its 7 percent loss and induced torque are unacceptable.
- Each spacecraft uses eight 1-newton (1/4 lb) thrusters for yaw momentum unloading and side translation control. Four thrusters at each end of the GRM spacecraft are used in opposite-end pairs. Their thrust axes are in the horizontal plane that is coincident with the cavity center.
- Each spacecraft uses eight 1-newton (1/4 lb) thrusters for pitch momentum unloading and vertical translation control. Four thrusters at each end of the GRM spacecraft are used in opposite-end pairs. Their thrust axes are in the vertical plane that is coincident with the cavity center.
- Each spacecraft uses eight 1-newton (1/4 lb) thrusters for roll momentum unloading. Four thrusters are each located at the top and the bottom on the GRM spacecraft close to the vertical axis of the proof mass to minimize cross-coupling. They are used in opposite-end pairs. Their thrust axes are angled inward from tangent to the GRM skin to minimize exhaust gas impingement on the solar panels.

At launch, the fuel tanks will be fully loaded with hydrazine allowing the ullage tanks to receive any overflow caused by thermal expansion either during a normal Orbiter mission or during an emergency landing. The estimated heating of the fuel by Orbiter thermal transients will cause less than 2 percent expansion of the fuel and this will be safely contained in the ullage tanks. After departure from the Orbiter, the regulated gas system will be actuated and will equally pressurize the fuel tanks. To minimize mass attraction unbalance on the DISCOS, the fuel mass distribution in the tanks will be kept nearly equal throughout the mission.

5.5.2 AERODYNAMIC DRAG ANALYSIS AND FUEL CONSUMPTION

Detailed mathematical modeling of the drag has been conducted by APL, the Air Force Geophysical Laboratory (AFGL), and the Air Force Aeronautical Laboratories. To use such models, it is necessary to select an applicable normal and tangential surface accommodating coefficient.

Based on a long history of orbiting spacecraft, the frontal surface drag coefficient of 2.0 to 2.2 has been accepted as valid. Estimation of the lateral surface drag is more difficult because it is a function of spacecraft velocity, ambient gas velocity, and the angle of the impinging atmospheric gases. Furthermore, the distribution on the lateral surfaces is not uniform. For the GRM spacecraft, the angle of arrival based on a 7.8 km/s spacecraft velocity and a 1 km/s gas velocity is 7.31 degrees. Measured surface tangential accommodation coefficients for angles that small are not available. Recent test data (Herrero and Cagiano, 1985) indicate that lateral surface drag will be less than presently estimated. The results of the GSFC test program are discussed in paragraph 6.6 of this report. At present, the design of the propulsion system is based upon the lateral surface drag estimation (Herrero, 1984) obtained from spacecraft flight data (Robertson, 1971).

The main problem with the flight data-based estimations is that variations in atmospheric density and recorded variations in fuel consumption or orbit life-time or accelerometer data are of the same magnitude, making it difficult to identify the drag associated with the lateral surfaces. The GRM drag coefficient normalized to the projected frontal area of 1.06 m² is estimated to be 3.5. The drag force is computed from

where

$$C_D = 3.5$$

$$A = 1.06 \text{ m}^2$$

$$F_D = \frac{C_D}{2} A \rho v^2$$

ρ = density as a function of altitude, latitudinal angle, and solar flux

$$v = 7.8 \text{ km/s}$$

Prediction of the solar flux (Figure 5-15) and fuel consumption was done by the GSFC's Flight Dynamics Division, using a Harris-Priester atmospheric model. The daily fuel consumption rate was computed using the I_{sp} , drag coefficient, projected area, and altitude values shown in Figure 5-16.

The fuel budget, tabulated in Table 5-4, is based upon the 230 average solar flux (1991 flight), the descent maneuver fuel consumption of 142 kg for A-1 and 150 kg for A-2, and an additional 44 kg of fuel required to increase the separation from the initial 150 km to the final 550 km.

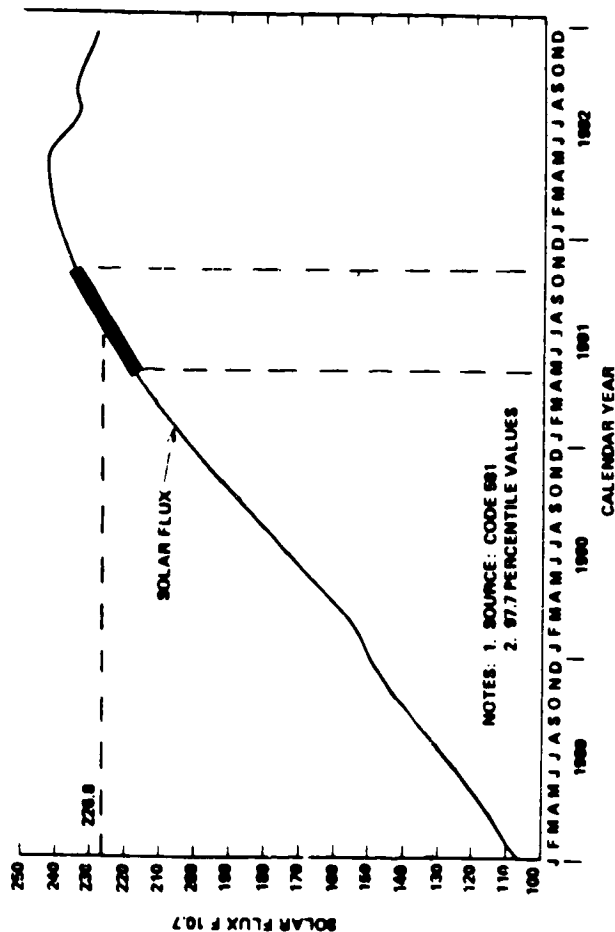


Figure 5-15. Predicted Solar Flux at 10.7 cm Wavelength

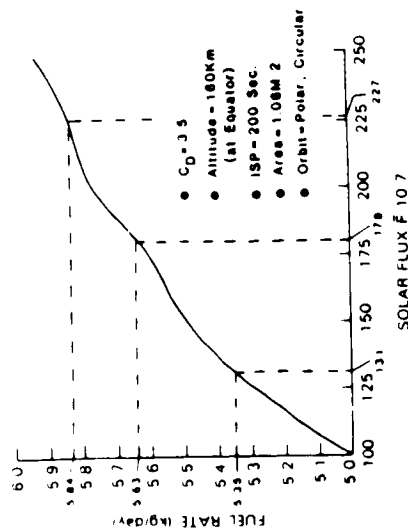


Figure 5-16. GRM Daily Fuel Consumption

Table 5-4 does not include the effects of cross winds because an onboard flight attitude control system reduces the effects of drag by heading the spacecraft into the wind. The complex problem of variable wind direction and surface accommodation coefficients related to the angle of attack requires further study. Worst-case assumptions were used to determine the fuel requirements for this conceptual design.

5.6 POWER SUBSYSTEM

The power subsystem is a peak-power tracker system used on the Geosat spacecraft with 20 ampere-hour batteries and a fixed solar array. The subsystem size, based on 156 W/m² solar array output, is capable of supporting an orbit average load of 400 W.

Table 5-4
GRM Fuel Budget Summary

	A-1 Spacecraft (kg)	A-2 Spacecraft (kg)
Descent and Checkout	142	150
180-Day Mission	1051	1051
150 to 550 km	26	18
Total	1219	1219
Available	1400	1400
Margin	181	181

The 17 m² solar array configuration is shown in Figure 5-17. Because of the polar orbit and nadir pointing, the sun position will project a cone with respect to the pitch axis of each orbit and the cone half-angle could be anywhere between 0 and 90 degrees. Movable solar arrays are unacceptable because of their perturbing momentum and asymmetric aerodynamic loading effects on the DISCOS and the guidance and control system.

The resulting solar array configuration consists of body-mounted cells on the upper 4.72 m long spine of the spacecraft and two 4.72 by 1.53 m solar array fins attached tangentially to the spacecraft that are at an angle of 40 degrees from horizontal. The resulting minimum sustainable load is 400 W and occurs at a sun cone angle of 48 degrees. The design features use high efficiency solar cells and a heat-pipe thermal distribution scheme (Figure 5-18). The orbital average power output and sustainable load versus cone angle is shown in Figure 5-19. The required load for each spacecraft is listed in Table 5-5.

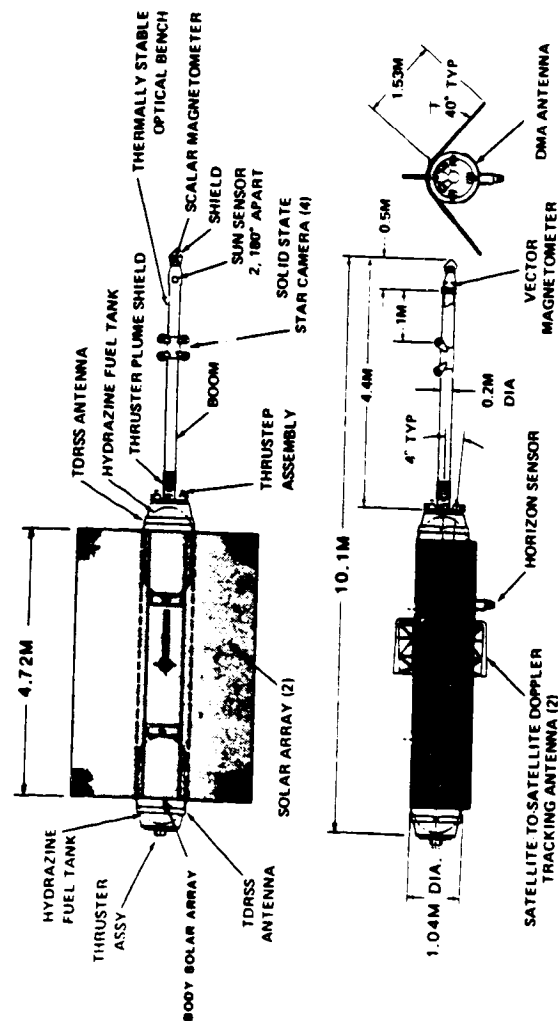


Figure 5-17. Solar Array Emphasis; GRM Orbit Configuration

K6700 SOLAR CELL

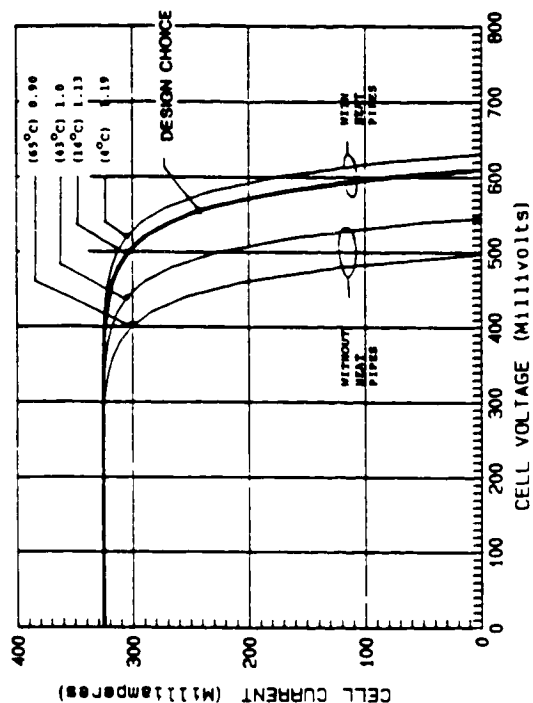


Figure 5-18. Operating Points for Peak-power Tracker

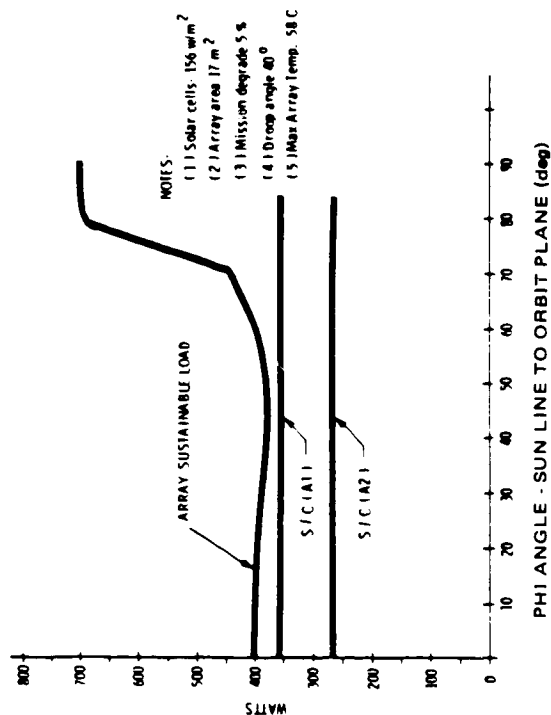


Figure 5-19. Power versus Load

Table 5-5
Power Load Budget

Subsystem	A-1 Spacecraft (W)	A-2 Spacecraft (W)
Spacecraft Bus	218.7	218.7
Gravity Instrumentation	45.0	45.0
Magnetic Instrumentation	88.9	--
Total	352.6	237.7

5.7 THERMAL SUBSYSTEM

The thermal design accommodates the extremes of solar flux, from a steady state at either side along the pitch axis (twilight orbit), to the Sun in the orbital plane rising 13 degrees below the nose proceeding across the back, and setting 13 degrees below the tail (noon orbit). The Earth and albedo fluxes are large and, because of the 160 km altitude, are fairly constant on an orbital average basis. The aerodynamic fluxes are approximately 0.3 Suns acting on all leading surfaces. Because of these extremes of flux and the need for spacecraft dimensional stability for the DISCOS, the conceptual thermal design uses the lower half of the spacecraft as a radiator for internally generated power and isolates the upper body and solar arrays from the lower body and from each other.

The solar array is fitted with solar cells on the space side and buffed aluminum on the under side. A 100 percent coverage of solar cells is necessary for power considerations, and the buffed aluminum provides a measure of thermal isolation from the spacecraft body. The array substrate is fitted with sixteen ammonia, grooved heat pipes on 22 cm centers that have a 2 cm diameter and 460 cm length. The worst-case load on these pipes is 24,000 watt-centimeters (W-cm) and their dryout capacity is 71.50 W-cm. The pipes lie parallel in the pitch-yaw plane direction. The heat pipes provide orbital average array temperatures of +17 deg C in the noon orbit ($\psi = 90$ deg) to +15 deg C in the twilight case ($\psi = 0$ deg) with a colder array in the $\psi = 30$ deg case. These temperatures maximize solar ψ array efficiency and minimize the spacecraft-induced sunside/darkside gradients for low orbits. The solar array is mounted to the cruciform structure through the outer shell on thermally isolated standoffs.

The upper spacecraft shell is buffed aluminum on the outside, multilayered aluminized kapton on the inside, and fitted with eleven 1 cm diameter, 570 cm length, ammonia, grooved heat pipes from front to back. Eighteen equally spaced semicircular heat pipes of the same type are provided to smooth out circumferential gradients. The loads on these pipes and the ones on the lower shell are far below the 13,680 W-cm dryout capacity of these pipes.

The lower spacecraft shell is the thermal radiator for the internal thermal dissipation of the spacecraft. The major view from the exterior thermal control surface (8.4 m²) is towards the Earth, therefore, large amounts of thermal flux cannot be dumped. With only about 290 W to be dissipated, the required flux to be dumped is 33 W/m².

Preliminary analysis shows that with an effective emittance of 0.55, the thermal performance calculations show worst-case temperatures of 14 deg to 19 deg C, which is adequate. The heat pipes in the shell provide a nearly isothermal radiator. The coating on the inside of the shell is high emittance (0.85).

The mechanical mounting of the SST Doppler antennas to the part of the structure containing the DISCOS will be of low thermal expansion material, insulated from the environment, and held at a stable temperature with heaters.

The thermal design for the GRM's magnetometer system will be similar to that of the Magsat-A. The vector and scalar magnetometers housed at the end of the rigid boom will be equipped with active heaters to stabilize the instrument temperature. Active heaters will also be used with the star camera/vector magnetometer package. The deployed rigid boom will use multilayer thermal insulation with a resultant α/ϵ ratio of 1.2. The radiating face of the scalar magnetometer will have a α/ϵ ratio of 0.24.

5.8 STRUCTURE SUBSYSTEM

5.8.1 SPACECRAFT

The two spacecraft are structurally identical except for the A-1 spacecraft boom that supports and houses the magnetometers, sun sensors, optical bench, and star cameras. The internal structural details are shown in Figure 5-20. The main features of the design are as follows:

- a. An aluminum honeycomb/facesheet cruciform panel primary structural element supports all the assemblies and systems.
- b. Strong aluminum rings at either end of the cruciform support the two 0.97 m diameter propellant tanks and provide the load path and linkage between the spacecraft and the cradle (Figure 5-21) used for supporting the spacecraft in the shuttle bay.
- c. An outer monocoque shell secondary structural element supports both the circumferential and the longitudinal heat pipes
- d. Both spacecrafts have a transition to a conical structure that allows an external payload mounting area. The forward (reverse thrust) thrusters are located on a

0.4 m circle allowing an available mounting area of an approximate 0.3 m diameter. The hinge/boom system occupies this mounting area on the A-1 spacecraft while the space is unassigned for the A-2 spacecraft.

- e. The hinge/boom system allows the boom to be folded back alongside the spacecraft during launch (Figure 5-21) and then deployed to a locked position as shown in Figure 5-22.

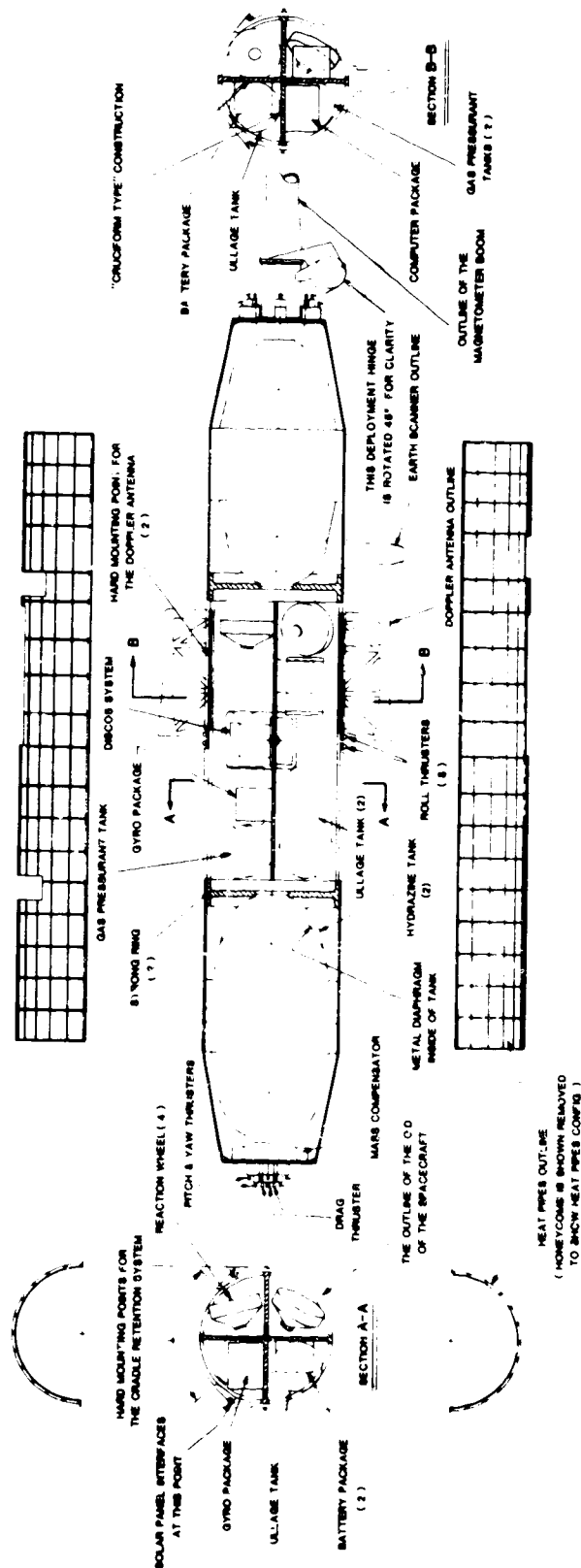


Figure 5-20. GRM Internal Configuration

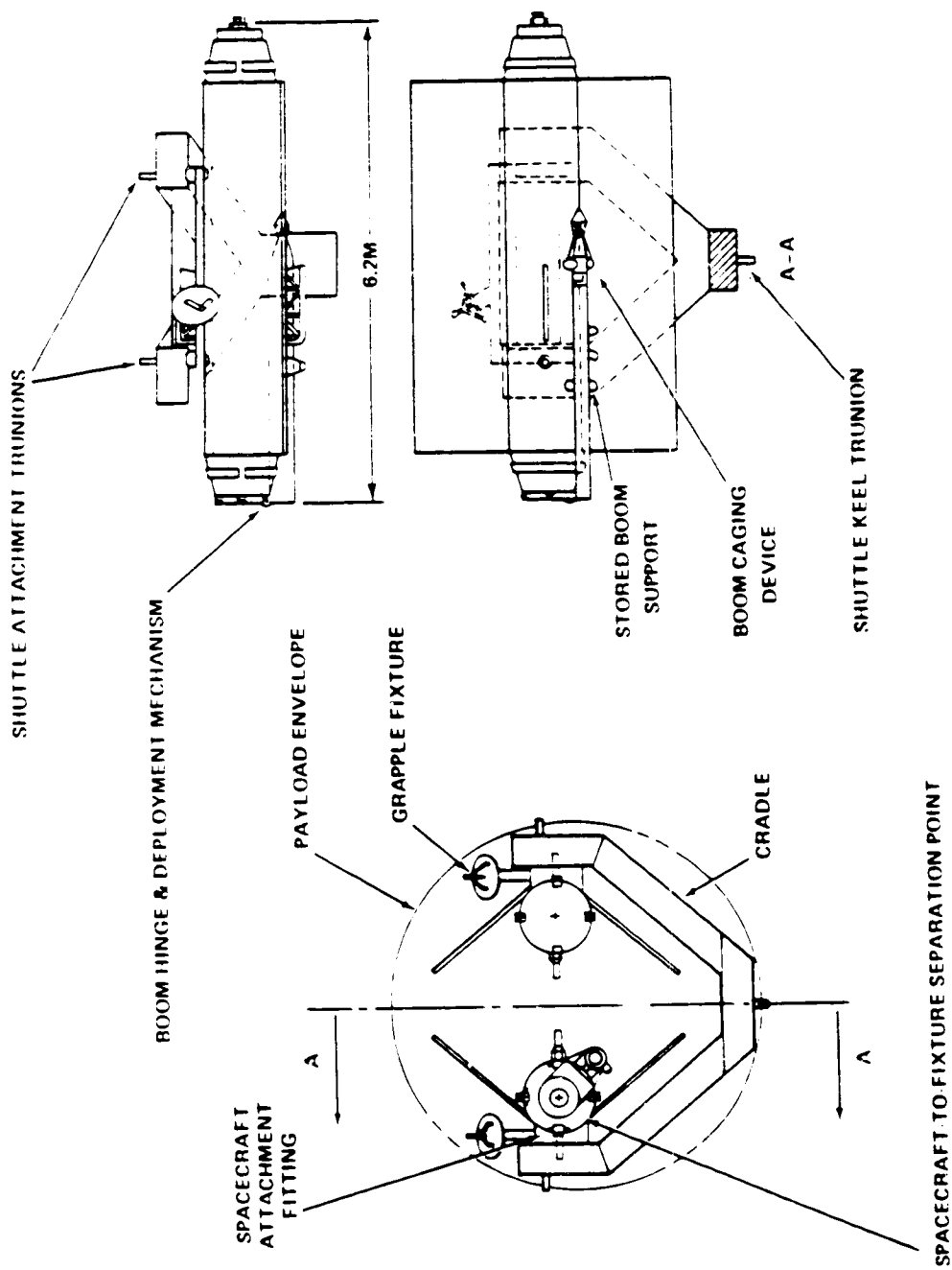
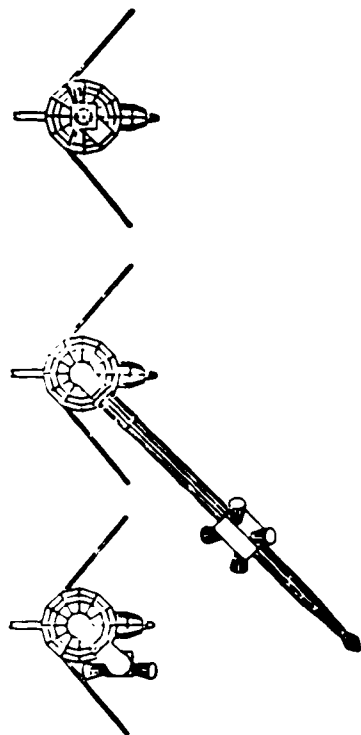


Figure 5-21. GRM-stowed Configuration

The structure is required to be sufficiently rigid to maintain the spacecraft centroid to within a 0.5 mm radius and a change of position at a rate less than 10^{-4} m/s orthogonal to the center line and 10^{-7} m/s along the center line. The mechanical characteristics of the S/C structure and boom are as follows:



<u>Element</u>	<u>Natural Frequency</u>
Structure	>10 Hz (lateral) >30 Hz (fore and aft)
Boom	>13.8 Hz (without loads of cameras and magnetometers) >9.9 Hz (loaded)

Figure 5-22. GRM A-1 Boom Deployment

The details of the boom and the loads are listed in Table 5-6. A tabulation of the estimated spacecraft weights is provided in Table 5-7.

5.8.2 LAUNCH CRADLE

Use of the Shuttle as a launch vehicle requires a cradle to support the spacecraft for both the normal launch and deployment operation and for an emergency landing. The cradle, shown in Figure 5-21, supports both spacecraft with a two-section arrangement. The first section is the primary cradle that has a keel fitting and four (two on each side) trunnion fittings. The second section is the cradle adapter that sets in the keyed slots of the primary cradle and supports the spacecraft through the strong rings as discussed in paragraph 5.7.1. The deployment sequence is shown in Figures 5-23 and 5-24.

Table 5-6
Boom Design Data

Load	Distance from S/C Body (m)	Mass (kg)
Boom	1.9	17.0
Star Cameras	1.9	28.0
Rigid Bench	2.3	4.5
Vector Magnetometer	3.1	0.54
Scalar Magnetometer	3.5	1.9

(Length: 3.8 m; diameter: 20.3 cm; and wall
thickness: 0.25 cm)

Table 5-7
GRM Estimated Weights

	A-1 Spacecraft (kg)	A-2 Spacecraft (kg)
Structure	672	514
Propulsion (dry)	260	260
Fuel	1400	1400
Subsystems	<u>402</u>	<u>343</u>
Total Weight	2734	2517

5.9 C&DH AND TDRSS TRACKING SUBSYSTEM

The Command and Data Handling (C&DH) system (Figure 5-25) for each spacecraft provides the means for ground operation (via the TDRSS) and onboard control of all spacecraft and instrument functions and for the retrieval of spacecraft housekeeping and instrument data. The communications subsystem for each spacecraft consists of redundant NASA standard transponders and conformal array antennas. Operation for the TDRSS requires two antennas located on the top of the spacecraft to maintain communications whether the GRM is approaching or receding from a particular Tracking Data Relay Satellite (TDRS). The antennas will also have an omnidirectional mode for emergency command. Command, telemetry, and tracking are then to be via the TDRSS S-band Single Access (SSA) link.

The 5 MHz oscillator feeding the 3.8112784 multiplier provides a separate 19.0564 MHz tracking signal that will operate via the S-band Multiple Access (MA) mode providing a one-way Doppler tracking capability. The early part of the mission requires quick-look orbit determination and tracking of orbital positions during the 160 km descent. Extensive use of this mode is anticipated.

Redundant data storage devices will be used on each spacecraft to record the science and housekeeping data. During the TDRSS ZOE and switchover from one TDRS to the other, the need for data storage is essential to the mission. The use of standard NASA tape recorders is planned for this function; however, the low bit rate may permit solid-state storage devices to be used. The data rates for each spacecraft are given in Table 5-8.

Table 5-8
GRM Data Rates

Spacecraft	Real	Playback	Time
A-1	4.6 kb/s	34 kb/s	12 min
A-1	2.6 kb/s	34 kb/s	7 min

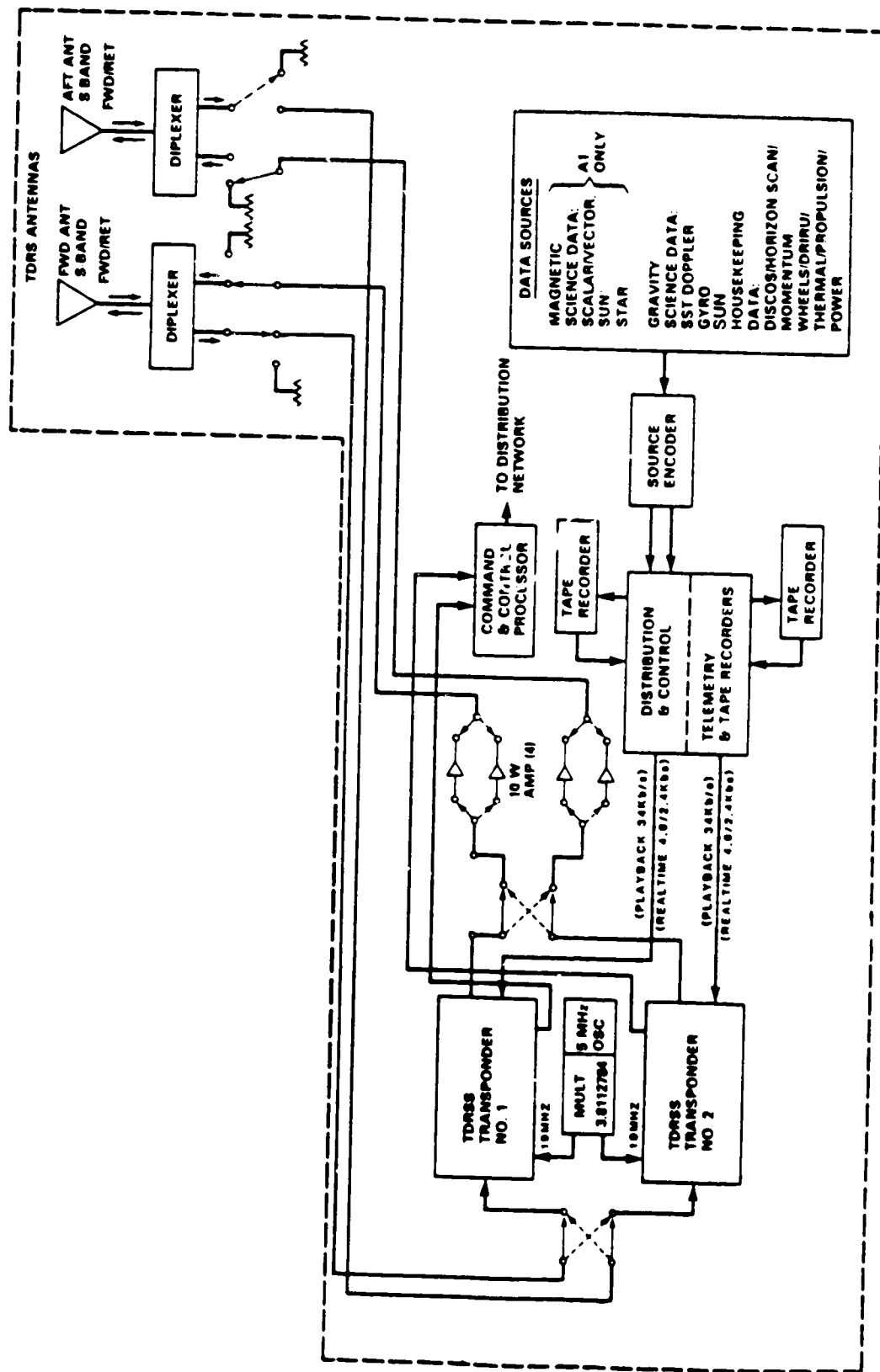


Figure 5-25. GRM Spacecraft: Telemetry/Command/Range and Range Rate Block Diagram

The link margin performance of both spacecraft and both the telemetry and one-way Doppler mode is listed in Table 5-9.

A command bit rate of a minimum of 125 b/s to a maximum of 1 kb/s is a modest requirement. Either the MA or SSA mode of the TDRSS can be used for the command link.

Table 5-9
GRM Link Margin Data

Spacecraft	Antenna Gain (dB)	Transmit Power (W)	Data Rate (kb/s)	Mode	Margin (dB)
A-1	7	10	34	TLM (SSA)	4.9
A-2	7	10	34	TLM (SSA)	7.7
A-1	7	10	4.6	TRK/TLM (MA)	3.8
A-2	7	10	4.6	TRK/TLM (MA)	6.3

5.10 DMA TRACKING SYSTEM

The block diagram of the subsystem is shown in Figure 5-26. The 150 and 400 MHz signals are generated from the stable 5 MHz reference oscillators. The performance of the system is listed in Table 5-10.

The antennas, which are circularly polarized, are of the type described in "Microstrip Antennas," IEEE Transactions on Antennas and Propagation, January 1975, Vol. A, pp. 23 and 90. A combined 150/400 MHz antenna will be mounted forward of the horizon sensor on the Earth-viewing side of the spacecraft.

Table 5-10
GRM/DMA Subsystem Characteristics

1. Beacon Frequency Stability	RMS Noise (σ)	Averaging Time (T)
Short-Term Stability	1×10^{-11} 6×10^{-12} 4×10^{-12}	1 sec 10 sec 100 sec
Systematic Drift	$+5 \times 10^{-10}/24$ hr after 72 hr warm-up	
Static Acceleration	$\pm 1.5 \times 10^{-9}$ g	
Magnetic Field	$\pm 1 \times 10^{-11}$ gauss	
Ambient Temperature	$\pm 5 \times 10^{-12}/^{\circ}\text{C}$	
2. Minimum Power Delivered to the Transmitting Antenna Terminal	150 MHz: -7.5 dBW 400 MHz: -6.0 dBW	
3. Antenna Gain	150 MHz: 4 dB minimum 400 MHz: 4 dB minimum	

5.11 ONBOARD DATA PROCESSING

Three data processing tasks are as follows:

- Monitoring and reporting the state of the spacecraft's subsystems (i.e., housekeeping data and command of the spacecraft)
- Monitoring and reporting the measurements made by the magnetometers and the SST and DISCOS systems
- Controlling the flight of the spacecraft, analogous to an aircraft autopilot to maintain the 160 km altitude drag-free orbit

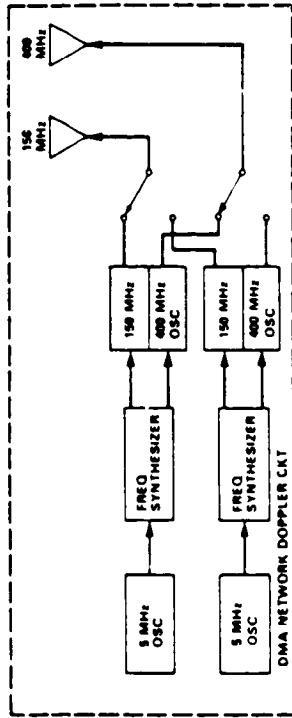


Figure 5-26. DMA Tracking Subsystem Block Diagram

5.11.1 HOUSEKEEPING AND COMMAND DATA

The related bit rate has been estimated as shown in Table 5-11. The storage requirement per orbit is 2.9 megabits.

For command of the spacecraft, it is necessary to have both Random-Access Memory (RAM) and Read Only Memory (ROM). An estimate of the GRM needs can be obtained from Magsat, which used a 64 bit command frame. The command processor was sized at 2048 bits (32 frames). The total Magsat implementation consisted of the RCA CDP 1802 microprocessor, CDP 1852 interface circuit, CDP 1822 1 K x 1 RAM, and HA 6611 256 x 4 programmable ROM. The total firmware for Magsat required 2.8 kilobytes of programmable ROM. This system covered all needs for Magsat, including the scientific instruments. For the GRM, a conservative sizing by a factor of 3 would require the performance of what is presently available in hand held calculators.

Table 5-11
GRM Housekeeping Data

Subsystem	A-1 Spacecraft (b/s)	A-2 Spacecraft (b/s)
Propulsion, DISCOS, and Attitude Control	110	110
Doppler SST	70	70
Instruments (A-1 only)	70	--
Command and Data Handling	50	50
Antenna System and Transponder	50	50
Power	60	60
Doppler Tracking	40	40
Thermal	<u>100</u>	<u>100</u>
Total	550	480

5.11.2 SCIENTIFIC DATA

The data rates for the magnetic data are as follows:

Vector Magnetometer	750 b/s
Scalar Magnetometer	165
Star Cameras	520
Sun Sensors	<u>260</u>
Total	1695 b/s

These requirements (1.695 kb/s) were easily handled by Magsat technology.

The gravity field measurement requires the determination of the output of the SST and the proof-mass position within the DISCOS cavity. The amount of data sampling and onboard processing are estimated as follows:

<u>Subsystem</u>	<u>Spacecraft (b/s)</u>
DISCOS	420
Flight Computer Output	480
Thruster Firings	72
Wheel Speed	32
Gyros and Horizon Sensors	64
Doppler SST	800
Total	<u>1868</u>

5.11.3 FLIGHT CONTROLLER

The most demanding onboard computer implementation is the flight controller or auto-pilot. The minimum inputs are:

- DISCOS axis position
- Thruster state (on/off)
- Fuel state (each tank)
- Spacecraft state (attitude as determined by horizon and sun sensors and the DRIRU)
- Spacecraft orbital position for estimation of expected cross winds

- Periodic updates of orbital state vectors for reestablishing the circular orbit and for set up and control of unique flight attitude and orbital position control.
- Reaction wheel state to anticipate and control momentum dumping

The requirements of the controller have not been determined. The TIROS-N type controller has been used as an estimate. It is expected that advancements in Personal Computer (PC) technology will show that the requirements are moderate. Recent (RCA model SCP-STAR) spaceflight computers are radiation hardened. The critical role of the onboard computer for guidance and control requires the use of either radiation hardened technology or redundant memories or both. The low orbital altitude with its resultant high atmospheric density presents a considerable hazard as loss of attitude control can result in catastrophic re-entry within a few orbits. Reliability of the onboard computer is a major design concern.

5.12 TOTAL SPACECRAFT \dot{s} ERROR

An error analysis of the ball-to-ball tracking is listed in Table 5-12. The data of Table 5-12 show that except for the ionosphere, an along-track error source ($\delta(\dot{x}) \cos \phi$) results in a DISCOS error of 10^{-7} m/s in pitch and yaw which dominate the total error.

In Table 5-12, each individual error is treated as an independent random variable giving a total Root Sum Squared (RSS) error of $0.4 \mu\text{m/s}$. Work performed by J. L. MacArthur, A. Finkel, and E. Westerfield (1981) shows that some of the individual sources of error, such as the mixer phase noise, are not white noise. It is not known if the harmonic content of the errors is correlatable with the harmonics of the spherical expansion model gravity field. The modeling of the above error sources including DISCOS-related \dot{s} correction capability is being continued to determine their effect on the gravity field measurement.

Table 5-12
Spacecraft-to-Spacecraft Velocity Errors

Source	Perturbation	Phase Noise (m/s)	Pitch (m/s)	Yaw (m/s)
Ionosphere	--	0.2×10^{-6}		
Mixer Noise	2×10^{-27}	3.0×10^{-9}		
Osc. and Mixer	1×10^{-12}	7.0×10^{-8}		
Ball not at Centroid	0.707×10^{-3} m		6.68×10^{-8}	1.73×10^{-8}
Static Mech. Offset	0.050 cm		9.5×10^{-8}	2.49×10^{-8}
Static Temp. Diff.	5°C		1.87×10^{-8}	4.9×10^{-9}
Y-axis Thrust				
(10 1/8 Hz)	5.7×10^{-8} m		1.06×10^{-11}	2.74×10^{-12}
Ant. Support Heat/Cool	0.14°C/s		1.4×10^{-9}	5.8×10^{-10}
Static Mech. Offset	0.050 cm		1.06×10^{-10}	1.14×10^{-11}
Main Thruster				
(30 1/8 Hz)	3.25×10^{-8} m		6.72×10^{-15}	7.28×10^{-16}
Ant. Support Osc.				
(30 1/8 Hz)	2.0×10^{-8} m		2.0×10^{-8}	2.0×10^{-8}
DISCOS: $\phi\delta(z) \cos\phi$	1.0×10^{-7} m		1.87×10^{-11}	4.9×10^{-12}
$\delta(z) \sin\phi$	1.0×10^{-7} m/s		1.12×10^{-14}	6.45×10^{-11}
$\phi\delta(x) \sin\phi$	1.0×10^{-7} m		2.09×10^{-14}	2.24×10^{-15}
$\delta(x) \cos$	1.0×10^{-7} m/s		1.0×10^{-7}	1.0×10^{-7}

Velocity Error (m/s) Summary (RSS)

Phase Noise (ionosphere):	0.2×10^{-6}	Yaw Axis (RSS total):	0.106×10^{-6}
Phase Noise (electronic):	0.07×10^{-6}	One Spacecraft (RSS total):	0.284×10^{-6}
Pitch Axis (RSS total):	0.156×10^{-6}	System (for RSS two spacecraft):	0.401×10^{-6}

SECTION 6. CRITICAL SUBSYSTEM DEVELOPMENT

6.1 SATELLITE-TO-SATELLITE TRACKING SYSTEM

6.1.1 COMPONENT TESTING

To demonstrate that the precision required range rate measurement can be realized, a breadboard system was assembled (MacArthur, Finkle, and Westerfield, 1981) embodying the major elements of the block diagram shown in Figure 5-3. The APL report No. SDO 6120, September 1981, describing the system and test program is summarized in the following discussion. The reference oscillators (item 1) are Frequency and Time Systems 1000 (FTS-1000). The xk multiplier chains (item 2) consist of two subsystems, an x20 multiplier of APL design, and a phased-locked Gunn oscillator supplied by Hughes Electron Dynamics Division (HEDD). The mixers (item 3) were also supplied by HEDD. The remaining systems (items 4, 5, and 6) are a combination of APL-built devices and commercial test equipment. Testing showed the following:

- a. Stability of the basic 5 MHz reference oscillators is not measurably degraded by the x18220 multiplication to 91.1 GHz. Fractional frequency deviation (Allan variance) measurements at 91.1 GHz (Figure 6-1) reveal instabilities of $<10^{-12}$ for averaging times above 1 second. The multiplier chains are in the compensated part of the two-way loop, with the result that a range rate noise of $<10^{-7}$ m/s is predicted for a 300 km spacecraft separation and 4 second averaging time.

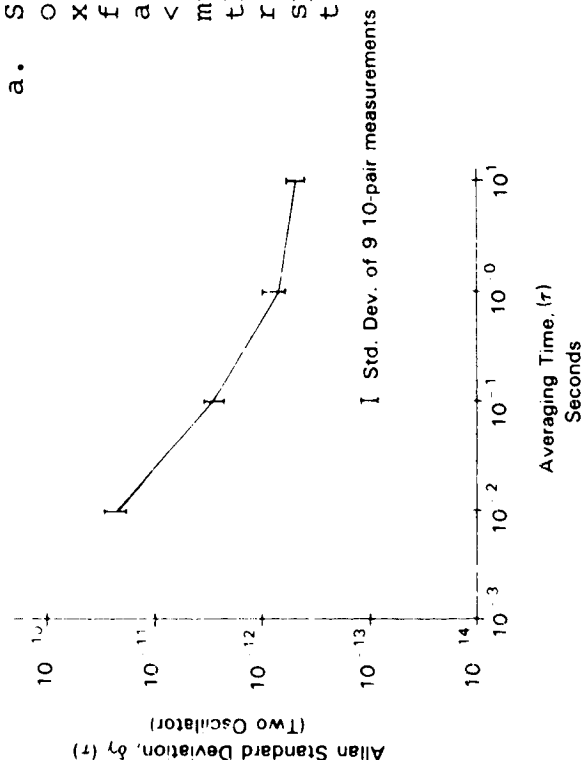


Figure 6-1. Frequency Stability at 91.1 GHz

- b. Measurement of the mixer contribution alone has shown a time delay jitter of 0.3 femtosecond ($1 \text{ femtosecond} = 10^{-15} \text{ seconds}$). The mixers are in the unsaturated part of the system for which no phase noise cancellation is realized. Accordingly, the predicted rate noise contribution from the two mixers is $1.6 \times 10^{-8} \text{ m/s}$. The temperature sensitivity of the mixers was also measured and found to be 0.3 deg/C . For an accuracy of $1 \mu\text{m/s}$, a temperature change rate of $<0.4^\circ \text{ C/s}$ is required. This is not a stringent condition to be met.

To verify the performance predicted from the foregoing measurements on individual components, two complete single-frequency systems were assembled to provide a system demonstration that included a phase noise cancellation simulation. To test the measurement capability, the systems were mounted on an optical bench with provisions for moving one system by a precision linear positioner (Figure 6-2). The movable

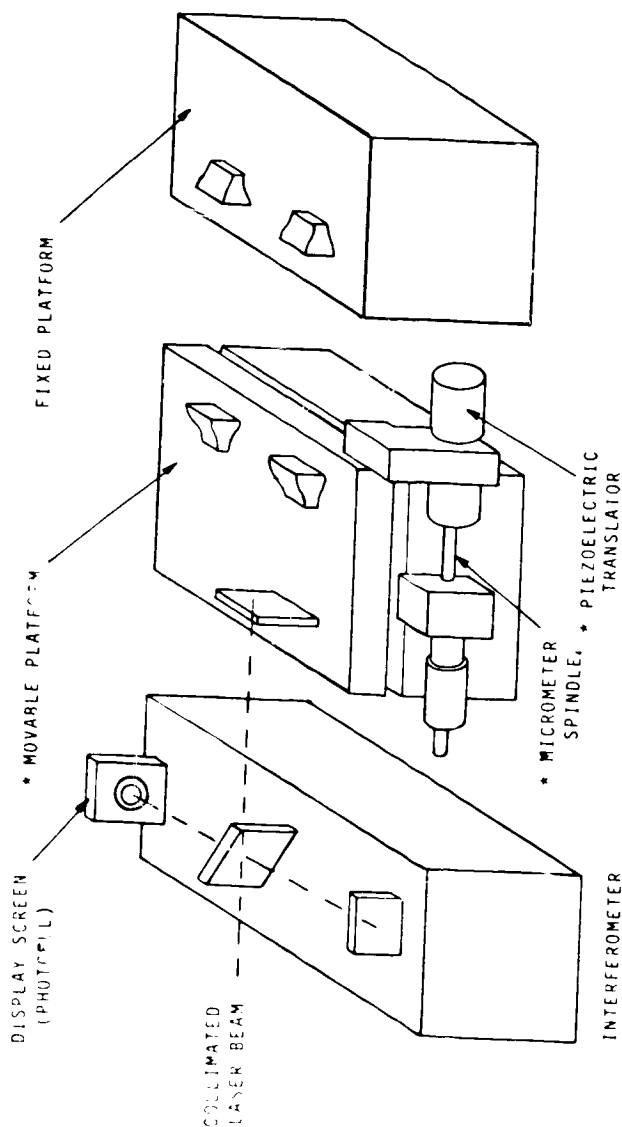


Figure 6-2. GRM Satellite-to-Satellite Tracking System (SST) Motion Experiment

platform was adjusted by a micrometer (for coarse motion) in series with a piezoelectric translator (for fine motion). A voltage of 0 to 1000 volts was applied to the piezoelectric transducer to produce a 0 to 40 μm movement. The transducer was nonlinear, exhibiting hysteresis, and was temperature dependent. A Michelson interferometer was used to independently track the moving platform. One mirror was attached to the moving platform. A pinhole and photocell provided a means for counting a fringe pattern light to dark transition and reflecting a half-wavelength (0.316 μm) platform motion.

The two RF systems were coupled via pairs of horn antennas. The setup allowed for separations of up to 1 foot. A 3/4 inch thick pine board was inserted between the antennas to add about 10 dB of path attenuation and to suppress multiple reflections between the antennas.

The initial system evaluation used the demonstration system shown in Figure 6-3. The relative phase of the two beat frequency output signals, S1 and S2, is a measure of range where a relative motion of the two systems of one-half wavelength at the frequency of 91.1 GHz results in 360 degrees of phase change. The phase delay, T, was measured in time interval counter along with the period of the beat of the optical tracker (S1 and S2). The sample time of the counter set the averaging time. Fringe transitions are accumulated in a separate counter to record platform motion.

Having first verified that the two systems (from front-end mixers to output signals (S1 and S2) have equal time delay, the nominal value of the phase delay, T, was set by a micrometer adjustment of the movable system to simulate an equal one-way range delay. In this way, the zero crossings of S1 and S2 were influenced by oscillator noise at sample times separated by T, and this resulted in the same decorrelation and increased range rate noise that results from propagation delay. To simulate a 300 km spacecraft separation, T was set to 10^{-3} s.

Data were collected with the two systems stationary to evaluate the system noise level. An example of the results for simulated ranges of 15 to 300 km is given in Figure 6-4. A projection based on the Allan variance data of Figure 6-1 is also included for comparison. A noise level close to 10^{-7} m/s for 300 km and 4 second averaging was realized. This level exceeds by almost a factor of 10 the mission accuracy requirement of 1 $\mu\text{m/s}$. The performance floor imposed by mixer noise is also shown. The 15 km results should be a factor of 20 below the noise at 300 km. This is true at the shorter averaging times, but above 10 seconds, mixer noise begins to dominate.

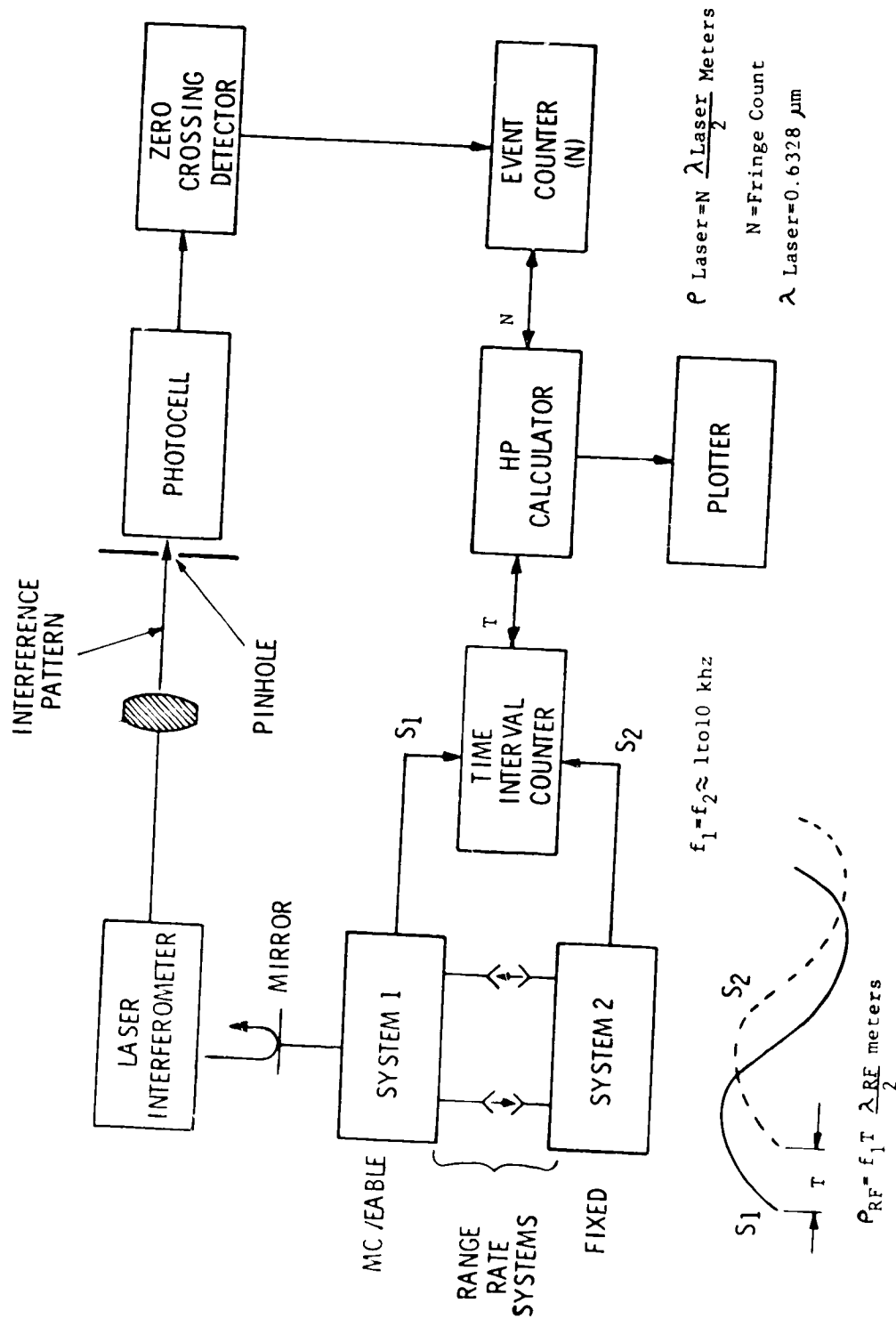


Figure 6-3. SST Demonstration System

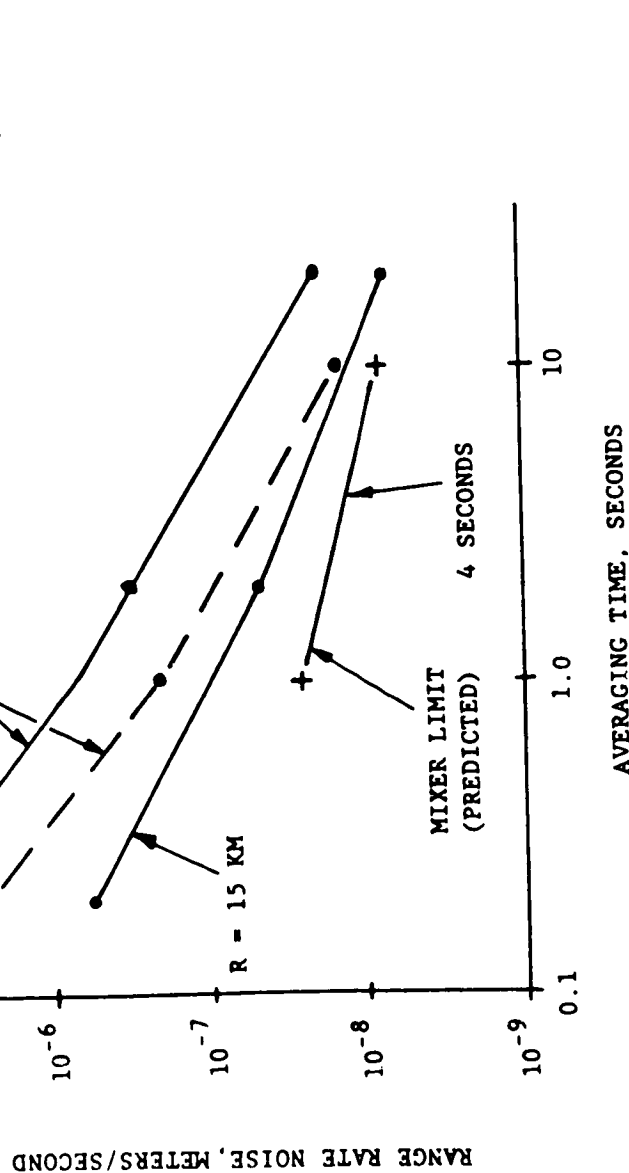
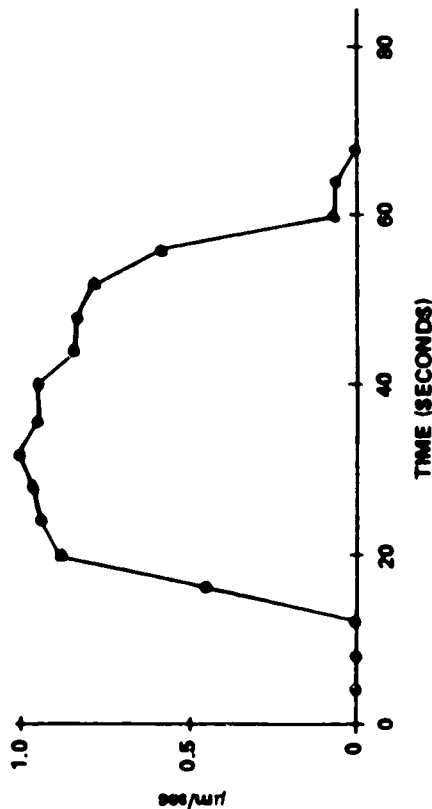


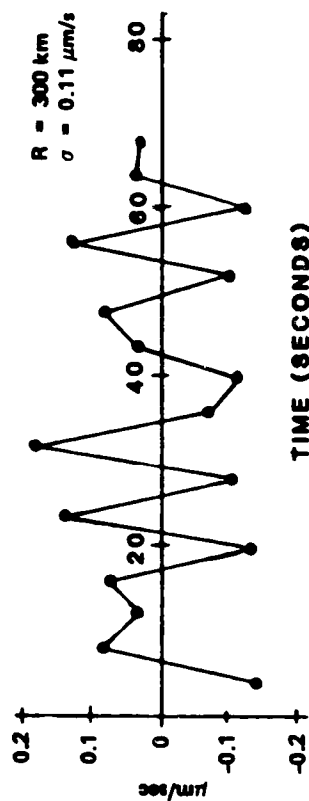
Figure 6-4. SST Measurement Noise Versus Averaging Time

The SST system performance was demonstrated by applying a ramp voltage to the piezoelectric transducer to cause the movable platform to translate at a nominally uniform rate. Figure 6-5A shows the system response to a $1 \mu\text{m}/\text{sec}$ ramp. The ramp lasts for approximately 40 seconds. Transducer nonlinearities account for the general profile of the indicated range rate that is computed as the difference between successive range measurements divided by the interval (e.g., 4 seconds). The 300 km range simulation is shown in Figure 6-5B. After time alignment (to account for a 1 second sample time difference), the residuals between interferometer and the RF system were determined and are then plotted for the 300 km separation range. The RMS of the residuals does not differ significantly from the static noise data shown in Figure 6-5B.



A. INTERFEROMETER READOUT FOR 40 $\mu\text{m}/40$ SEC RAMP

NOTE: EACH FRINGE COUNT
IS EQUAL TO 0.316 m
IN RANGE OR 0.079 m/s
WITH 4-SECOND SAMPLING



B. RANGE RATE RESIDUALS FOR SIMULATED RANGE

Figure 6-5. Rate Noise During a Constant Velocity Ramp

6.2 GUIDANCE AND CONTROL SIMULATION

Since 1981, a number of simulations and modeling of the DISCOS/guidance and control/propulsion systems have been run at both APL and GSFC. The modeling and simulation conducted by APL in 1981 and reported in the JHU/APL report SDO 6179, September 1981, are summarized in the following discussion.

Figure 6-6 is a functional block diagram of the GRM G&CS. In the actual spacecraft, each element (represented by a box shown in Figure 6-6) is a physical entity that behaves according to applicable laws. In the simulation, a set of equations mathematically models the behavior of each element. Utilization of a digital computer program provides the combined solution of the equations (models) of the system elements. Essential features of the important models used in the G&CS simulation are described in the following paragraphs.

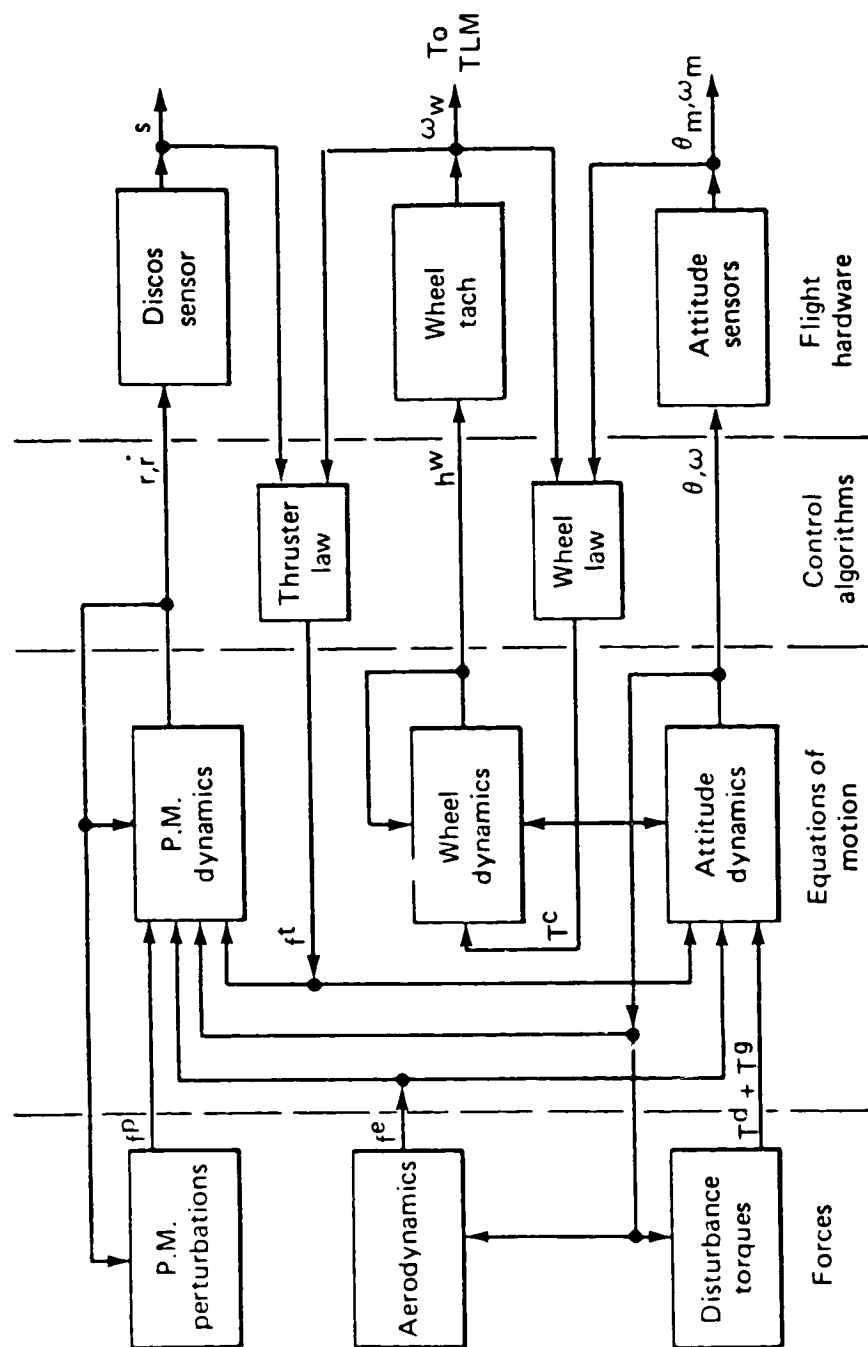


Figure 6-6. GRM Guidance and Control System Functional Block Diagram

6.2.1 EQUATIONS OF MOTION

Referring to Figure 6-7, the general equations (Ray and Jenkins, 1981) for proof-mass position, spacecraft angular velocity, and reaction wheel angular momentum are:

$$\ddot{\mathbf{r}} = -(\mathbf{f}_e + \mathbf{f}_t) - \nabla g(\mathbf{r} + \mathbf{d}) - \mathbf{f}_k(\mathbf{r} + \mathbf{d}) - \ddot{\mathbf{a}} + (1 + m/M)\mathbf{f}_p$$

$$\dot{\boldsymbol{\omega}} = \mathbf{I}^{-1} [-\boldsymbol{\omega} \times (\mathbf{I} \boldsymbol{\omega} + \mathbf{h}^w) - \dot{\mathbf{h}}^w + \mathbf{T}\mathbf{d} + \mathbf{T}\mathbf{g} + \ell_1 \times M\mathbf{f}_e + \ell_2 \times M\mathbf{f}_t]$$

$$\dot{\mathbf{h}}^w = \mathbf{T}^c - \boldsymbol{\omega} \times \mathbf{h}^w$$

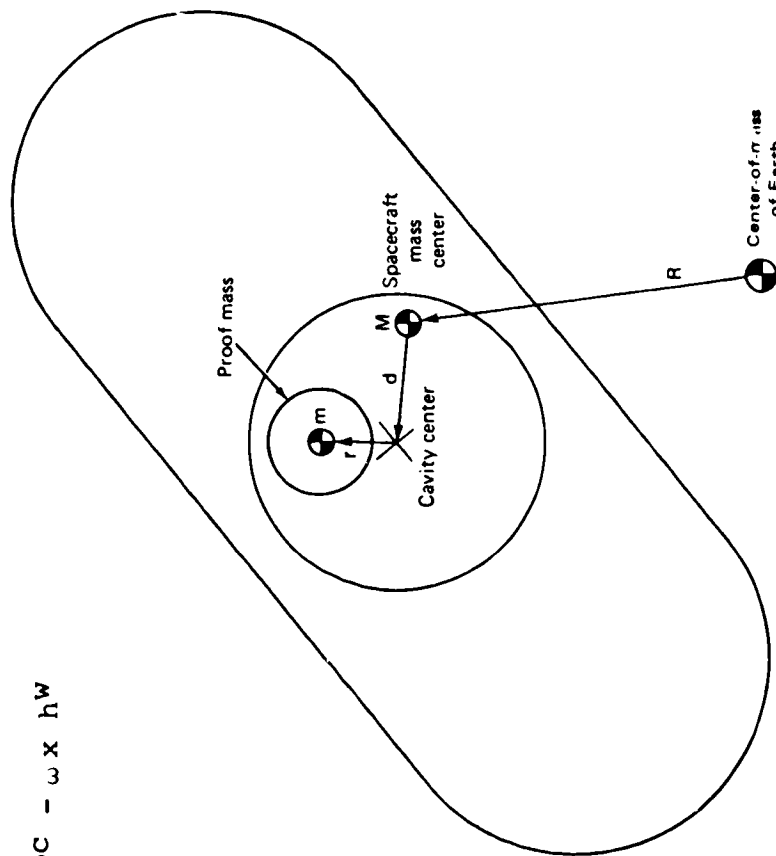


Figure 6-7. Notation for General Dynamic Equations

In these equations, the variables are generally three-component vectors unless otherwise noted. The vectors are expressed in a spacecraft body-fixed reference frame.

r = position of proof mass with respect to cavity
 f_e, f_t, f_p = specific forces (force per unit mass) due to external forces, thrusters, and proof-mass perturbations
 $\nabla g(r)$ = specific force due to difference in Earth's gravity between two points separated by r . Note: ∇ is a differential notation and not a "Del" operator, and g is a functional notation not a symbol for gravity.
 $f^k(r)$ = apparent kinematic specific force due to angular velocity of reference frame: $f^k(r) = \dot{\omega} r + \omega \times (\omega r) + 2 \omega \dot{x} r$
 d = displacement of DISCOS sensor from spacecraft mass center
 (m, M) = mass of (proof mass, spacecraft); m, M are scalar values
 ω = spacecraft angular velocity
 I = spacecraft inertia Tensor (3 x 3 matrix)
 $h \omega$ = vector sum of angular moments of reaction wheels
 T_d, T_g = disturbance torques due to drag and gravity gradient
 ℓ_1, ℓ_2 = vectors from spacecraft mass center to point of application of aerodynamic and thruster forces
 T_C = torque applied to reaction wheels (control torque)

In addition to the foregoing equations, a kinematic differential equation relating spacecraft attitude and angular velocity is required to completely model the motion. Euler parameters (quaternions) are used computationally in the G&CS simulation. These parameters are converted to standard Euler angles (pitch, roll, and yaw) for display.

Note that the model for equations of motion is a set of ordinary differential equations that must be solved by numerical integration. The GRM G&CS simulation primarily uses standard fourth-order Runge-Kutta integration.

One of the inputs to the simulation model (Figure 6-6) is the aerodynamic forces. Modeling of these forces was performed in 1981 and has recently (July 1984) been updated. The outputs of the model provide both force and torque data applicable to all three axes of the spacecraft.

As seen in Figure 6-6, input/output models are needed for the DISCOS sensor, thrusters, reaction wheels, and attitude sensors (gyros and horizon sensor).

The DISCOS sensor measures proof-mass position relative to the cavity coordinate axes. Because the sensor is based on capacitance between the proof mass (ball) and cavity, its measured output is a nonlinear function of true ball position. An example of this nonlinearity for the X axis is shown in Figure 6-8.

The model (Ray and Jenkins, 1981) implemented in the simulation is

$$x_m = K_{11}x[1 + x^2/w_1^2 + K_{21}(y^2 + z^2)]$$

$$y_m = K_{12}y[1 + y^2/w_2^2 + K_{22}(x^2 + z^2)]$$

$$z_m = K_{13}z[1 + z^2/w_3^2 + K_{23}(x^2 + y^2)]$$

where x , y , and z are true ball coordinates, x_m , y_m , and z_m are measured coordinates, and the K 's and w 's are model parameters. The modeled "measured" ball coordinates are used as inputs to the control and estimation algorithms implemented in the guidance and control simulation.

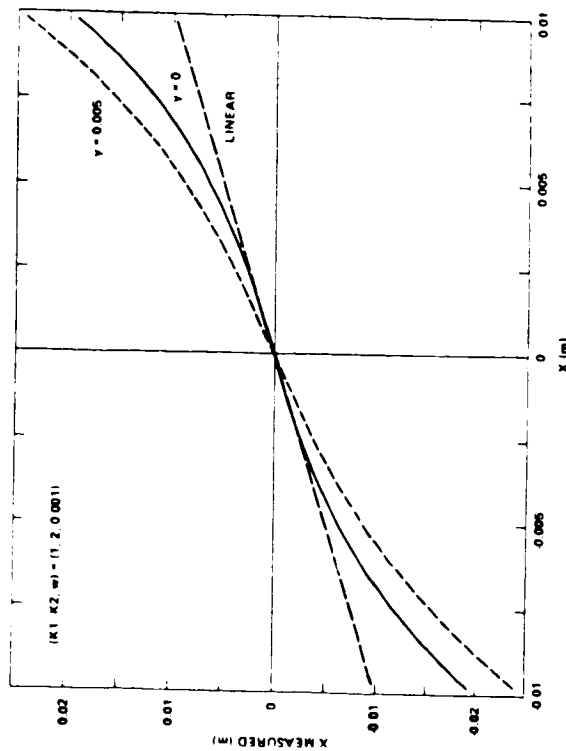


Figure 6-8. DISCOS Sensor Model

6.2.2 CONTROL LAWS

A central feature of the G&CS consists of the algorithms programmed in the flight computer to control the thrusters and reaction wheels. An important use to date of the simulation has been in preliminary development of these control laws. The objective of the thruster control laws is to maintain proof-mass position and stored reaction wheel momentum within required limits while minimizing fuel consumption. In addition,

there are constraints on the thruster control laws arising from the needs to complement the science data and to obtain maximum reliability of the propulsion system.

Minimizing mission fuel consumption is equivalent to never firing a thruster except to compensate for the drag force. Thruster firings to center the ball in the crosstrack direction, to dump angular momentum, or to apply reverse thrust will increase fuel consumption. In these instances, a control law to minimize such waste is feasible provided the value of the drag force is available for the algorithm. Therefore, the thruster control laws will have to be adaptive at least in the sense that the continuously changing drag force is estimated and utilized. The necessity of real-time flight control independent of ground control requires an onboard flight computer.

It is important that the thruster control laws be designed with the GRM science mission in mind. Dual use of the DISCOS sensor for spacecraft control and for science data requires reconstruction of the ball velocity relative to the DISCOS cavity. Motion caused by thruster firings will directly corrupt (equation 5-4; $s_t = \dot{s} + \delta x_1 + \delta x_2$) the science data unless it is determined to a $0.1 \mu\text{m/s}$ accuracy. The frequency and amplitude of the drag compensation limit cycle will be chosen to provide the accuracy required for postflight ball-velocity reconstruction. As an example, if hardware constraints prevent the control limit cycle frequency from being set outside the bandwidth of primary interest for geophysics, the limit cycle must be precisely repeatable to facilitate filtering it out of the relative velocity data. Also, it may be desirable to choose a small limit cycle amplitude to stay near the linear range of the sensor.

Another factor complicating the control law design is attitude/translation coupling. Attitude affects the translational dynamics of the proof mass both through aerodynamic forces and by kinematic pseudo-forces (e.g., centrifugal and Coriolis). The proof-mass translation affects the attitude since firing the thrusters will, in general, produce a torque and a translational force. This coupling is inherent, and it is necessary that it be considered.

The thrusters must be governed by an on/off control law, and in the presence of a substantial acceleration due to the drag force, the desired steady-state condition is a sequence of relatively short firing pulses and relatively long coast arcs. A phase-plane diagram of this limit cycle is shown in Figure 6-9. The phase-plane trajectories are parabolas for both firing and coasting arcs when the net force (thrust plus drag) is constant over any arc.

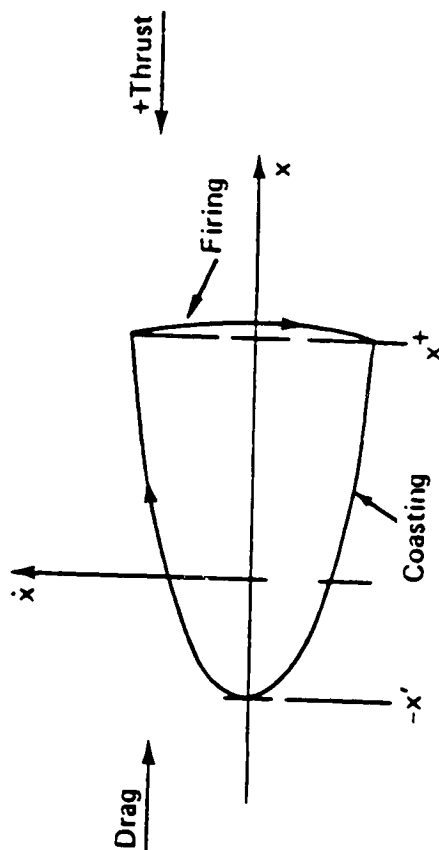


Figure 6-9. Desired In-track Limit Cycle

The control law design begins with the choice of the limit cycle parameters x' and x^+ , necessitating some compromise. For maximum sensor accuracy, the excursion of the ball from center should be as small as possible. A small amplitude ($x' + x^+$) limit cycle requires a high firing rate, that would affect thruster reliability. Given the thrusters and other spacecraft characteristics, the smallest value of ($x' + x^+$) that has been evaluated is about +1 mm, -0.5 mm, yielding a cycle time of approximately 15 seconds.

Using the position limits of $x^+ = 1$ mm and $x' = 0.5$ mm as well as the velocity and position limits shown in the phase plane of Figure 6-10, simulations of the guidance and control were run.

In the cross-track directions, the drag component is much smaller than the in-track drag and it is not as consistently predictable as the in-track drag. The control law that has been derived from the crosstrack thrusters is shown in Figure 6-11. The control law stops any outbound proof-mass motion at a specified deadzone boundary (currently +1 mm) and imparts a small inward velocity proportional to the proof-mass position beyond the deadzone boundary. This gives rise to the switching lines shown in Figure 6-11. The curved lines are the trajectories with thrusters on, whereas the

straight lines represent the position-proportional inward velocity concept.

The control law axes are:

- 1- vertical or yaw
- 2- direction of flight or roll
- 3- horizontal or pitch

The behavior of the cross-track control law is shown in Figure 6-12 which is a 1-direction vertical phase plane. This case was initialized at ($x_1 = -2$ mm, $\dot{x}_1 = 0$) that resulted in the desired inward velocity (about 0.1 mm/s). With very little drag in the 1-direction, the proof-mass coasted across to the other deadzone boundary where the control law effectively stopped it. Small perturbations (in this case, attitude coupling and Coriolis force) start it drifting back toward the $-x_1$ deadzone. The scalloped appearance is the effect of Coriolis-induced coupling from the in-track limit cycling.

A time history of the proof-mass motion on all three axes, for the same case as Figure 6-12, is shown in Figure 6-13. It is seen that, even starting from grossly perturbed initial conditions, the in-track (2-direction) limit cycle is quickly established and stable. The 1-axis (vertical) is seen to have a drifting character after being captured in the deadzone. The 3-axis shows much perturbations which is due to the slower response of the satellite yaw control that results in a relatively large drag

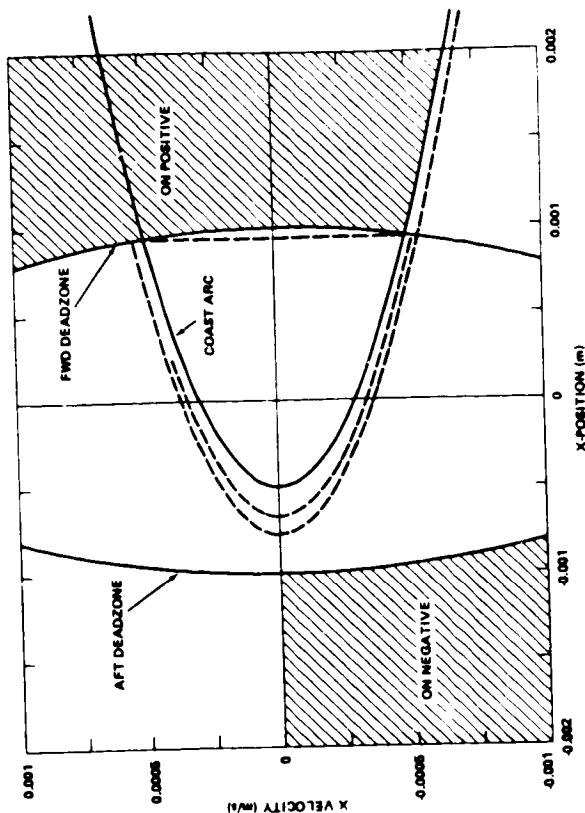


Figure 6-10. In-track Thruster Control Law

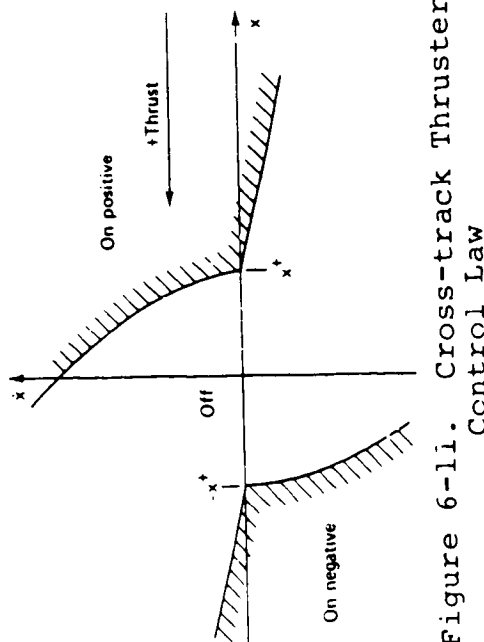


Figure 6-11. Cross-track Thruster Control Law

projection onto this body axis until the attitude is stabilized. The 3-axis perturbation illustrates the importance of attitude-translation coupling in the overall G&CS analysis.

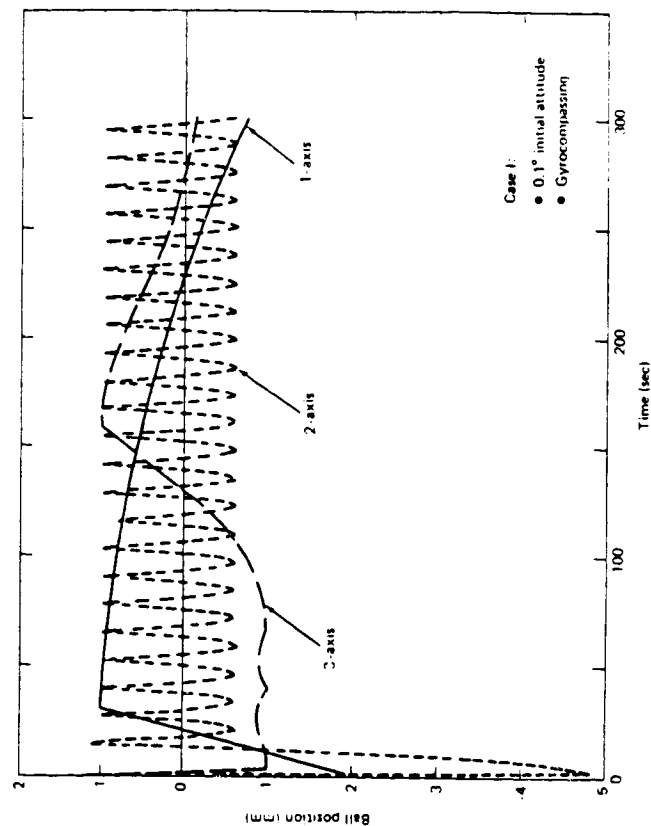


Figure 6-12. Proof-mass 1-Axis Phase Plane

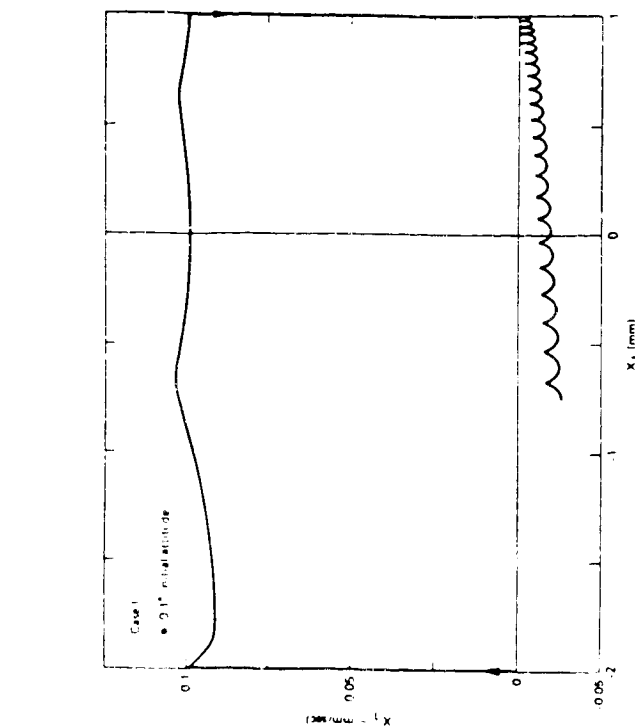


Figure 6-13. Proof-mass Coordinate History (Without BCA)

Because the control laws used for the simulations shown in Figures 6-12 and 6-13 force the expenditure of fuel to correct for cross-track drift, a scheme to pitch the spacecraft off the in-track velocity vector was examined. The results of the Ball-Centering Angle (BCA) simulation are shown in Figure 6-14. In this case, cross-track thrusters did not fire; therefore, fuel consumption was minimized.

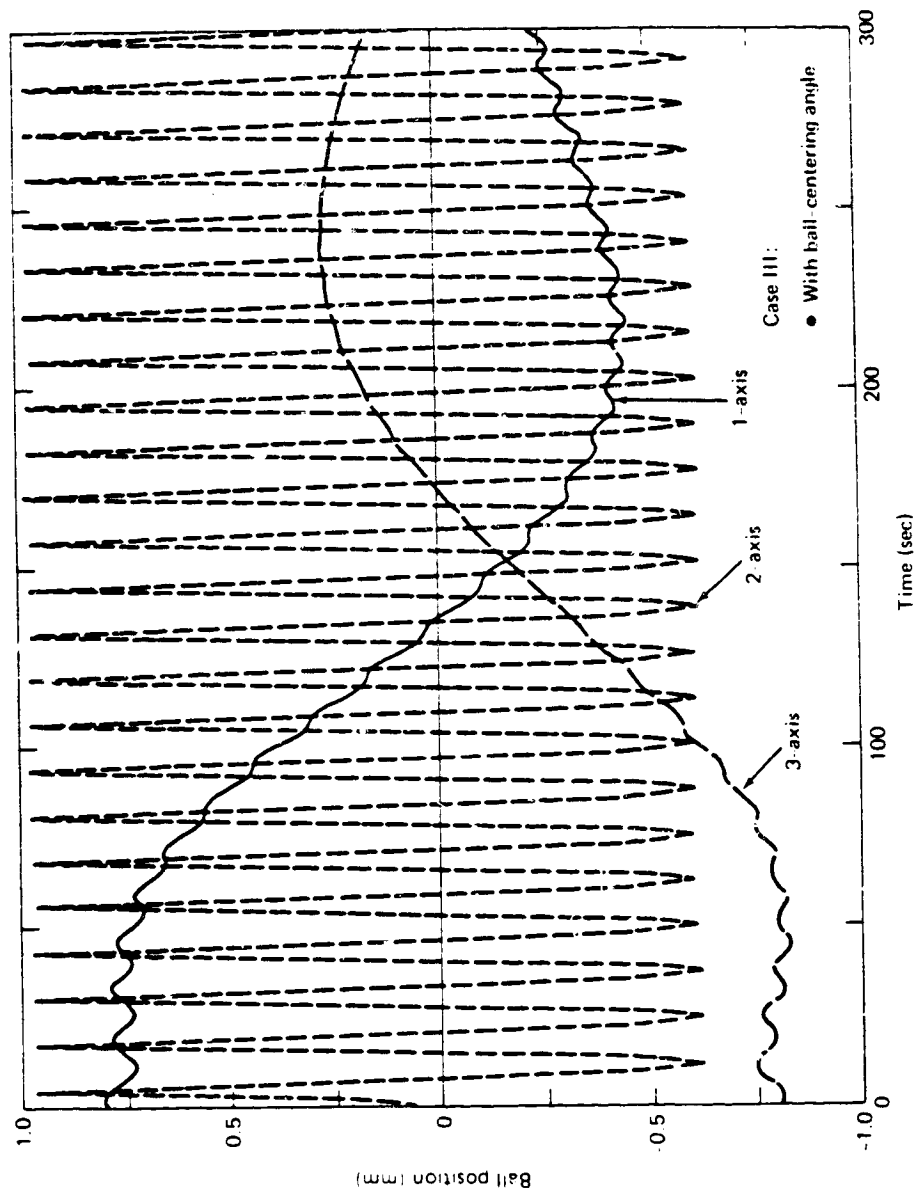


Figure 6-14. Proof-mass Coordinate History (With BCA)

6.3 GUIDANCE AND CONTROL SUBSYSTEM

The G&CS includes much more than the DISCOS and thruster control system.

6.3.1 ATTITUDE CONTROL CONFIGURATION

To meet the performance requirements, an inertial reference (gyro) unit, such as the DRIRU, is the basic control sensor. A radiation balance Earth sensor (Tiros-N Earth sensor) supplies the vertical axis reference for the DRIRU; digital solar aspect sensors provide third axis (yaw) reference as well as attitude sensing for initial acquisition and attitude determination.

The torque actuators will be NASA standard reaction wheels that have 20 N-m-s capacity and torque output to 0.15 N-m (for momentum less than 10 N-m-s). Four wheels, geometrically arranged in a tetrahedral configuration will provide redundancy and improved performance. Hydrazine thrusters provide 3 axis torques to maintain stored momentum and auxiliary control torque for pointing acquisition and backup, in case of wheel failure or overload.

6.3.2 ONBOARD COMPUTER

The G&CS digital Onboard Computer (OBC) implements the control laws that provide stability, calibration (of the DRIRU drift compensation), momentum control, and attitude determination. The OBC will provide for minimum fuel consumption by considering interactions of spacecraft attitude and proof-mass position in the control laws.

6.4 PROOF MASS ROUNDNESS AND CENTER OF MASS

The DISCOS system accuracy is dependent upon the roundness of the ball and the center of mass of the ball.

6.4.1 BALL ROUNDNESS

Stanford University has stated (DeBra, March 1981, Monthly Report) that the ball surface deviations can be modeled as spherical harmonics, analogous to the usual description of the figure of the Earth. Stanford has measured (DeBra, May 1981, Monthly Report) the roundness spectrum of five balls, representative of the size for

the GRM proof-mass but ranging widely in quality. A typical spectrum is shown in Figure 6-15. The amplitude of deviation from spherical of the n th harmonic is seen to vary as n^{-1} for n less than about 10 and to fall off even more rapidly for n greater than 10. Assuming for the moment that the sensor measures the distance between the housing and the two points on the ball, as shown in Figure 6-16, then the position output error is

$$\delta x = \delta R_n \sin n\omega t \quad (6-1)$$

where R_n is the amplitude of the n th harmonic and ω is the ball spin rate. Thus, the velocity error is

$$\delta v = \omega (n \delta R_n) \cos n\omega t \quad (6-2)$$

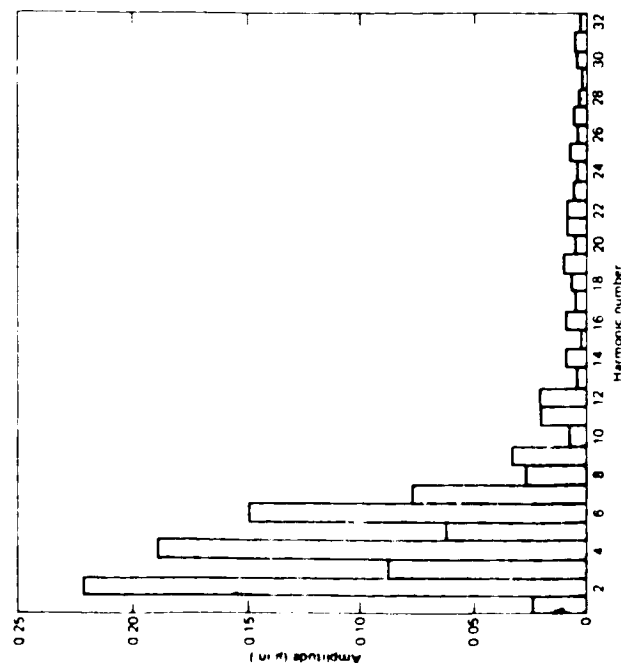


Figure 6-15. Harmonic Analysis of Roundness Errors--Typical Proof-mass

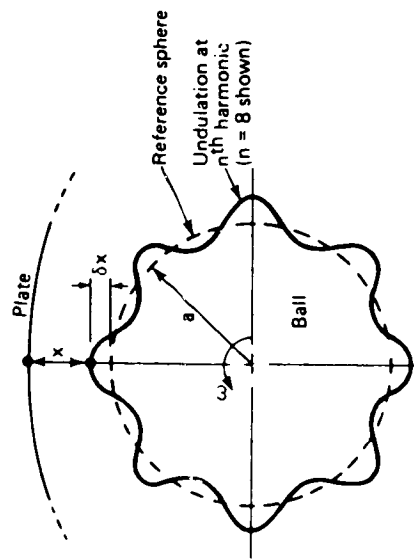


Figure 6-16. DISCOS Error Due to Proof-mass Roundness Errors

It is clear that if δR_n falls off as n^{-1} or faster (with n greater than 10), there is no increase in sensitivity to ball spin for the higher harmonics. In the actual sensor, the plates will measure the average contribution of the higher harmonics rather than the point measurement modeled in Figure 6-16. Stanford has concluded that harmonics above the 5th or 6th can be ignored.

All the roundness measurement data are below the line $N\delta R_n = 0.2 \mu\text{m}$, so that for spin rates of $\omega < 0.5 \text{ rad/sec}$ (≈ 500 times orbital rate), the velocity error will be less than $0.1 \mu\text{m/s}$ because of ball roundness. The Relativity Gyro Program of Stanford University has made and measured the roundness of balls at least an order of magnitude better than those previously discussed. Although the proof mass will need to be made with care, acceptable roundness is well within the state-of-the-art.

6.4.2 BALL MASS CENTER OFFSET

The measurements of ball roundness were made with respect to a reference sphere, which is defined as the best fit to the surface. Thus, the first harmonic that represents the deviation of the center of the reference sphere from the center of spin (i.e., the mass center) is subtracted out of the data. This first harmonic once-around term or mass center offset) must be separately measured.

Present mass center offset measurement techniques involve flotation of the ball and measurement of the pendulous frequency. Since small mass center offsets produce very long pendulous periods, it is difficult to sustain oscillation long enough to measure a very small offset. The flotation technique is an accuracy limited to about $3 \mu\text{m}$, or about one to two orders of magnitude larger than the state-of-the-art in measuring the ball surface roundness. The state-of-the-art of CM measurement metrology is sufficient for successful GRM performance. Since limitations of the metrology burden the GRM data reduction, it is planned to pursue techniques that may yield a more precise determination of the CM.

If advanced CM measurement techniques cannot be developed, an alternative to measuring and removing (by machining) the CM offset from the ball is to identify its effect from the data in flight and to remove the effect by data processing. Since the offset only affects the data proportional to the ball spin, which will probably be essentially undamped if it exists, the CM offset effect can be identified as an undamped oscillation of constant frequency in the data. A narrow-band digital filter can then be used to remove its effect. This approach should be regarded as a last resort since

some compromise of scientific data will result if the spin rate is within the data bandwidth. The degree of difficulty of the data processing has not been determined.

Another alternative is to avoid the effect of CM offset by preventing ball spin at frequencies in the science bandwidth. This alternative requires that the spin be kept either very slow (essentially damped) or maintained at a sufficiently high rate (>0.5 rad/sec). Either alternative will require torque on the ball, which should be avoided if possible, since forces will inevitably result from the torque generation mechanism. It is feasible to develop spin damping or spin-up systems with acceptably small force perturbations on the ball, but this design complexity should and can be avoided, if the ball mass center offset can be made sufficiently small.

6.5 MASS ATTRACTION

Each spacecraft contains a pair of 700 kg hydrazine fuel tanks. This massive amount of fuel affects both the centroid of the spacecraft and the point of zero mass attraction within the spacecraft. When the forward tank has more fuel than the aft tank, the proof-mass is pulled forward toward the DISCOS cavity wall. This movement looks the same as atmospheric drag to the DISCOS. The propulsion system is commanded to activate the rear thrusters providing a delta velocity that is detected by the SST. The signal is processed as if it were measuring a response to a gravity anomaly that had accelerated the spacecraft toward a higher orbit. This action generates an error signal. If the frequency of the thruster firing, to compensate for the attraction imbalance, is within the spacecraft response to a gravitational anomaly, the centroid signal cannot be filtered out. To minimize the mass attraction and the centroid imbalance, the fuel tanks have metal diaphragms that continuously hold the fuel in a controlled position. As the fuel is consumed, the external gas pressure source maintains a minimum pressure of 2 MPa (300 psi) against the diaphragm, which keeps the fuel cavity full (prevents sloshing). The maximum tank-to-tank fuel imbalance will be 10 kg. The acceleration from a 10 kg imbalance is shown in Figure 6-17.

The spacecraft drag acceleration is approximately $6 \times 10^{-5} \text{ m/s}^2$. The worst-case mass attraction acceleration shown in Figure 6-17 is $6.7 \times 10^{-10} \text{ m/s}^2$, which is much less than the drag acceleration. For the $6.7 \times 10^{-10} \text{ m/s}^2$ acceleration, the time required for the proof-mass to move 1 mm (out of the null zone) is 1732 seconds. This is about one third of the orbit and is beyond the longest gravity wavelength (10,000 km) that is to be detected per the mission requirements.

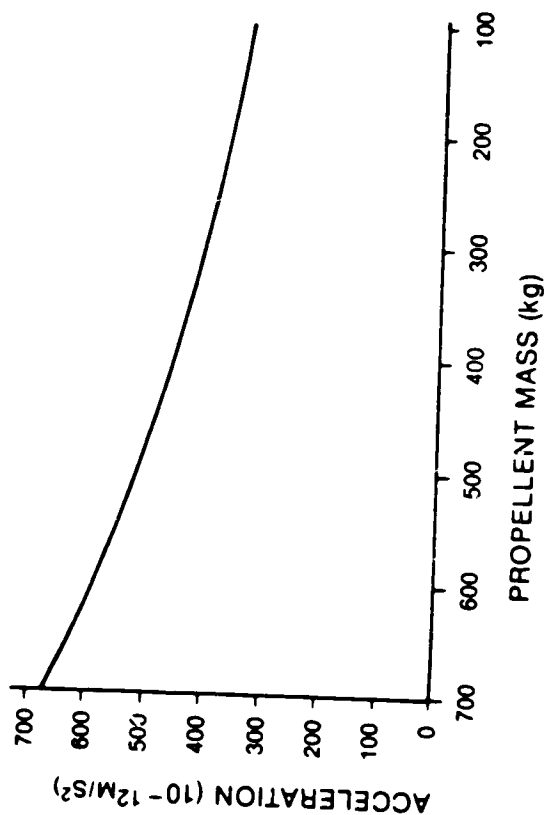


Figure 6-17. Acceleration Due to a 10 Kg Mass of Fuel Imbalance

6.5 CRITICAL DESIGN

The critical areas of the mission and those needing constant attention and resolution are described in the following paragraphs.

6.6.1 DISCOS PERFORMANCE

The present system design requires that the proof-mass velocity be determined with respect to the cavity center (δ) and used to correct the SST measured δ . This design relies upon the ability to precisely calibrate the instrument (prior to flight) and the instrument's stability throughout the mission. The DISCOS plays a critical role in providing data inputs to the gravity field determination. The heritage from the successful TRIAD DISCOS mission provides confidence in the present design.

Two alternate designs are being considered to increase the probability of mission success. These designs are:

- a. on-board calibration of the proof-mass position,
- b. an alternate design that is defined as the two-stage DISCOS (Figure 6-18)

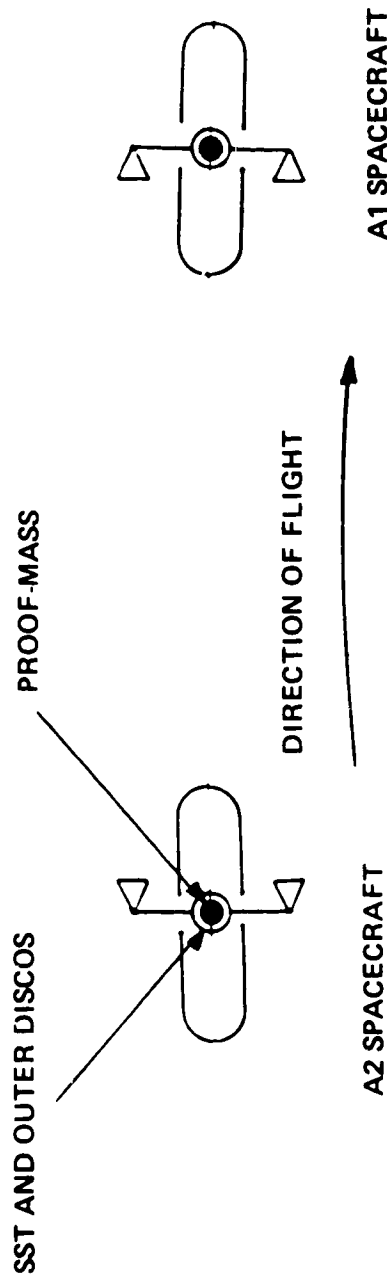


Figure 6-18. Two-stage DISCOS

6.6.1.1 ON-BOARD CALIBRATION

On-board calibration is an augmentation of the existing design. The major design feature incorporates an optical (laser source) cage that surrounds the proof-mass. Proof-mass position would be determined by the interruption of the light beams. These points of interruption would be compared to the preflight calibration data and corrections to the data would then be made.

6.6.1.2 TWO-STAGE DISCOS

This alternative isolates the DISCOS instrument and the SST system from the spacecraft body. The isolation of the SST/DISCOS platform from the spacecraft structure is accomplished by magnetically suspending the platform in a manner analogous to a solenoid in a magnetic field. The SST/DISCOS platform is surrounded by the spacecraft and except for the antenna, it is shielded from all external forces except gravity.

Since the drag forces and thruster firing are absorbed in the space between the SST/DISCOS platform and the spacecraft body, the off-center movement of the proof-mass (the second stage of the two-stage DISCOS) within its cavity is minimal.

The resultant advantage of this design would be to obtain a direct proof-mass to proof-mass range rate (\dot{s}) measurement eliminating the data corrupting movement present in the existing design.

A feasibility study of this alternate design is being done by APL and will be completed in the summer of 1986.

6.6.2 SATELLITE-TO-SATELLITE TRACKING SYSTEM

Although a major accomplishment was made by the successful laboratory test program, the minimum critical features of this system include the following:

- a. Stability of the mixers and their long-term drift characteristics. Determining if the drift is correlatable to the harmonics of the gravitational field.
- b. Design and analysis of the counter system that detects and measures the Doppler signal.
- c. A two-frequency system design, and the analysis of the ionospheric correction capability.
- d. A need to qualify the parts and components.

6.6.3 ATMOSPHERIC DRAG AND FUEL CONSUMPTION

The flight attitude, essentially in the direction of the axis of a cylinder, requires a need to know the total drag force associated with the lateral surfaces of the cylinder and the flat surfaces (edge on flight attitude) of the solar panels. The present fuel supply (1400 kg) is based upon allowing for considerable lateral surface drag which is a function of the surface tangential accommodation coefficient. Test data for grazing angles near 85 degrees have recently been obtained.

A test program currently being performed at GSFC by Dr. F. Herrero has provided some test data for momentum transfer. These data can be used to obtain drag force due to grazing angle collisions of the atmospheric molecules with satellite surfaces. The data are then used to obtain lateral surface drag coefficients arising from grazing angle impacts between 80 and 85 degrees (Herrero and Cagiano, 1985). This coefficient determines the drag force due to the solar panels and the lateral surface of the main body of the spacecraft.

These new angular data, obtained from using an ion beam that has a narrow energy distribution and a detector with a narrow (5 deg) field of view, provides new insight for understanding the gas to surface interaction. Figure 6-19 shows the reflected lobe structure for a set of impact energies. It is highly significant that the angle of the reflected lobe increases proportional to the impact energy. Figure 6-20 provides data for two additional configurations and in particular, Figure 6-20(b) represents the condition that approximates the GRM flight parameters (8 to 15 eV and $\theta_i = 85^\circ$).

The type of test data shown in Figures 6-19 and 6-20 was used to generate the curves shown in Figure 6-21 that shows the variation of the lobe angle θ fm with ion energy. Using the data that are represented in Figures 6-19, 6-20, and 6-21, it is possible to obtain a value for the fractional momentum transfer, $F(\theta)$, that is related to the more commonly known normal and tangential accommodation coefficients by the equation Herrero, 1983)

$$F(\theta) = (1 - \alpha_n) \cos^2(\theta_i) - (1 - \alpha_\tau) \sin^2(\theta_l)$$

where

α_n is the normal accommodation coefficient

α_τ is the tangential accommodation coefficient

The value of $F(\theta)$ is shown in Figure 6-22 for the 1985 GSFC data and also the data from earlier works (Seidl and Steinheil, 1974; Boring and Humphris, 1973; and Knechtel and Pitts, 1973). The previous data was projected to the low grazing ($\theta_i > 80$ deg) angles giving values that are much greater (less negative) than the test data. The equation for applying the $F(\theta)$ data is

$$CDLS = \cot(\theta) [1 + F(\theta)]$$

where

CDLS is the drag coefficient of the lateral surface which may be a flat plate or a cylinder wall

θ is the average impact angle measured from the surface normal and is a function of the spacecraft velocity and the velocity of the rarefied gas atmosphere

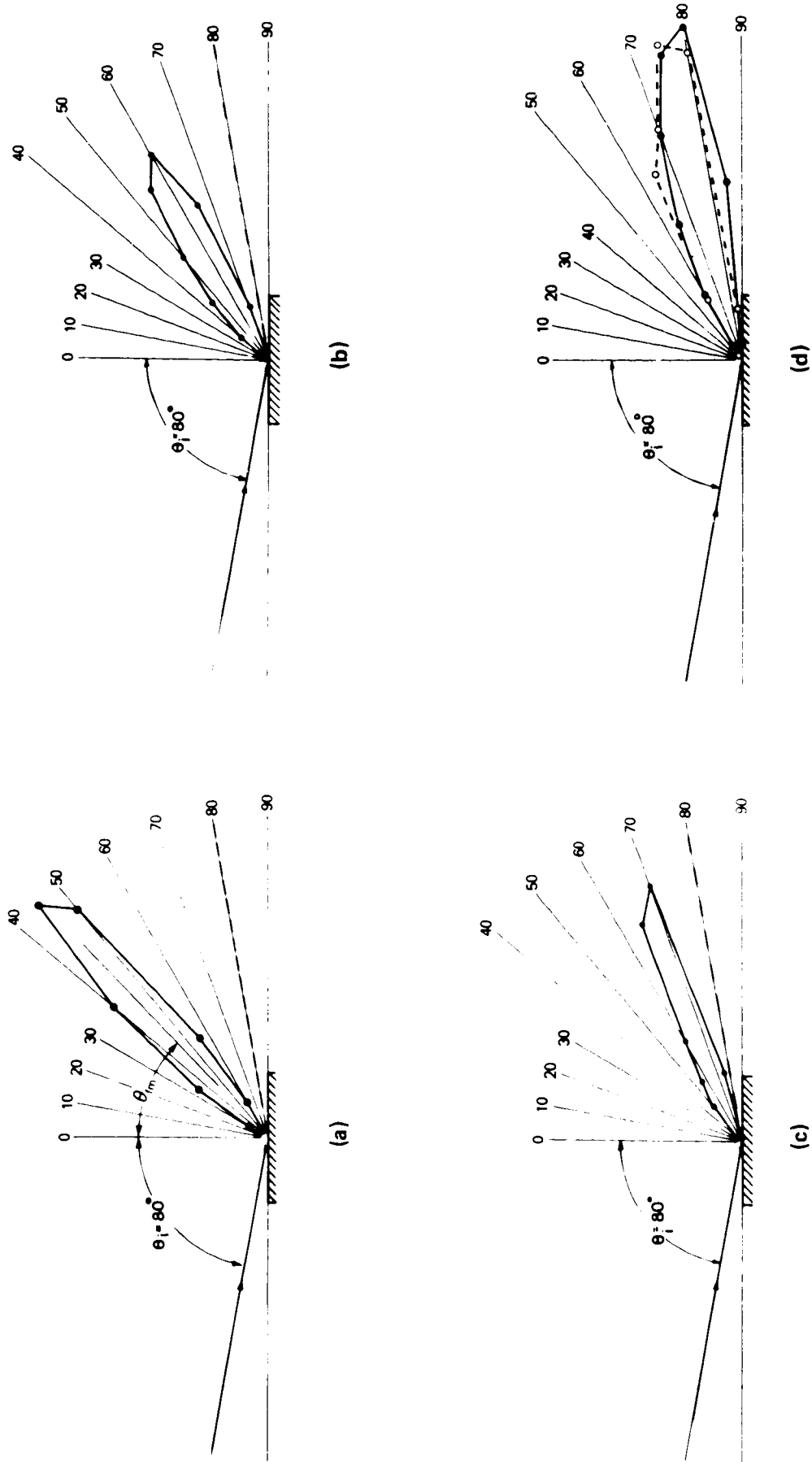
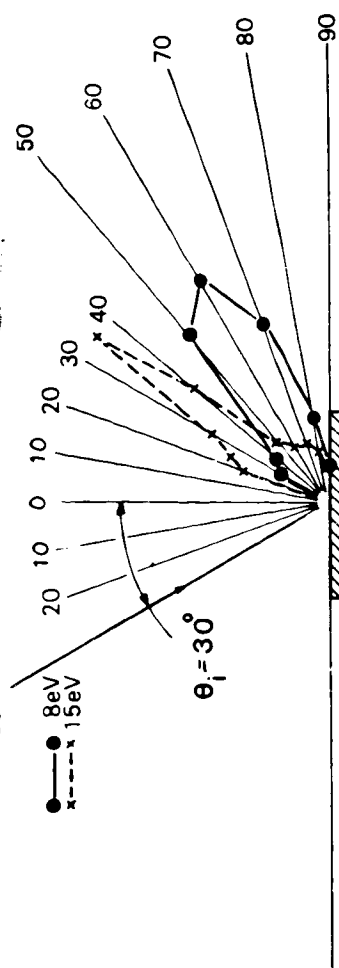
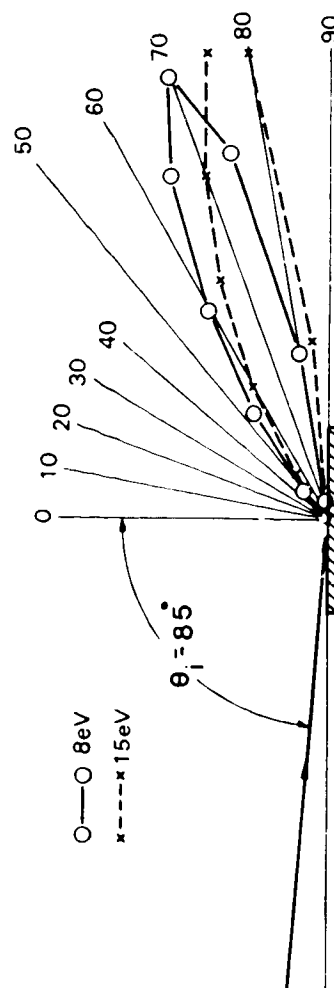


Figure 6-19. Reflected N_2^+ Ion Stream Pattern from Molybdenum with Impact Energy of (a) 1 eV, (b) 4 eV, (c) 8 eV, and (d) 16 eV



(a)



(b)

Figure 6-20. Reflected Ion Stream Pattern from Molybdenum with (a) $\theta_i = 30^\circ$,
(b) $\theta_i = 85^\circ$, and Two Impact Energy Levels

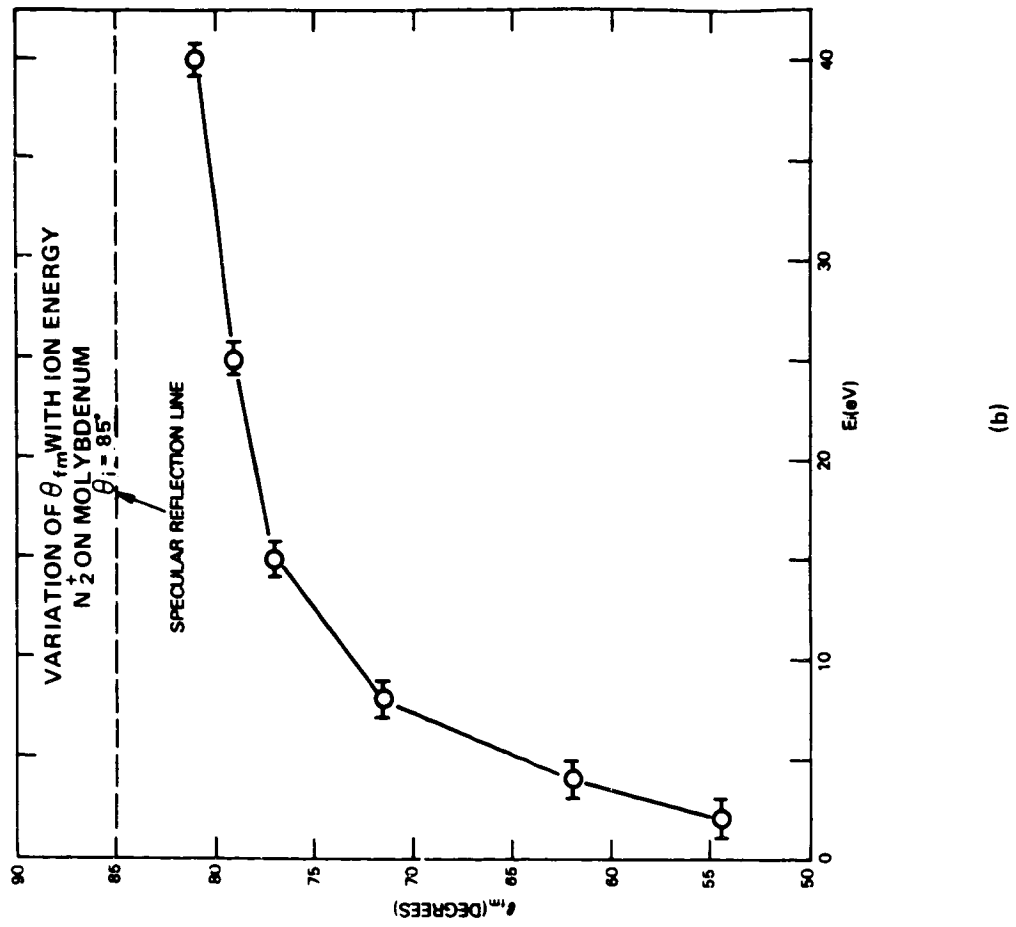
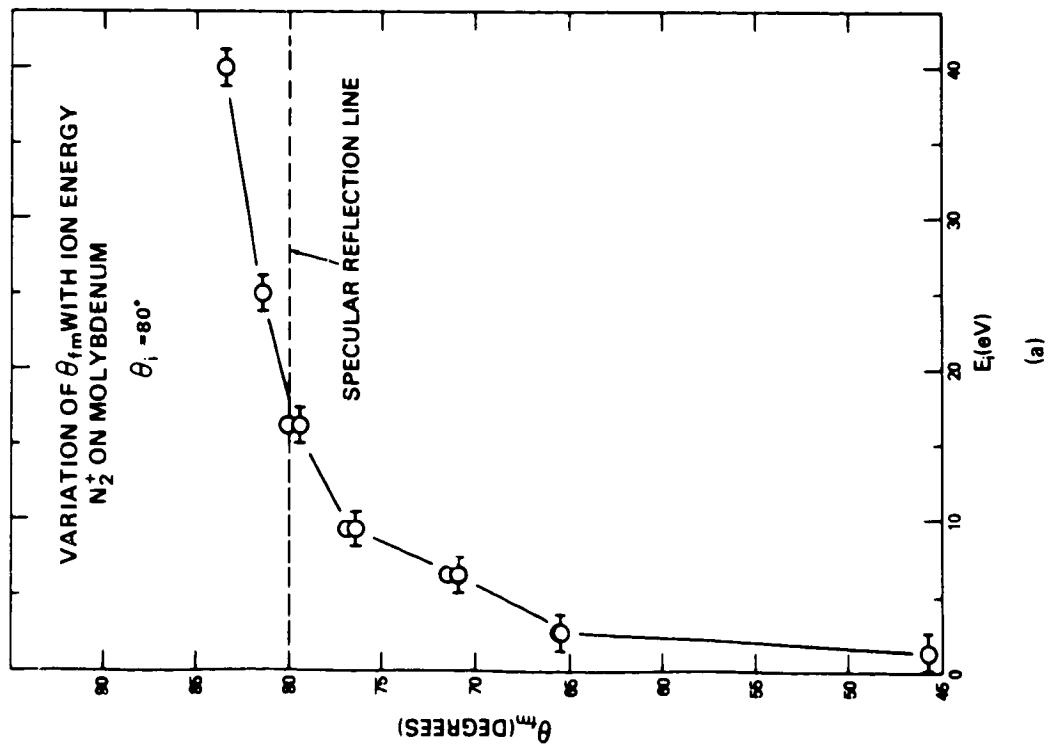


Figure 6-21. Fractional Momentum Transfer with (a) $\theta_i = 80^\circ$ and
(b) $\theta_i = 85^\circ$

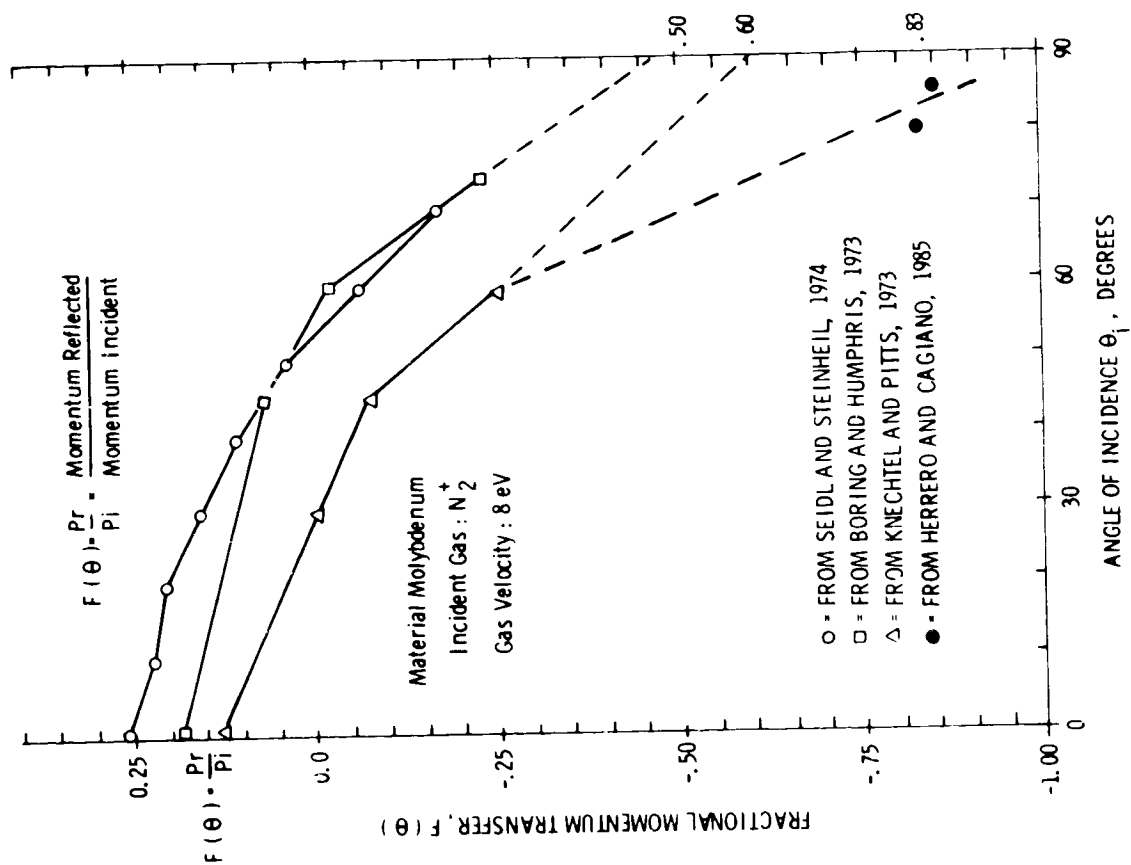


Figure 6-22. Gas to Surface Momentum Transfer

$F(\theta)$ is the fraction of momentum transfer; i.e., $F(\theta) = P_R/P_i$

where

P_R is the reflected momentum along the line of molecular impact

P_i is the incident momentum

Computing total drag force, F_D , based on the equation

$$F_D = 1/2 \rho V^2 A_D C_D$$

where

C_D is the effective drag coefficient for all surfaces

F_D is the total drag force, N

ρ is atmospheric density, kg/m³

V is spacecraft velocity, m/s

A_D is total projected area normal to the velocity vector, m²

in accordance with Herrero (1985), F_D is computed by summing the $A_D C_D$ for each drag-force related component of the spacecraft with A_D being the surface area of the corresponding component. The equations used to compute the individual C_D for the GRM are:

$$C_{Df} = 2 [1 + F(0)] \text{ for frontal surfaces; } F(0) = F(\theta_i) \text{ for } \theta_i = 0$$

For the frustrated cone with base radius R and front radius r ,

$$C_{Dc} = 2 \left\{ \left[1 + F(0) \right] \left(\frac{r}{R} \right)^2 + \left[1 + F(90^\circ - \phi) \right] \left[1 - \left(\frac{r}{R} \right)^2 \right] \right\} \text{ for total cone surface}$$

where ϕ is the cone half angle (see Table 6-1)

Table 6-1
Drag-force Related Dimensions

Element	Area
Antennas and support (2)	0.028 m ²
Horizon scanner (projected area)	0.067 m ²
Solar panel leading edge (2 panels)	0.107 m ²
Solar panel surface (2 panels, 2 surfaces each)	26.38 m ²
S/C truncated cone front	0.361 m ²
Cone surface	2.5 m ²
Cylinder base	0.866 m ²
Cylinder lateral surface	13.06 m ²
Solar panel	Length (L) = 4.72 m Width (W) = 1.397 m Thickness (t) = 0.0381 m
Cone half angle	$\phi = 11.5$
Cylinder	Length (L) = 3.97 m Diameter (D) = 1.05 m
S/C truncated cone front	diameter (d) = 0.678 m

$$CDLS = 2 \frac{f}{R} \cot(\theta_i) [1 + F(\theta_i)] \text{ for cylinder lateral surface}$$

$$CDLS = \left\{ \left[2 \frac{L}{t} \cot(\theta_i) \right] [1 + F(\theta_i)] \right\} \text{ for solar panel lateral surface}$$

where

r, R, L, W, t, ϕ are defined in Table 6-1

$F(\theta_i)$ is shown in Figure 6-22

$F(0)$ is $F(\theta_i)$ with $\theta_i = 0$ (i.e., parallel with the velocity vector)

For the GRM at 160 km altitude

$$\psi = \frac{V_{gas}}{V_s/c} = \frac{1 \text{ km/s}}{7.8 \text{ km/s}} \text{ radians} = 7.35 \text{ degrees maximum } (\theta_i = 90 - \psi = 82.7)$$

For the GRM A2 spacecraft, the following surface areas and dimensions constitute the applicable drag-force surfaces.

Using these formulas and the information in Figure 6-22, the following is computed and presented in Table 6-2.

$CDf = 2 (1 + 0.18) = 2.36$ for all surfaces normal to the velocity vector and the projected area of the horizon scanner

$$CD_{cone} = 2 \left\{ \left[(1 + 0.18) \frac{(0.678)^2}{1.05} \right] + [1 + F(78.5^\circ)] \left[1 - \frac{(0.678)^2}{1.05} \right] \right\}$$

$$= 2 [0.492 + (1 - 0.28) (0.583)]$$

$= 1.82$ (Note: $F(78.5^\circ)$ is obtained from Boring and Humphris data per Figure 6-22)

$$CDLS (\text{cylinder}) = \frac{2 \times 3.97}{1.05/2} \cot(82.7^\circ) [1 - 0.83]$$

Table 6-2
adjCDj Drag Force Components

Solar Panel Edge	ad1CD1 = 0.253 m ²
Antennas	ad2CD2 = 0.066 m ²
Horizon Sensor	ad3CD3 = 0.158 m ²
Cone	ad4CD4 = 1.576 m ² (normalized to πR^2)
Cylinder Surface	ad5CD5 = 0.285 m ² (normalized to πR^2)
Solar Panel	ad6CD6 = 0.577 m ²

$$A_D C_D = \sum_{j=1}^6 ad_j CD_j = 2.92 \text{ m}^2; C_D = \frac{A_D C_D}{A_D} = \frac{2.92}{1.068} = 2.73 \text{ (for the GRM A2 s/c)}$$

= 0.329 (Note: F (82.7°) is obtained from Herrero data, Figure 6-22)

$$CDLS \text{ (solar panels)} = \frac{2 \times 4.72}{0.0381} \cot (82.7^\circ) [1 - 0.83]$$

= 5.396 (Note: F (82.7°) is obtained from Herrero data, Figure 6-22)

The value 2.73 (Table 6-2) is considerably less than the 3.5 value used in sizing the fuel requirements for the mission. The difference is based upon the ion impact data shown (Figure 6-22) for the $\theta_i = 82.7$ case. For the present, the design will be based upon 1400 kg of fuel with the knowledge that if further testing with neutral particles substantiates the data, the design can be changed or a greater mission life margin can be incorporated into the flight plan.

For the GRM A1 spacecraft, the changes in Table 6-1 are:

- for C_{Dcone} : delete the front surface value $2 [1 + F(0)] (R)^2$ leaving $C_{Dcone} = 0.836$ plus an annular ring front surface C_D of $2 [1 + F(0)] \left(\frac{r^2 - r_b^2}{R^2} \right) =$

$$2.36 \left[\frac{(0.678/2)^2 - (0.203/2)^2}{(1.05/2)^2} \right] = (2.36) (0.38) = 0.896$$

- add C_{D7} of front cone of boom $C_{Dcone} =$

$$C_{D7} = 2 [(1 + F(74^\circ))] = 1.5$$

- add C_{D8} of boom $= \frac{2 \times 4.4}{0.1} \cot(82.7) [1 + F(82.7)]$

$$= 1.916$$

The change in Table 6-2 is:

- cone $a_{D4} C_{D4} = (0.866) (1.732) = 1.506 \text{ m}^2$

and the addition of the boom adds the following:

- boom cone $a_{D7} C_{D7} = [(0.032) (1.5)] = 0.048 \text{ m}^2$; $a_{D7} = \pi r_b^2 = \pi (0.203/2)^2$
- boom lateral surface $a_{D8} C_{D8} = [(0.032) (1.916)] = 0.061$; $a_{D8} = a_{D7}$

The A1 spacecraft summation of $a_{Dj} C_{Dj} = 2.954$. Consequently, the $C_D = 2.765$. This relatively small increase is a result of removing the flat front surface related to the boom mounting area of A2 and putting a cone on the front of the boom. The four star cameras that are on the boom are not included in the above calculations. The worst-case estimation for impact is equivalent to two times the horizon scanner or a net C_D star-camera increase of 0.296 for a total C_D of 3.06 for the A1 spacecraft.

6.6.4 PROPULSION TANK AVAILABILITY

The GRM requires that the fuel be held in a stable configuration to prevent slosh reactions and CM variation. In addition, fuel consumption from the tanks must be balanced. The manufacturing state-of-the-art for applicable tanks has not reached the size required for the GRM.

6.6.5 SCALAR MAGNETOMETER LIFE AND STABILITY

Magsat experienced failures in the lamp and RF exciter circuits of the cesium gas, optically pumped, scalar magnetometer. An analysis of the Magsat failures has been performed and a test program has been initiated with the manufacturer of the cesium lamps and gas cell components. This program, which will last until early spring of 1986, will determine:

- A 6500-hour life performance and transfer characteristics of cesium lamps
- A means of predicting lamp life based on the 6500 hour life tests
- An RF exciter design that accommodates variations in the lamp characteristics, thus ensuring successful operation over the duration of the mission

In addition, a study program is being performed by Dr. Edward Smith of Jet Propulsion Laboratory (JPL) to determine the applicability of metastable helium for the scalar magnetometer. This program has successfully demonstrated the feasibility of the helium design. The anticipated successful conclusion of these programs will provide the confidence that either design will yield an instrument capable of meeting the flight requirements.

6.6.6 VECTOR MAGNETOMETER AXIS ALIGNMENT

Critical to the vector magnetic field measurement is the determination of the orientation of the instrument axes. Magsat used the NASA standard star tracker and an Attitude Transfer System (ATS) (an optical tracking system). The GRM will use solid-state star cameras positioned on the boom and within 1 m of the magnetometers.

This location allows the utilization of an optical bench-like arrangement tying the star cameras to the magnetometer. Critical to this design is the development and

manufacture of star cameras based on a Charge Transfer Device (CTD) of either the charge injection or charge coupled technology. Both types have been under development for some time. For a Shuttle attached payload, JPL is developing the Advanced Star/Target Reference Optical Sensor (ASTROS) using Charged Coupled Devices (CCDs). The Ball Aerospace Division (BASD) has flown an optical target tracker on STS 41-F using Charge Injection Devices (CIDs). Neither system is directly usable on the GRM. Both systems have the potential of greatly improved (compared to the standard tracker) accuracy.

It is anticipated that the alignment errors, that are based on the Magsat performance, will be substantially less than presently allowed. Improvement is anticipated from not using an ATS and the expected superior performance of the solid-state star cameras. Critical to this improvement is the control of the magnetic fields generated by the star camera system. The previously stated one meter separation is based on the need to limit the spacecraft magnetic fields to no greater than 1 nT at the magnetometer.

6.6.7 ONBOARD FLIGHT CONTROLLER SYSTEM

The atmospheric density at the GRM flight altitude imposes a demanding requirement on the guidance and control system. Loss of attitude control with an ensuing large drag could cause re-entry within one orbit. Mission life is dependent on minimizing fuel consumption. Control of the drag makeup thruster duty cycle to provide as repetitive as possible a thruster/drag force induced coast-arc will be a factor in the successful processing of the velocity related data for gravity field determination.

6.7 DATA REDUCTION

6.7.1 PRE-PROCESSING OF SST DATA

The process of providing true \dot{s} , accurate to $1 \mu\text{m/s}$ (1σ), for the gravity field determination is shown in Figure 6-23.

The configuration in Figure 6-23 shows that the computation is performed on the ground. This configuration requires a much higher data rate than if each spacecraft had an onboard computer that sent to the ground only the $\dot{\theta}$ with the DISCOS generated $\dot{\delta}$ removed. Ground processing would then only have to remove the correlatable errors generated by oscillator phase jitter.

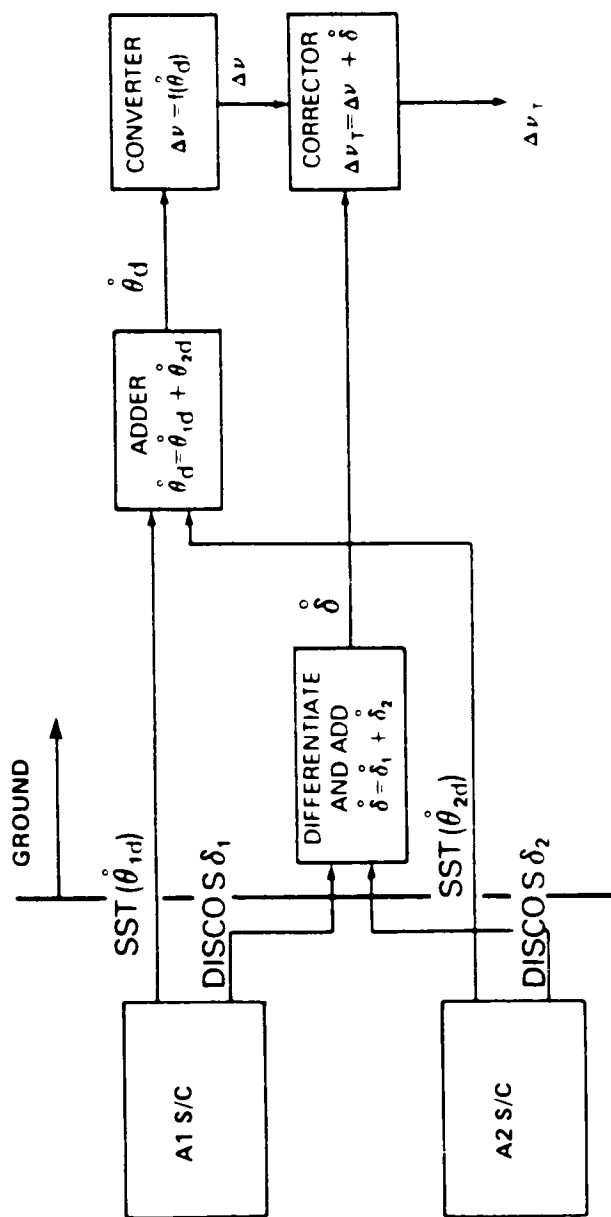


Figure 6-23. SST Correction Data Flow

6.7.2 GRAVITY FIELD COMPUTATION EFFICIENCY

To obtain a resolution of the gravity field down to 100 km with 1 mgal accuracy, it was necessary (paragraph 4.3) to carry the spherical harmonic expansion to about degree and order 300 or the gridded anomalies to about 1/2 deg equal area squares. In both cases, it is a massive task to obtain a computation for a precise adjustment in one iteration. Hence, approximation techniques are employed which may require more than one iteration for convergence, but which are computationally feasible. For a description of the process, consider the case of computation for the gravity parameter matrix of 1/2 deg equal area squares amounting to about 165,000 parameter values. The flight data inputs are the \dot{s} between the satellites and the two satellites-positions

that have first been determined from the Doppler tracking network of the DMA. The \dot{s} inputs have previously been averaged over a 4-second period. For an 88-minute orbit (approximately 160 km altitude) and 180-day mission, the number of \dot{s} inputs is approximately 3.87×10^6 data points. For the least squares method, the observational equations can be written in matrix form as

$$AY \approx R$$

Y = 165,000 x 1 vector of estimation parameters (considering just the gravity parameters)

R = $(3.87 \times 10^6) \times 1$ vector of measurement residuals

A = $(3.87 \times 10^6) \times 165,000$ matrix of partials of the modeled measurement residuals with respect to the estimation parameters

The estimation parameters were assumed to be mean gravity anomalies defined on 1/2-degree equal areas covering the Earth.

For a unit weight, the least squares normal equations are:

$$A^TAY = A^TR$$

where the normal matrix B ($B = A^TA$) will form the basis for discussing the computational time.

Although an estimate of the number of floating point operations (flops) required to form the complete B matrix for $N = 165,000$ unknowns and all observations is

$$4 \times 10^6 \times N^2 \approx 10^{11} \text{ megaflop}$$

the efficiency gained by the sparse matrix techniques employed for the spherical harmonics and the anomaly grid parameters greatly reduces this number.

A workload of 10^{11} megaflops for the complete B matrix is based upon contributions from all of the anomalies in the observation equation. Excluding anomalies remote from the observation point because of lack of sensitivity, a circular neighborhood of points or "cap" of $50'$ is employed in the computations shown in Table 6-3. A case

is also considered for computation where the anomaly grid is placed at satellite altitude, which will only require a small cap size yielding a very sparse matrix.

Table 6-3
Mathematical Computations for the Least Squares
Gravity Anomaly Matrix*

Cap Size	Megaflops	Cyber 205** Time
Full Matrix		
50° cap (ground)	1011	3 x 10 ⁵ hours
10° cap (altitude)	2 x 10 ⁸	600 hours
	3 x 10 ⁵	1 hour

*Using 1/2° equal area squares

**Assuming 100 megaflops per second

From Table 6-3 it is obvious that, the full matrix is not feasible in computational time, therefore, some form of approximation is necessary. For an at altitude solution with a 10 deg cap, the computational time of 1 hour for the normal matrix is not a significant task. Other aspects of the computations, such as the orbit integration, partial derivatives, the reference potential (equation 4-2), and calculation of the anomalies do become significant. These areas are currently being investigated by using a Cyber 205 vector processor. The approach of analytical techniques using sparse matrices is also being studied as discussed in paragraph 4.3. As previously mentioned, these approximate techniques must be tested and verified through simulations.

William M. Kaula, chairman of the Science Steering Group for Gravity, suggested the following summary for consideration of spherical harmonic computations. "If 100-km resolution is to be achieved, the spherical harmonic expansion should be carried to at least degree 200, resulting in about 40,000 unknowns. However, if the data sets are taken to be at least 12 days long (enough to give 100-km intervals of equator crossings), then the strongly non-zero terms of the normal equations will break down

into blocks of which the largest is about 100×100 , corresponding to harmonics of low order $m = 0, 1, 2, \dots$ and the same parity (n odd or even). These solutions can be made separately, but will be imperfect because orthogonality among the sets of harmonics of differing order and/or parity is imperfect due to non-commensurability of orbits and days. Hence there must be iterations, subtracting off the range-rates (or, better, off their Fourier transforms) the effect of the previous iteration (Kaula, 1983). For longer data sets a more precise tuning and hence probably faster convergence can be obtained (Colombo, 1984). However, very long data sets may sacrifice the strengthening obtained by varying the spacing of the spacecraft."

6.7.3 MAGNETIC FIELD MODEL COMPUTATION

In an analogous manner with the gravity field representation, a magnetic field model will be produced using the technique of spherical harmonic expansion. The magnetic field strength is obtained directly from the instruments either in units of frequency or counts for the scalar magnetometer or volts for the vector fluxgate magnetometer which are converted to the units of magnetic field (actual induction) nanotesla. ($1 \text{ nT} = 10^{-5} \text{ Gauss} = 10^{-9} \text{ Webers/m}^2$).

To produce the scalar and vector field models at satellite altitude, the field strength and orbital position information is required. The vector field models (north-south, east-west, and vertical components) require the orientation data obtained by the star cameras and sun sensors. The satellites positions along track, cross-track, and radial will be computed from the DMA Doppler data to accuracies of 100 m, 100 m, and 60 m respectively. The orientation of the vector magnetometer must be determined to within 20 arc-seconds. Computation of the magnetic field is minor when compared with the gravity field processing.

Even though the gravity field is perturbed by Earth and ocean tides, the magnetic field is subjected to greater external irregularities (called noise) with varying duration. This magnetic noise is due to the interaction between charged particles and the Earth's magnetic field; these charged particles are of extra terrestrial origin. It is very important that the data used in this spherical harmonic analysis are taken only at the time when the external field variations are at a minimum.

Ideally, these magnetic field data should be uniformly distributed around the Earth. If they are not, then a type of gridding procedure will be used to ensure uniform

global distribution. Unlike Magsat, which had an elliptical orbit, the magnetic field data from GRM will be obtained from a nearly circular orbit with an altitude of 160 km. Having these data on a surface of constant altitude will permit the use of the Fast Fourier Transform (FFT) method of field modeling (Ricardi and Burrows 1972). In the main or core field studies, a model with $N_{\max} = 14$ will be derived. Higher order models will be derived for special applications.

For example, with a larger spherical harmonic model ($N_{\max} = 23$), there is a half-wavelength resolution of 7.82 degrees or 869 km. If there is an increase to $N_{\max} = 180$, the resolution will be one degree or an 111 km half-wavelength. These higher order models can be used for mapping of the anomaly or crustal fields.

A spherical harmonic representation of the magnetic field was given in paragraph 4-4, equation 4-8, and it is repeated in equation 6-3.

$$V = a_m \sum_{n=1}^N \sum_{m=0}^n \left(\frac{a_m}{r} \right)^{n+1} [g_n^m \cos m\lambda + h_n^m \sin m\lambda] p_n^m(\cos \theta) \quad 6-3$$

$$X = \frac{1}{r} \frac{\partial V}{\partial \theta}; Y = -\frac{1}{r \sin \theta} \frac{\partial V}{\partial \lambda}; Z = \frac{\partial V}{\partial r} \quad 6-4$$

where

X, Y, and Z represent the north-south, east-west, and vertical vector components.

$a_m = 6371.2$ km mean radius of the Earth reference sphere

r = radial distance from the Earth's center

μ = colatitude measured from the North Pole

λ = longitude measured East from Greenwich

$P_n^m(\cos \mu)$ = Schmidt quasi-normalized type of the associated Legendre function of degree n and order m .

Computing a 180 degree and order magnetic field is computationally easier than an equally high degree and order gravity field. The magnetic field data enables the utilization of the Fourier analysis; the spherical harmonic coefficients can be computed directly from the two-dimensional Fourier coefficients. This procedure is based upon the fact that the associated Legendre polynomials can be expressed as the sum of a sine or cosine series (Macmillan, 1930). The only constraint in using this technique is that the data must be equally spaced on a spherical surface. The Fourier coefficients can be computed efficiently with the fast algorithm of Cooley and Tukey (1965). After they are computed, a set of weighting functions are applied to obtain the spherical harmonic coefficients. The technique was first described by Shuster (1903). A later version of essentially the same idea was given by Ricardi and Burrows (1972) to which a treatment of vector fields was added.

A currently operational computer program employing this method has been used to compute unnormalized spherical harmonics up to degree and order 28. An application of several methods published in recent literature (Olver and Smith, 1981, 1983) should allow the Associated Legendre polynomials to be evaluated up to orders of several thousand.

To estimate the time required to carry out the computation for a 180 x 180 model, it is only necessary to note that a 180 x 180 discrete Fourier transform must be computed. If the fast algorithm is employed, then the data must be padded out to the next power of two. A 256 x 256 complex double-precision out-of-core (Anderson, 1980) Fast Fourier Transform requires less than a minute of CPU time on the IBM 3081 at GSFC. The application of the weighting functions should no more than double that time. New methods can be applied to speed up this process even more; e.g., the self-sorting mixed radix transform of Temperton (1983) takes advantage of the parallel processors in machines like the Cyber. Moreover, still faster procedures could be developed on the Massively Parallel Processor (MPP) which has 16,384 processors arranged in a 128 x 128 array (Lerner, 1985).

6.7.4 COMPUTATIONAL SUMMARY

The number of computations and computer time required for the mathematical manipulation related to the number of floating point operations (FLOPS) is shown in Table 6-4. There is a need to develop algorithms for processing the gravity related data that are critical to mission success. It should be remembered that Table 6-4 data does not include computations related to preprocessing the range rate (\dot{s}) data, the corrections related to the DISCOS (δ) data, and numerous other computational tasks of orbit determination, star camera-to-vector magnetometer determination, as well as the normal input/output times. The overall computational task is formidable, but the previously discussed techniques (sparse matrix for gravity and fast Fourier transform for magnetics) are being developed and tested to determine feasibility.

6.8 ALTERNATE DESIGNS

The GRM design discussed in this document is capable of meeting the mission requirements. There are a number of alternate designs or competitive instruments that should be considered before the configuration design is finalized. These alternate designs are as follows:

Selected

Single-stage DISCOS

Single-stage DISCOS

Cesium scalar magnetometer

Single 4 N thruster firing every 16 seconds

Cylindrical shape

Buffed aluminum surface

Heat-pipe thermal control

Alternate

Two-stage DISCOS

Onboard calibration augmentation

Helium scalar magnetometer

1 N or smaller thruster firing every 4 or less seconds

Slightly tapered shape based on surface to gas accommodation coefficient

Glass surface based on surface gas accommodation coefficient

Active thermal control

Table 6-4
Number of Mathematical Computations

Factor	Gravity Computation for Sparse Normal Matrix		Magnetic Computation		
	Harmonics	1/2° x 1/2° Anomalies	Harmonics		1° x 1°
	N _{max} = 300	Cap of 10° at Altitude	N _{max} = 23	N _{max} = 180	Map
N _{OBS}	3.9 x 10 ⁶	3.9 x 10 ⁶	0.26 x 10 ⁶	3.9 x 10 ⁶	3.9 x 10 ⁶
N _{UNK}	90,601	3.14 x 10 ²	5.76 x 10 ²	32,761	41,253
N _{FLOPS}	3.6 x 10 ¹³	3.8 x 10 ¹¹	8.63 x 10 ¹⁰	--	1.61 x 10 ¹¹
Math. Comp. (Hours)	100	1.07	0.24	See text	0.45

N_{OBS} = (Mission life)/(sampling rate) = number of observations

N_{UNK} = Number of unknowns

N_{FLOPS} = (N_{UNK})² x N_{OBS}: for computing B = A^TA

= N_{UNK} x N_{OBS}: for computing 10° cap and 1° x 1° map

N_{UNK} = for 10° cap = {[π (5)²] / [4 π (57.3)²] } x (41,253) / (1/2)² = 3.14 x 10²

Doppler network tracking

Global Positioning System (GPS) tracking
(The GPS may become the prime system)

GRM A-2 spacecraft has no added
experiment

Aeronomy instrumentation for flight control
and atmospheric wind velocity determination

Star cameras not selected

CCD or CID type cameras

Other Experiments

Doppler laser experiment

6.9 INTERNATIONAL COOPERATIVE VENTURES

The GRM provides an opportunity for a possible joint venture with other satellite programs and the inclusion of additional instruments. Feasibility studies are being pursued that are related to the European Space Agency (ESA) Precise Orbit Positioning Satellite (POPSAT) and the French GRADIO gravity gradiometer.

6.9.1 POPSAT PROGRAM

The POPSAT spacecraft will be placed in a circular (98.6 deg inclination) orbit at an altitude of 7000 km. The GRM linkage to the POPSAT program would be with the inclusion of a transponder and antenna on one or both GRM spacecraft.

A transponder on GRM would generate a range rate link with the much higher orbiting POPSAT spacecraft. This link would provide a radial \dot{s} signal that would complement the \dot{s} signal generated by the two GRM satellites. Combining the two range rate (\dot{s}) signals in the data processing, may result in greater accuracy and efficiency in the recovery of the gravity anomaly data although studies needed to verify these assumptions have not yet been done. Presently, the cooperative venture is exploratory in nature with neither parties having performed more than a quick-look evaluation of the impact on and benefits to the respective missions.

6.9.2 GRADIO GRADIOMETER

The GRADIO is a gravity gradiometer that incorporates eight accelerometers located at the corners on a 1-meter per side cube. The GRADIO instrument is designed for a measurement accuracy of 10^{-2} Eötvös (1 Eötvös = 10^{-9} cm/s² per cm).

This initial 1-meter per side cube design by (ONERA) is too large for the GRM spacecraft and must be located at the centroid of the spacecraft. A study is required to determine the feasibility of locating the GRADIO offset from the centroid and to determine the instrument accuracy resulting from reducing the spacing between the accelerometers from the original design of 1-meter to the 0.5-meter GRM design.

If the gradiometer were included in the GRM, it would be flown on the A-2 spacecraft. Since the gradiometer makes in situ measurements of the gravitational potential, there is no need to carry an instrument on both spacecraft. Further, the A-2 spacecraft has a greater surplus of weight, power, and thermal performance than the A-1 spacecraft, which is carrying the magnetometers.

SECTION 7. MISSION DATA

7.1 DATA FLOW AND DATA HANDLING

Figure 7-1 shows the two networks (DMA and TDRSS) that provide the tracking, telemetry, and command links between the spacecraft and the MSOCC located at GSFC.

A draft Memorandum of Understanding (MOU), which has been discussed with the DMA, contains the following: The Doppler data obtained from the DMA will be Clean-Checked Source Data (CCHSD) of the format in existence at the time of the mission. Since the DMA does not deliver ground station clock corrections, NASA will also receive CCHSD for a TRANSIT satellite to compute the clock corrections. The DMA data will be delivered on magnetic tape weekly and will contain the previous 10 days tracking data. It must be noted that only the TRANET stations of the DMA network may be operational during the GRM flight. Consequently, it is recognized that any draft agreements with the DMA are inoperable except for frequency, accuracy, and type of data.

The NASA TDRSS link handles all command, tracking, and telemetry required for operation control and safekeeping of the spacecraft.

7.2 DATA STORAGE/AVAILABILITY

The approved Investigators will be provided data through the GRM Project. Other investigators will have access to the data via the National Space Science Data Center (NSSDC) located at GSFC. The data and data products are expected to be the following:

- a. Gravity
 - Spherical harmonic model with 400 km resolution within 12 months after launch
 - Interim geoid with 50 cm accuracy with 400 to 600 km resolution within 15 months after launch
 - Access to SST and ground-based tracking data tapes within 3 months after end of flight

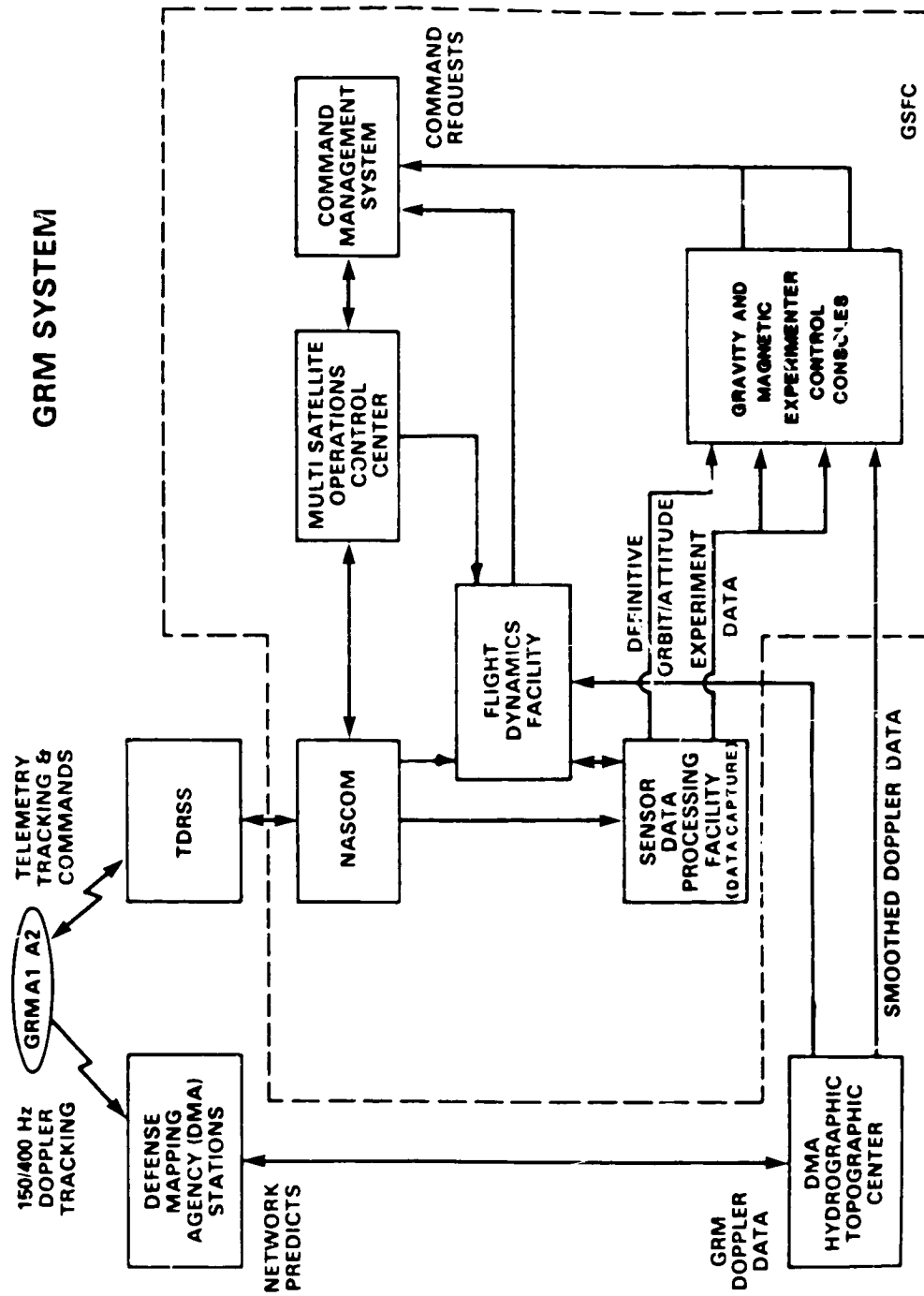


Figure 7-1. Ground Control and Data-processing Block Diagram

- Interim global anomaly map with 7.5 mgal accuracy and 400 km resolution within 15 months after launch

- Map of the gravity field with an accuracy of 2.5 mgal (1σ) and 100 km resolution within 30 months after launch

- Map of the geoid undulation differences with an accuracy of 10 cm (1σ) for distances of 100 to 10,000 km within 30 months after launch

b. Magnetic

- Processed data tapes containing scalar (2 nT), vector (5 nT), and orientation of 20 arc-min starting 4 months after launch

- Model of the field based on 20 arc-min resolution beginning 6 months after launch

- Global scalar anomaly map (at spacecraft altitude) with accuracy of 2 nT; 100 km resolution

- Global vector anomaly map (at spacecraft altitude) with accuracy of 5 nT; 100 km resolution

- Fine aspect (20 arc-sec) magnetic field model

- Processed data tapes with 20 arc-sec resolution starting 19 months after launch

c. Flight History--Because the GRM flight program has the following combined features, there is a unique opportunity to obtain aerodynamic and atmospheric data on a global basis over an extended period.

- Drag-free orbit

- 160 km altitude, circular orbit

- Polar orbit

- Recorded propulsion data
- Spacecraft-to-spacecraft precision Doppler tracking
- Precision ground system Doppler tracking
- Stable, well-defined spacecraft shape

For this reason, it is intended that the essential flight data be included in the mission data available from the NSSDC. Flight performance information should be available within 240 days after launch.

SECTION 8. SCIENTIFIC ANALYSIS OPPORTUNITIES

It is anticipated that opportunities will exist for investigators to participate in the planning and post launch phases of the GRM. Generally, these opportunities will be of two types: (1) participation in theoretical studies and analyses relating to techniques and methods for the development of gravity and magnetic field models of the accuracy and resolution specified for the GRM; and (2) use of the GRM data or field models for geophysical studies relating to the GRM objectives. In addition, it is anticipated that other federal agencies will, in collaboration with NASA, consider proposals for specific studies, and the application of GRM data to operational problems.

In preparation for the GRM data processing and field modeling, NASA is currently supporting in house research and research at several institutions. This activity is expected to continue for several years. Investigators that are interested in this research may submit proposals at any time.

Approximately one year after approval of the GRM, an Announcement of Opportunity (AO) will be issued for investigators to participate in mission planning and data analysis. The investigators selected in response to this AO and the requirements of their investigations are expected to influence the final data products produced by the Project. These investigations are expected to extend to several years after the post mission phase.

A second AO will be issued about one year after the launch of the GRM. Investigators responding to this AO are expected to make extensive use of the final GRM data products for continued geophysical studies.

Finally, the GRM data and the derived models will be archived in an appropriate center for several years after launch and will be available to the scientific and application community.

SECTION 9. PROGRAM SCHEDULE

The GRM program schedule is shown in Figure 9-1. The schedule is normalized to the new-start year and it presents the major milestones of the mission. If the program was approved for a new-start in October 1989, then the launch would be no later than March 1994.

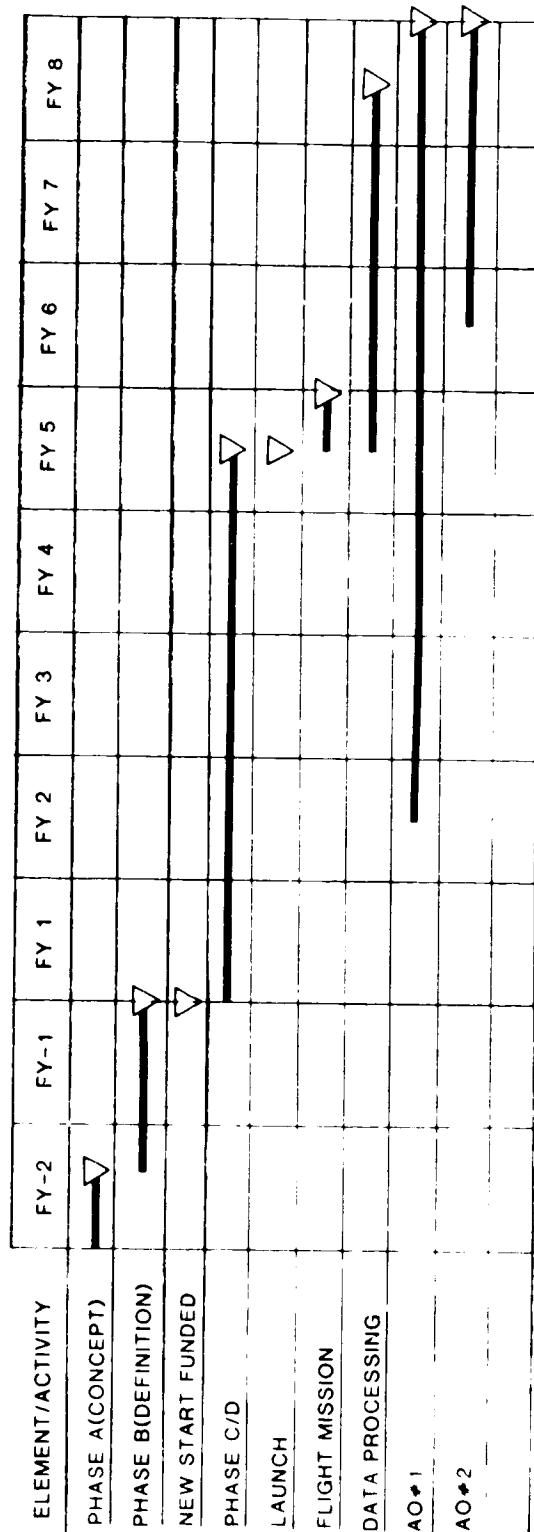


Figure 9-1. GRM Program Milestone Schedule

SECTION 10. SUMMARY OF GRM REPORT

The Geopotential Research Mission (GRM) originated in 1980 as the Gravity Satellite (GRAVSAT) and with the inclusion of a magnetometer in 1981, it became known as the GRAVSAT/MAGSAT. Since 1981, the mission has been further defined and the supporting scientific rationale has been delineated to a greater degree.

The current design configuration for the GRM has evolved according to mission needs and will continue to evolve as additional needs are identified. The current flight requirements for providing both the gravity and magnetic scientific data for mission success are substantiated in this report by detailed design information. Alternate designs and the possible inclusion of international projects in the GRM flight program are explored. Full attention is given to the design ideas of scientific investigators selected through the AO process or those independent scientists who may later desire access to mission data. Despite the detailed studies performed to date, the natural evolution of the mission design may result in an enhancement of the current GRM capability.

This GRM summary report has brought together information from numerous GRM related documents in the areas of scientific data, spacecraft engineering, data analysis and processing, and mission program information.

SECTION 11. REFERENCES

- Acuna, M. H., "The MAGSAT Precision Vector Magnetometer," Johns Hopkins Applied Physics Laboratory, Technical Digest, 01.1, no.3, 1980, pp. 210-213.
- Acuna, M. H., C. S. Scearce, J. B. Seek, and J. Scheifele, "The MAGSAT Vector Magnetometer - A Precision Fluxgate Magnetometer for the Measurement of the Geomagnetic Field," NASA TM-79656, October 1978.
- Anderson, G. L., "Stepwise Approach to Computing the Multidimensional Fast Fourier Transform of Large Arrays," IEEE Transactions on Acoustics, Speech, and Signal Processing, vol. ASSP-28, no. 3, 1980, pp. 280-283.
- Arkani-Hamed, J., W. E. S. Urquhart, and D. W. Strangway, "Scalar Magnetic Anomalies of Canada and Northern United States Derived from MAGSAT Data," Journal of Geophysical Research, vol. 90, 1985, pp. 2599-2608.
- Colombo, Oscar L., "The Global Mapping of Gravity with Two Satellites," Netherlands Geodetic Commission Publications on Geodesy, New Series, vol. 7, no. 3, 1984.
- Colombo, Oscar L., "Global Geopotential Modelling from Satellite-to-Satellite Tracking," Report No. 317, Ohio State University Dept. of Geodetic Science, Columbus, Ohio, October 1981.
- Cooley, J. W. and J. W. Tukey, "An Algorithm for the Machine Calculation of Complex Fourier Series," Math. Comput., vol. 19, April 1965, pp. 297-301.
- Farthing, W. H., "The MAGSAT Scalar Magnetometer," Johns Hopkins Applied Physics Laboratory, Technical Digest, vol. 1, no. 3, 1980, pp. 205-209.
- Goyal, H. K., R. R. B. Von Frese, W. J. Hinze, "Statistical Magnetic Anomalies from Satellite Measurements for Geologic Analysis," Trans. Amer. Geological Union, EOS, vol. 66, 1985, p. 255.
- Heiskanen, W., and H. Moritz, Physical Geodesy, W. H. Freeman and Company, San Francisco, California, 1967.

- Herrero, F. A., "The Drag Coefficient of Cylindrical Spacecraft in Orbit at Altitudes Greater than 150 Km," NASA-TM 85043, May 1983.
- Herrero, F. A., "The Lateral Surface Drag Coefficient of Cylindrical Spacecraft in a Rarefied Finite Temperature Atmosphere," AIAA Journal, vol. 23, no. 6, pp. 862-867.
- Herrero, F. A. and S. Cagiano, " N_2^+ Scattering from Molybdenum Surfaces at Grazing Angles: Implications for the Lateral Surface Drag Coefficients," to be published, 1985.
- Jekeli, C. and R. H. Rapp, "Accuracy of the Determination of Mean Anomalies and Mean Geoid Undulations from a Satellite Gravity Field Mapping Mission," Report No. 307, Ohio State University Department of Geodetic Science, Columbus, Ohio, August 1980.
- Jenkins, R. E., "Performance in Orbit of the TRIAD Disturbance Compensation System," Johns Hopkins Applied Physics Laboratory, Technical Digest, vol. 12, no. 2, pp. 27-35.
- Kahn, W. E. and F. J. Von Bun, "Error Analysis for a Gravity Gradiometer Mission," IEEE Transactions on Geoscience and Remote Sensing, vol. GE-23, July 1985, pp. 517-523.
- Kahn, W. D., S. M. Klosko, and W. T. Wells, "Mean Gravity Anomalies from a Combination of APOLLO/ATS 6 and GEOS 3/ATS SST Tracking Campaigns," Journal of Geophysical Research, vol. 87, no. B4, 1982, pp. 2904-2918.
- Kahn, W. D. and T. L. Felsentreger, "Signal Analysis and Error Analysis Studies for a Geopotential Research Mission (GRM)," NASA TM-83970, July 1982.
- Kaula, W. M., "Interference of Variations in the Gravity Field," Journal of Geophysical Research, vol. 88, October 10, 1983, pp. 8345-8349.
- Kaula, W. M. and C. G. A. Harrison, "The Geopotential Research Mission Scientific Rationale," 1983.
- Keating, T. and D. Smith, "Coupled Orbiting Inertial Reference Systems and Geopotential Research Mission (GRM) Geodesy," AIAA Guidance and Control Conferences, Seattle, Washington, August 20-22, 1984, p. 264.

- Langel, R. A., "The Magnetic Earth as Seen from MAGSAT, Initial Results," Geophysical Research Letters, vol. 9, 1982, pp. 239-242.
- Langel, R. A., R. H. Estes, G. D. Mead, E. B. Fabiano, and E. R. Lancaster, "Initial Geomagnetic Field Model from MAGSAT Vector Data, Geophysics Research Letters, vol. 7, 1980, pp. 793-796.
- Langel, R. A., J. D. Phillips, and R. J. Homer, "Initial Scalar Magnetic Anomaly Map from MAGSAT," Geophysical Research Letters, vol. 9, 1982, pp. 269-272.
- Langel, R. A. and R. A. Sweeney, "Asymmetric Ring Current at Twilight Local Time," Journal of Geophysical Research, vol. 76, 1971, pp. 4420-4427.
- Lerch, F. J. and B. Putney, "GRAVSAT (GMM) Simulations for Geopotential Recovery," Paper Presented at the AGH Meeting, Baltimore, Maryland, June 1, 1983.
- Lerch, F. J., W. D. Kahn, B. H. Putney, T. L. Felsentreger, and D. E. Smith, "GRAVSAT Simulation Studies," Paper Presented at the Fourth Annual Conference on the NASA Geodynamics Program, GSFC, January 26-29, 1982.
- Lerner, E. J., "Parallel Processing Gets Down to Business," High Technology, vol. 5, no. 7, 1985, pp. 20-28.
- MacArthur, J. L., A. Finkel, and E. Westerfield, "GRAVSAT/MAGSAT-A Range and Range Rate Report," Johns Hopkins Applied Physics Laboratory Report, SDO 6120, September 1981.
- MacArthur, J. L. and A. S. Posner, "Satellite-to-Satellite Range Rate Measurement," IEEE Transactions on Geoscience and Remote Sensing, vol. GE-23, July 1985, pp. 517-523.
- Macmillan, W. D., 1930, The Theory of the Potential, Dover, New York, reprint, 1953.
- Mayhew, M. A., "Inversion of Satellite Magnetic Anomaly Data," Journal Geophysical Research, vol. 45, 1979, pp. 119-128.
- Oliver, F. W. J. and J. M. Smith, "Associated Legendre Functions on the Cut.," Journal of Computational Physics, vol. 51, 1983, pp. 502-518.

- Parkinson, W. D., "Introduction to Geomagnetism," Scottish Academic Press, Edinburgh, U.K., 1983, p. 433.
- Ray, J. C. and R. E. Jenkins, "GRAVSAT/MAGSAT-A Guidance and Control System Annual Report 1981," Johns Hopkins Applied Physics Laboratory Report, SDO 6179, September 1981.
- Ray, J. C., et al., "Attitude and Translation Control of a Low Altitude GRAVSAT," AIAA Paper, 82-1416, AIAA/AAS Astrodynamics Conference, August 1982.
- Regan, R. D., J. C. Cain, and M. W. Davis, "A Global Magnetic Anomaly Data," Journal of Geophysical Research, vol. 80, 1975, pp. 794-802.
- Ricardi, L. J. and M. L. Burrows, "A Recursion Technique for Expanding a Function in Spherical Harmonics," IEEE Trans. Computers, vol. C-21, 1972, pp. 583-585.
- Schnetzler, C. C., P. T. Taylor, and R. A. Langel, "Mapping Magnetized Geologic Structures from Space: The Effects of Orbital and Body Parameters," NASA TM-86134.
- Schutz, B. E. and B. D. Tapley, "Simulation and Analysis of a Geopotential Research Mission," report for NASA Geodynamics, proposal G-15-85, in print.
- Shuster, A., "On Some Definite Integrals and a New Method of Reducing a Function of Spherical Co-ordinates to a Series of Spherical Harmonics," Phil. Trans. Roy. Soc., London, vol. 200, 1903, pp. 181-211.
- Sonnabend, D., A. Vijayaraghavan, and T. Hagstrom, "Electrostatic Disturbance Forces on a 3-Axis Drag-Free Sensor," Journal of Guidance and Control Dynamics, vol. 7, no. 3, May/June 1984.
- Spiegel, Murry R., Probability and Statistics, Schaum's Outline Series, McGraw-Hill Book Company, 1975, p. 160.
- Taylor, P. T. and J. J. Frawley, "Kursk Magnetic Anomaly (KMA) at Satellite Altitude", Transactions of the American Geophysical Union, EOS, 1985, p. 870.
- Temperton, C., "Self-Sorting Mixed-Radix Fast Fourier Transforms," Journal of Complete Physics, vol. 52, 1983, pp. 1-23.

- Uy, M. O., "Oxygen Atom Reactions with Materials at Low Altitudes," Attachment to JHU/APL Report SOR-84089, December 1982.
- Wagner, C. A., "Direct Determination of Gravitational Harmonics from Low-Low GRAVSAT Data," Journal of Geophysical Research, Vol. 88, no. 1612, December 10, 1983, pp. 10,308-10,321.
- Wagner, C. A. and C. C. Goad, "Direct Determination of Gravitational Harmonics from Low-Low GRAVSAT Data," EOS C314-05, vol. 63, no. 45, November 9, 1982.
- Walter, L. S., Geodynamics, NASA Conferences Publication No. 2325.
- Webster, W. J., P. T. Taylor, C. C. Schnetzler, and R. A. Langel, "The Magnetic Field of the Earth: Performance Considerations for Space-Based Observing Systems," IEEE Transactions on Geoscience and Remote Sensing, vol. GE-23, July 1985, pp. 541-551.
- Yionoulis, S. M., D. B. Klein, and Jenkins, "GRAVSAT Data Analysis: Computer Selection Study," Johns Hopkins University/Applied Physics Laboratory Report SDO 6155, August 1981.
- Yionoulis, S. M. and V. L. Pisacane, "Geopotential Research Mission: Status Report," IEEE Transactions on Geoscience and Remote Sensing, vol. GE-23, July 1985, pp. 511-516.
- Committee on Earth Sciences: "A Strategy for Earth Science from Space in the 1980's; Part I: Solid Earth and Oceans," NRC Space Science Board, 1982.
- Committee on Solar-Terrestrial Relationships: "Solar Systems Space Physics in the 1980's: A Research Strategy," NRC Space Science Board, 1980.
- Goddard Space Flight Center: "Geopotential Research Mission (GRM)," NASA Goddard Space Flight Center, 1982.
- GRAVSAT Users Working Group: "GRAVSAT Data Analysis," NASA Goddard Space Flight Center, 1982.
- Journal of Geophysical Research, "Solid Earth and Planets," vol. 90, no. B3, published by American Geophysical Union, February 28, 1985.

JPL Study Team: "Ocean Topography Experiment (TOPEX), Prephase B Report," NASA Jet Propulsion Laboratory, 1982.

Panel on Gravity Field and Sea Level: "Applications of a Dedicated Gravitational Satellite Mission," NRC Committee on Geodesy, 1979.

Reference Data for Radio Engineers, Howard W. Sams and Co., Inc., ITT Sixth Edition, 1979, pp. 42-2, 42-3.

Research Briefing Panel: "The Solid Earth Sciences," Research Briefings, National Academy Press, 1983.

Reviews of Geophysics and Space Physics, Papers from U.S. National Report to IUGG, vol. 21, no. 3, published by American Geophysical Union, April 1983.

TOPEX Science Working Group: "Satellite Altimetry Measurements of the Ocean," NASA Jet Propulsion Laboratory, 1981.

U.S. Geodynamics Committee: "Geodynamics in the 1980's," National Research Council, 1980.

APPENDIX A
ACRONYM LIST

ACRONYMS

AFGL	Air Force Geophysical Laboratory
AO	Announcement of Opportunity
ASTROS	Advanced Star/Target Reference Optical Sensor
ATS	Attitude Transfer System
BASD	Bail Aerospace Division
BCA	Ball-Centering Angle
BPSK	Binary Phase-Shift Key
CCDS	Charged Coupled Devices
CCHSD	Clean-Checked Source Data
CID	Change Injection Device
CM	Center of Mass
CTD	Change Transfer Device
CW	Continuous Wave
C&DH	Command and Data Handling System
DE	Dynamics Explorer
DGI	Data Group 1
DISCOS	Disturbance Compensation System
DMA	Defense Mapping Agency
DMA/HTC	DMA Hydrographic/Topographic Center
DOD	Department of Defense
DOMSAT	Domestic Satellite
DRIRU	Dry Rotor Inertial Reference Unit
ESA	European Space Agency
FFT	Fast Fourier Transform
FTS-1000	Frequency and Time Systems 1000
GPS	Global Positioning System
GRAVSAT	Gravity Satellite
GRM	Geopotential Research Mission
GSFC	Goddard Space Flight Center
G&CS	Guidance and Control System
HEDD	Hughes Electron Dynamics Division

ACRONYMS (Continued)

IF	Intermediate Frequency
IGRF	International Geomagnetic Reference Field
JHU/APL	Johns Hopkins University/Applied Physics Laboratory
JPL	Jet Propulsion Laboratory
LFC	Large Format Camera
MA	Multiple Access
MOU	Memorandum of Understanding
MPP	Massively Parallel Processor
MSOCC	Multisatellite Operations Control Center
NAS	National Academy of Sciences
NASA	National Aeronautics and Space Administration
NASCOM	NASA Communications Network
NRC	National Research Council
NSSDC	National Space Science Data Center
OBC	Onboard Computer
PC	Personal Computer
PRN	Pseudo Random Noise
POGO	Polar-Orbiting Geophysical Observatory
POPSAT	Precise Orbit Positioning Satellite
RAM	Random-Access Memory
RF	Radio-Frequency
RMS	Root-Mean-Square
RCM	Read-Only Memory
RSS	Root Sum Squared
SIR	Shuttle Imaging Radar
SSA	S-band Single Access
SSB	Space Science Board
SSG	Scientific Steering Group
SST	Satellite-to-Satellite Tracking
STS	Space Transportation System

ACRONYMS (Continued)

TDRS
TDRSS
TIROS-N
TOPEX
TRANET
TRIAD

VRM

WSGT
WSMC
W-cm

ZOE

Tracking Data Relay Satellite
Tracking Data Relay Satellite System
Television Infrared Observation Satellite
Ocean Topography Experiment
Tracking Network
Transit Improved and DISCOS

Venus Radar Mapper

White Sands Ground Terminal
Western Space and Missile Center
Watt-centimeters

Zone of Exclusion

APPENDIX B
DEFINITION OF TERMS

b/s	:	Bits/second
a _e	:	Semi-major radius of the Earth, 6378.14 km at the Equator
a _m	:	Reference mean radius of the Earth for the magnetic sphere, 6371.2 km
λ	:	East longitude
φ	:	Geocentric latitude
θ	:	Geocentric colatitude (referenced to the North Pole)
P _n ^m (cos θ)	:	Associated Legendre functions of degree n and order m and of the Schmidt quasi-normal type
V	:	Geomagnetic potential; tesla-meter
g _m	:	Spherical harmonic coefficients in units of tesla
h _m	:	Spherical harmonic coefficients in units of tesla
B	:	Magnetic flux density or magnetic induction (webers/m ²)
∇	:	Vector operator $\bar{i}\frac{\partial}{\partial x} + \bar{j}\frac{\partial}{\partial y} + \bar{k}\frac{\partial}{\partial z}$
r	:	Radial distance from the Earth's geocentric center to the point of measurement
g	:	Earth's gravitational acceleration (9.80665 m/s ²)
λg	:	Note $\bar{g} = \sqrt{U}$ where U is the scalar gravitational potential
λv	:	Gravity field anomaly in units of milligal
μ	:	Velocity difference between the orbital velocities of two spacecraft
	:	Universal Earth gravitational constant (km ³ /s ²) also termed GM = 3.986012 x 10 ⁵ km ³ /s ²
P _{lm}	:	Normalized Legendre polynomial coefficients of degree l and order m
C _{lm} , S _{lm}	:	Normalized coefficients of the cosine and sine terms of the spherical expansion of degree l and order m
R	:	Radius of gravity reference sphere for the residual anomaly, λg
s	:	Line-of-sight distance between the two GRM satellites
ṡ	:	Rate of change of line-of-sight between the two satellites; also termed range-rate
λs	:	Noise on the ṡ signal
f	:	Frequency (Hz)
Hz	:	Frequency rate in periods per second
Gal	:	Acceleration of 10 ⁻² m/s ²
milligal	:	(mgal) = 10 ⁻⁵ m/s ²
tesla	:	Unit of induced magnetization (B) in webers/m ²

: Gyromagnetic ratio of cesium (nT/Hz)
 : 10⁻⁹ tesla
 : 10⁻⁹ tesla = 1 gamma
 : Magnetic field intensity (amp/meter)
 : Magnetic permeability (henry/meter)
 : Speed of light 2.997925 x 10⁸ meters/second
 : Thermal absorption factor
 : Thermal emittance factor
 : Unit of pressure (N/m²)
 : Unit of pressure; pounds force per square inch = 6.894 x 10³ Pa
 : Newton; force = kg m/s²
 : Fuel overflow tanks
 : Gas to surface normal accommodation coefficient
 : Gas to surface tangential accommodation coefficient
 : Observed shift in frequency of a signal radiating between two objects,
 : one of which is moving

$$f_D = f_C (1 \pm \frac{v}{c})$$

where f_D = received frequency
 f_C = transmitted frequency
 v = relative speed of moving observer
 c = speed of light

Allan variance: Defined by $\frac{\Delta f}{f}$

Δf : frequency jitter

dB : Decibel = $10 \log_{10} \frac{P_{OUT}}{P_{IN}}$; P_{IN} = Input Power, P_O =Output Power

N_2^+

: Molecular nitrogen ion

δ : Incremental change for the DISCOS: δ is the off-center position of the proof-mass

proof mass

: The reference mass for the DISCOS system

ρ : Atmospheric density; kg/m³

A_D : Total frontal projected area for drag force determination

A_{Di} : Frontal projected area for a subset of the total drag force area

C_D : Total drag coefficient

C_{Di} : Drag coefficient of a subset of the total C_D

NOBS : Number of observations

NUNKS : Number of unknowns

NFLOPS : Number of FLOPS

: Number of floating point operations

T : Gravitational disturbance potential at altitude
 Eotvos : Unit of acceleration gradient ($10^{-9}/s^2$)
 geoid : Surface of equal gravitational potential of Earth
 h : Height of the geoid
 mean : $E(x) = \sum p_k x_k$ = Expected value of $x = \mu$
 p_k : Probability of k th event
 RMS : Root-Mean-Square = $[E(x^2)]^{1/2} = [\sum p_k x_k^2]^{1/2}$
 Variance : $\sigma^2 = E[(x-\mu)^2] = \sum p_k (x_k - \mu)^2$
 σ : Sigma, standard deviation = $[\sum p_k (x_k - \mu)^2]^{1/2}$
 VAR(x) : $E(x - \mu)^2$
 σ_x : Standard Deviation = $[E(x - \mu)^2]^{1/2} = [\sum_{j=1}^{\mu} (x_j - \mu)^2 f(x_j)]^{1/2}$

where: $f(x)$ is the probability of the j th event
 if $f(x_j)$'s are all equal, then $f(x_j) = 1/n$ and

$$\sigma^2 = \sum_{j=1}^{\mu} (x_j - \mu)^2 / n$$

$$s^2 : \text{Sample Variance} = \sum_{j=1}^{\mu} (X_j - \mu)^2 / n$$

where: X_j 's are random variables of a sample of size n , and
 $E(s^2) = (n-1)/n \cdot \sigma^2$ = expected value of the sample variance

$$\hat{s}^2 : \text{Unbiased estimator} = (n/n-1) s^2 = \sum_{j=1}^{\mu} (x_j - \mu)^2 / (n-1)$$

$$\hat{s}^2 : \text{Equal to } \sigma^2, \text{ therefore} = \left[\sum_{j=1}^{\mu} (x_j - \mu)^2 / (n-1) \right]^{1/2} \text{ for statistical samples}$$

APPENDIX C

MAJOR CONTRIBUTORS TO GRM REPORT

GEOPOTENTIAL RESEARCH MISSION SCIENCE STEERING GROUP

Christopher G. A. Harrison, Cochairman (University of Miami)
William M. Kaula, Cochairman (NOAA), National Geodetic Survey
Shelton S. Alexander (Pennsylvania State University)
Don L. Anderson (California Institute of Technology)
John R. Apel (Johns Hopkins University/Applied Physics Laboratory)
Edward R. Benton (University of Colorado)
Paul J. Coleman, Jr. (UCLA)
Charles L. Drake (Dartmouth College)
E. Michael Gaposchkin (MIT Lincoln Laboratory)
William Hinze (Purdue University)
Timothy Killeen (University of Michigan)
John E. Naugle (Fairchild)
Richard H. Rapp (Ohio State University)
Irwin I. Shapiro (Harvard Center for Astrophysics)
Sean C. Solomon (Massachusetts Institute of Technology)
Byron D. Tapley (University of Texas)
Anthony B. Watts (Columbia University)
Owen W. Williams, Consultant

GODDARD SPACE FLIGHT CENTER

Werner D. Kahn, Laboratory for Terrestrial Physics
Thomas Keating, Advanced Mission Analysis Office, GRM Study Manager
Francis J. Lerch, Laboratory for Terrestrial Physics
David E. Smith, Laboratory for Terrestrial Physics, Project Scientist for Gravity
Patrick T. Taylor, Laboratory for Terrestrial Physics, Project Scientist for Magnetism
Federico A. Herrero, Laboratory for Atmospheres

GRAVSAT USERS WORKING GROUP

Richard H. Rapp, Chairman, Ohio State University
Richard J. Anderle, General Electric Co.
Peter Bender, National Bureau of Standards/Joint Institute for Laboratory Astrophysics,
(NBS/JILA)
Carl Bowin, Woods Hole Oceanographic Institution
John Breakwell, Stanford University
Bernard Chovitz, National Geodetic Survey
Daniel B. DeBra, Stanford University

John DeNoyer, U.S. Geological Survey
Thomas Fischetti, NASA Headquarters (Retired)
E. M. Gaposchkin, MIT Lincoln Laboratory
William Kaula, NOAA, National Geodetic Survey
Cliff Leitao, NASA, Wallops Flight Center (DAS)
Frank Lerch, Goddard Space Flight Center
Marcia McNutt, Massachusetts Institute of Technology
William L. Sjogern, Jet Propulsion Laboratory
Byron D. Tapley, University of Texas
Anthony B. Watts, Lamont-Doherty Geological Observatory
Jack Whitehead, Woods Hole Oceanographic Institution
Carl Wunsch, Massachusetts Institute of Technology

JOHNS HOPKINS UNIVERSITY/APPLIED PHYSICS LABORATORY

John L. MacArthur
J. Courtney Ray
George Bush
Steve M. Yionoulis

NASA HEADQUARTERS

Charles J. Finley, Geodynamics Branch
Thomas L. Fischetti, Geodynamics Branch Head (Retired)
Edward A. Flinn, Geodynamics Program Scientist

STANFORD UNIVERSITY

Daniel B. DeBra

SIGMA SCIENTIFIC CONSULTANTS, INC.

John L. Junkins

ACKNOWLEDGMENTS

S. Bergeson-Willis (GRAVSAT Study Manager), D. Suddeth, M. Acuna, W. Hibbard, B. Bromberg, R. Langel, and H. Farthing, Goddard Space Flight Center; T. Wyatt (Program Manager) and V. Pisacane, Johns Hopkins University/Applied Physics Laboratory; L. Carpenter, EG&G; S. E. Bradley (Technical Writer/Editor), Engineering and Economics Research, Inc.; J. J. Frawley, Herring Bay Geophysics, Inc., D. Sonnabend, Jet Propulsion Laboratory

APPENDIX D

BIBLIOGRAPHY

These publications are of general interest and are useful for background knowledge. They have not been cited in this report.

- Anderson, G. L., "A Step-wise Approach to Computing the Multidimensional Fast Fourier Transform of Large Arrays," IEEE Trans. on Acous., Speech and Sig. Proc., vol. ASSP-28, no. 3, 1980, pp. 280-284.
- Argentiero, P. and B. Lowrey, "A Comparison of Satellite Systems for Gravity Field Measurements, NASA/GSFC X-932-77-267, November 1977
- Bender, P., "Signal Equation and Error Model," GRAVSAT Users Data Analysis Working Group Summary Report, Goddard Space Flight Center, June 30, 1982, pp. 17-19.
- Benton, E. R., L. A. Muth, and M. Stix, "Magnetic Contour Maps at the Core-mantle Boundary," J. Geomag. Geoelectr., 31, 1979, pp. 615-626.
- Bergeson-Willis, S. E., D. H. Suddeth, and D. E. Smith, "Preliminary Execution Phase Project Plan for Gravity Satellite (GRAVSAT-A)," NASA Goddard Space Flight Center, December 1980.
- Bhattacharyya, B. K., "Reduction and Treatment of Magnetic Anomalies of Crustal Origin in Satellite Data," Journal of Geophysical Research, 82, 1977, pp. 3379-3390.
- Boring, J. W. and R. R. Humphris, "Drag Coefficients for Spheres in Free Molecule Flow in 0 at Satellite Velocities," NASA Report no. CR-2255, March 1973.
- Bose, S. C. and G. E. Thobe "Gravity Field Recovery by Fourier Analysis of Satellite-to-Satellite Range Rate," Applied Science Analytics Inc.; ASA Technical Report 84-4, interim report for August 1983 to August 1984.
- Breakwell, J. V., "Satellite Determination of Short Wavelength Gravity Variations," AAS Paper 79-151, Provincetown, Massachusetts, June 25-27, 1979.
- Colombo, O. L., "Global Geopotential Modelling from Satellite-to-Satellite Tracking," Rep. 317, Dept. Geod. Sci. Surv., Ohio State University, Columbus, Ohio, 1981.
- Cooke, G. E., "Satellite Drag Coefficients, Planet Space Science, 13, 1965, pp. 929-946.
- Cooley, J. L., K. G. Nickerson, R. W. Herder, and A. B. Glass, "Application of Altitude Control Techniques for Low Altitude Earth Satellites," AAS/AIAA Astrodynamics Conference, Grand Teton National Park, Wyoming, September 7-9, 1977.

- DeBra, D. B., R. A. Van Patten, and R. Hacker, "Special Report on GRAVSAT Research," Stanford Univ. Report to NASA/GSFC (S. Kant/Code 700), October 1978.
- Douglas, B. C., C. C. Goad, and F. F. Morrison, "Determination of the Geopotential from Satellite-to-Satellite Tracking Data," Journal of Geophysical Research, vol. 85, 1980, pp. 5471-5480.
- Douglas, B. C., C. C. Goad, and F. F. Morrison, "Determination at the Geopotential from Satellite-to-Satellite Tracking Data," Tech. Memo. NOS NGS 24, Nat. Oceanic and Atmos. Admin., Washington, D.C. 1980.
- Ebert, W. L., "Euler Parameters, I," APL/JHU Memo SLA-75-79, December 11, 1979.
- Fischell, R. E. and V. L. Pisacane, "A Drag Free Lo-lo Satellite System for Improved Gravity Field Measurements," in Applications of Geodesy to Geodynamics, Department of Geodetic Science Report, no. 280, Ohio State University, Columbus, Ohio, 1978, pp. 213-219.
- Fredo, R. M. and M. H. Kaplan, "Procedure for Obtaining Aerodynamic Properties of Spacecraft," J. Spacecraft, 18, 1981, pp. 367-373.
- Frey, H., "MAGSAT Scalar Anomaly Distribution: The Global Perspective," Geophysical Research Letters, 9, 1982, pp. 277-280.
- Gaposchkin, E. M., "Memorandum to GRAVSAT Data Analysis Group," January 27, 1981.
- Hajela, D. P., "Improved Procedures for the Recovery of 5° Mean Gravity Anomalies from ATS-6/GEO-3 Satellite-to-Satellite Range-Rate Observations," Dept. of Geodetic Science Report No. 276, Ohio State University, Columbus, Ohio, 1978.
- Heyler, G. A., "GRM Simulation and Analysis Aerodynamics Modeling," Johns Hopkins University/Applied Physics Laboratory Report SDO 7317, June 1984.
- Hunt, J. W., "Geopotential Research Mission Spacecraft Simulation and Analysis: Guidance and Control System Simulation," Johns Hopkins University/Applied Physics Laboratory Report SDO-7397, September 1984.

3
Jacchia, L. G., "Thermospheric Temperature, Density, and Composition: New Models," Smithsonian Astrophysical Observatory Special Report 375, March 15, 1977.

Jekeli, C. and R. H. Rapp, "Accuracy of the Determination of Mean Anomalies and Mean Geoid Undulations from a Satellite Gravity Field Mapping Mission," Report 307, Dept. Geod. Sci. Surv., Ohio State University, Columbus, Ohio, 1980.

Junkins, J. L. and S. Rajaram, "Estimation of the Proof Mass Trajectory and Sensor Parameters for the Geodetic Research Mission," Sigma Scientific Consultants, Inc., Report 8403-1, April 30, 1984.

Kaula, W. M., "Inference of Variations in the Gravity Field from Satellite-to-Satellite Range Rate," Journal of Geophysical Research, vol. 88, October 10, 1983, pp. 8345-8349.

Kaula, W. M., "The Next Development in Satellite Determination of the Earth's Gravity Field," Proceedings of the USA-Hungarian 1981 Workshop on Dynamics, Eotvos University, Budapest, 1982, pp. 127-134.

Keating, T. and D. Smith, "Coupled Orbiting Inertial Reference Systems and Geopotential Research Mission (GRM) Geodesy," AIAA Guidance and Control Conference, Seattle, Washington, p. 264, August 20-22, 1984.

Keating, T., "Geopotential Research Mission (GRM)," AAS/AIAA Astrodynamics Specialist Conference, AAS Paper no. 83-347, Lake Placid, N.Y., August 22-25, 1983.

Keating, T., "Geopotential Research Mission (GRM)," The Journal of the Astronautical Sciences, vol. 32, no. 2, April-June 1984, pp. 145-158.

King, P. B., The Evolution of North America, Princeton University Press, Princeton, N.J., 1977, p. 197.

Knechtel, E. D. and W. C. Pitts, "Normal and Tangential Momentum Accommodation for Earth Satellite Conditions," Astronautica Acta, 18, 1973, pp. 171-184.

Krynski, J., "A Global Determination of the Earth's Gravity Field by Using Satellite-to-Satellite Tracking," Bollettino di Geodesia e Scienze Affini, no. 3, 1981a.

- Krynski, J., "A Solution for Determination of the Gravity Field from Satellite-to-Satellite Tracking Data," Proceedings of the 4th International Symposium "Geodesy and Physics of the Earth," Karl-Marx-Shadt, 1980.
- Krynski, J., "Possibilities of Low-Low Satellite Tracking for Local Geoid Improvement," Report of the Geodetic Institute of the Technical University at Graz no. 317, Graz, 1978.
- Lambeck, K., "Lateral Density Anomalies in the Upper Mantle," Journal of Geophysical Research, 81, 1976, pp. 6333-6340.
- Lancaster, E. R., R. H. Estes, and R. C. Chin, "GRAVSAT Error Analysis Results for One Degree Gravity Resolution," GSFC X-932-80-2, January 1980.
- Langel, R. A., "MAGSAT Scientific Investigations," Johns Hopkins APL Technical Digest 1, 1980, pp. 214-227.
- Langel, R. A., "The Magnetic Earth as Seen from MAGSAT, Initial Results," Geophysical Research Letters, vol. 9, no. 4, 1982, pp. 239-242.
- Langel, R. A., R. H. Estes, L. B. Fabino, and E. R. Lancaster, "Initial Geomagnetic Field Model from MAGSAT Vector Data, Geophysical Research Letters, 7, 1980, pp. 793-796.
- Langel, R. A., G. Ousley, J. Berbert, J. Murphy, and M. Settle, "The MAGSAT Mission," Geophysical Research Letters, vol. 9, no. 4, 1982, pp. 243-245.
- Leger, Lubert J., "Oxygen Atom Reaction with Shuttle Materials at Orbital Altitudes," NASA TM-58246, May 1982.
- Lerch, F. J., "Status of the Geopotential," Review of Geophysics and Space Physics, vol. 21, no. 3, April 1983, pp. 560-564.
- Lerch, F. J., S. M. Klosko, R. E. Laubscher, and C. A. Wagner, "Gravity Model Improvement Using GEOS-3 (GEM-9 and 10)," Journal of Geophysical Research, vol. 84, no. B8, July 30, 1979, pp. 38973916.
- Lerch, F. J., J. G. Marsh, S. M. Klosko, and R. G. Williamson, Journal of Geophysical Research, vol. 87, no. C5, 1982, pp. 3281-3296.

- Lerch, F. J., B. H. Putney, C. A. Wagner, and S. M. Klosko, "Goddard Earth Models for Oceanographic Applications (GEM 10B and 10C)," Mar. Geod., 5, 1981, pp. 145-187.
- Lozier, D. W. and J. M. Smith, "Algorithm 567 Extended-range Arithmetic and Normalized Legendre Polynomials," ACM Trans. on Math. Soft., vol. 7, no. 1, 1981, pp. 141-146.
- MacArthur, J. L. and A. S. Posner, "Satellite-to-Satellite Range-Rate Measurements," IEEE Transactions on Geoscience and Remote Sensing, vol. GE-23, no. 4, July 1985, pp. 517-523.
- Marsh, B. D. and J. G. Marsh, "On Global Gravity Anomalies and Two Scale Mantle Convection," Journal of Geophysical Research, 81, 1981, pp. 5267-5280.
- Mayhew, M. A., "Application of Satellite Magnetic Anomaly Data to Curie Isotherm Mapping," Journal of Geophysical Research, 87, 1982, pp. 4846-4854.
- Mayhew, M. A. and S. C. Galliher, "An Equivalent Layer Magnetization Model for the United States Derived from MAGSAT Data," Geophysical Research Letters, 9, 1982, pp. 311-313.
- Mayhew, M. A., H. H. Thomas, and P. J. Wasilewski, "Satellite and Surface Geophysical Expression of Anomalous Crustal Structure in Kentucky and Tennessee," Earth Planet. Science Letters, 58, 1982, pp. 395-405.
- Moe, M. M. and L. C. Tsang, "Drag Coefficients for Cones and Cylinders According to Schamberg's Model," AIAA Journal, 11, 1973, pp. 396-399.
- O'Keefe, J. A., A. Eckels, and R. K. Squires, "The Gravitational Field of the Earth," Astron. J., 64, 1959, pp. 245-253.
- Peddie, N. W., "International Geomagnetic Reference Field 1980: A Report by IAGA Division I, Working Group I," J. Geomag. Geoelectr., 33, 1981, pp. 607-611.
- Pisacane, V. L., et al., "Description of the Dedicated Gravitational Satellite Mission (GRAVSAT)," IEEE Transactions on Geoscience and Remote Sensing, vol. GE-20, no. 3, July 1982.

- Pisacane, V. L. and S. M. Yionoulis, "Recovery of Gravity Variations from Satellite-to-Satellite Tracking," Report SDO-5583, Johns Hopkins University/Applied Physics Laboratory, April 1980.
- Posner, A. S., "Geopotential Research Mission Spacecraft Simulation and Analysis: Satellite-to-Satellite Tracking Data Analysis," Johns Hopkins University/Applied Physics Laboratory Report 52-R-020, April 1984.
- Rapp, R. H., D. P. Hajela, "Accuracy Estimates of 1 x 1 Mean Anomaly Determinations from a High-Low SST Mission," Department of Geodetic Science, Report No. 295, Ohio State University, Columbus, Ohio, 1979.
- Rapp, R. H., "Comparison of Surface and Satellite Gravity Data," Applications of Geodesy to Geodynamics, Department of Geodetic Science Report No. 280, 1978, Ohio State University, Columbus, Ohio, pp. 267-272.
- Ray, J. C., "Survey of DISCOS Technology," EOS Trans. AGU, 64, 1983, p. 207.
- Regan, R. D. and B. D. Marsh, "The Bangui Magnetic Anomaly: Its Geological Origin," Journal of Geophysical Research, 87, 1982, pp. 1107-1120.
- Reinhardt, V., "A Simplification of the Least Squares Determination of the Gravity Field from Low-Low Satellite Tracking Data Utilizing an Operator Representation of the Range Observable," Bendix Corp., Columbia, Md. preprint, February 1984.
- Ricardi, L. J. and M. L. Burrows, "A Recurrence Technique for Expanding a Function in Spherical Harmonics," IEEE, Trans. on Comp., June 1972, pp. 583-585.
- Robertson, A., "Comparison of Flight-measured Drag Characteristics with Preflight Predictions," Internal Report 71-5131.1-34, July 1971, The Aerospace Corporation, El Segundo, California.
- Rummel, R., "Determination of Short-Wavelength Components of the Gravity Field from Satellite-to-Satellite Tracking or Satellite Gradiometry--An Attempt to an Identification of Problem Areas," Manuscripta Geodetica, 4, 1979, pp. 107-148.

- Rummel, R., "Error Analysis of Low-Low Satellite-to-Satellite Tracking; an Error Analysis," Department of Geodetic Science Report No. 306, Ohio State University, Columbus, Ohio, 1980.
- Rummel, R., C. H. Reigber, and K. H. Ilk, "The Use of Satellite-to-Satellite Tracking for Gravity Parameter Recovery," Proceedings of European Workshop on Space Techniques, Schloss Elmau, West Germany, 1978.
- Schaaf, S. A. and P. L. Chamber, Flow of Barefield Gases, Princeton University Press, 1958.
- Schnetzler, C. C. and R. D. Allenby, "Estimation of Lower Crust Magnetization from Satellite Derived Anomaly Field," Tectonophysics, 93, 1983.
- Schnetzler, C. C., P. T. Taylor, R. A. Langel, "Mapping Magnetized Geologic Structures from Space: The Effect of Orbital and Body Parameters," NASA TM-86134, August 1984.
- Schnetzler, C. C., P. T. Taylor, R. A. Langel, W. J. Hinze, and J. D. Phillips, "Verification of MAGSAT Anomaly Data: A Comparison Between the Recent U.S. Composite Magnetic Anomaly Map and Satellite Results," Journal of Geophysical Research, 90, 1985, pp. 2543-2548.
- Seidl, M. and E. Steinheil, "Measurement of Momentum Accommodation Coefficients on Surfaces," Characterized by Auger Spectroscopy, SIMS and LEEDS, in Rarefied Gas Dynamics, Proceedings of 9th International Symposium 1974, vol. II, pp. E.9-1 to E.9-12, ed. M. Becker and M. Fiebig, DFVLR-Press, Porz-Wahn, Germany, 1974.
- Sjoberg, Lars, "Least Squares Combination of Satellite and Terrestrial Data in Physical Geodesy," Annals. Geophysics, t. vol. 37, fasc. no. 1, 1981, pp. 25-30.
- Smith, J. M., F. W. J. Olver, and D. W. Lozier, "Extended Range Arithmetic and Normalized Legendre Polynomials," ACM Trans. on Math. Soft., vol. 7, no. 1, 1981, pp. 93-105.
- Sonnabend, D., "Study of a New Drag-Free Air Density Instrument Requiring No Propellant," Stanford University Report to NASA-Langley (Aeronomy Section), April 1976.

- Spencer, N. W., H. B. Niemann, and G. R. Carignan, "The Neutral Atmosphere Temperature Instrument," Radio Science, 8, 1973, p. 284.
- Stanley, H. R., "The GEOS-3 Project," Journal of Geophysical Research, vol. 84, no. B8, 1979, pp. 3779-3783.
- Taylor, P. T., T. Keating, W. D. Kahn, R. A. Langel, D. E. Smith, and C. C. Schnetzler, "GRM: Observing the Terrestrial Gravity and Magnetic Fields in the 1990's," EOS, vol. 64, no. 43, October 25, 1983, pp. 609-611.
- Taylor, P. T., T. Keating, D. E. Smith, R. A. Langel, C. C. Schnetzler, and W. D. Kahn, "The Geopotential Research Mission: Mapping The Near Earth Gravity and Magnetic Fields," International Symposium on Remote Sensing of Environment, Second Thematic Conference, Remote Sensing for Exploration Geology, Fort Worth, Texas, December 6-10, 1982.
- Thomas, L. B., "Accommodation of Molecules on Controlled Surfaces," Rarefied Gas Dynamics, vol. 74, part I, pp. 83-108, AIAA, New York, 1980.
- Tsien, H. S., "Superaerodynamics, Mechanics of Rarefied Gases," Journal of Aeronautical Science, 13, 1946, pp. 653-664.
- Vonbun, F. O., "Probing the Earth's Gravity Field by Means of Satellite-to-Satellite Tracking," Phil. Trans. Roy. Soc. London, Ser., 284, pp. 475-483, 1977c.
- Vonbun, F. O., W. D. Kahn, W. T. Wells, and T. D. Conrad, "Determination of 5' x 5' Gravity Anomalies Using Satellite-to-Satellite Tracking Between ATS-6 and Apollo," Geophys.-F.R. Astr. Soc., 61, 1980, pp. 645-658, published by Blackwell Scientific Publications, Oxford, London, Edinburgh, Boston, and Melbourne.
- Vonbun, F. O., W. D. Kahn, W. T. Wells, and T. D. Conrad, "Gravity Anomalies Determined from Tracking the Apollo-Soyaz," NASA TM-78031, Goddard Space Flight Center, 1977a.
- Walter, L. S., "Geodynamics," NASA Conference Publication No. 2325.
- Watts, A. B., "Present Status of Marine Geodesy," Applications of Geodesy to Geodynamics, Department of Geodetic Science Report No. 280, Ohio State University, Columbus, 1978, pp. 251-256.

- Wolff, M. and K. Fertig, "Earth Gravitational Potential Measurement Using a Satellite Pair," Trans. Amer. Geophysical Union, vol. 50, no. 4, April 1969, p. 127.
- Vansouni, P. A., and D. B. DeBra, "Nonlinear Identification in the DISCOS Position Sensor," Journal of Spacecraft and Rockets, vol. 2, no. 1, January 1976, p. 26.
- Zietz, I., et al., "Composite Magnetic Anomaly Map of the United States," Map GP-954A, two sheets, 1982, U.S. Geol. Surv., Reston, Virginia.
- Barnes Engineering Company, "Technical Description of the Model 13-401 Earth Sensor," BEC P.-1677, September 1972.
- "Geopotential Research Mission," NASA/Goddard Space Flight Center Publication, January 1985.
- Goddard Space Flight Center, "Specifications for NASA Standard Inertial Reference Unit," Specification No. GSFC-S-712-10, May 1976.
- "GRM Spacecraft Simulation and Analysis: DISCOS Calibration," Johns Hopkins University/ Applied Physics Laboratory Report SDO-7325, June 1984.
- IEEE Transactions on Geoscience and Remote Sensing, vol. GE-23, no. 4, July 1985.
- Journal of Geophysical Research, "Solid Earth and Planets," vol. 90, no. B3, February 28, 1985. Published by American Geophysical Union.
- National Oceanic and Atmospheric Administration, U.S. Standard Atmosphere, 1976, U.S. Government Printing Office, 1976.
- "Oceanography from Space: A Research Strategy for the Decade 1985-1995," Joint Oceanographic Institutions Incorporated, July 1984.
- Proceedings of Science Conference, "Geopotential Research Mission," University of Maryland, October 29-31, 1984. NASA Conference Publication 2390.
- Reviews of Geophysics and Space Physics, "Papers from U.S. National Report to IUGG," vol. 21, no. 3, April 1983. Published by American Geophysical Union.

Seventh Annual Conference on the NASA Geodynamics Program, May 1984.

Sperry Flight Systems, "NASA Standard Reaction Wheel," undated.

U.S. Geological Survey, "Magnetic Tape of Gravity Values for the U.S.," PB-82-253378,
Nat. Tech. Inform. Serv., Springfield, Virginia 1982.